Flow structure and coherence in the wake of a lifting wing with multiscale sinusoidal cut-in trailing edge serrations

Simon L. Prigent

Department of Aeronautics
Imperial College London
London SW7 2AZ
United Kingdom

This thesis is submitted for the degree of Doctor of Philosophy in fluid mechanics

June 2017

I hereby declare that this thesis, and the research to which it refers, are entirely my own work and have not been submitted for any other award. Where other sources of information have been used they have been acknowledged and fully referenced.

The copyright of this thesis rests with the author and is made available under a Creative Commons Attribution Non-Commercial No Derivatives licence. Researchers are free to copy, distribute or transmit the thesis on the condition that they attribute it, that they do not use it for commercial purposes and that they do not alter, transform or build upon it. For any reuse or redistribution, researchers must make clear to others the licence terms of this work.

Simon Lucien Prigent
London,
June 2017

Acknowledgements

I would like to start by thanking my supervisors, Paul Bruce and Oliver Buxton, for giving me the opportunity to work on this research project and be part of such a multicultural and international group of Ph.D. students. I was lucky enough to go abroad on many occasions to present my work at various international conferences and take part in workshops and have them spending many hours to improve the quality of manuscripts before sending them to various journals or editorial committees. They have scientifically challenged me over the course of this thesis to show me the way towards conducting independent research.

A peculiar aspect of Academia is to find yourself talking about many a topic with renown researchers and professors (e.g. that have invented the technics you base your work on) and Ph.D. students alike around a coffee or a drink after a day of conference in a nice and sunny city. The current thesis has undoubtedly gained from these discussions and I am grateful to those I have shared this time with. Those who have been there for coffee breaks at the arguably less exotic place that SCR is are not to be forgotten. An estimated $530\,\mathrm{g}$ of pure caffeine has served to the fulfillment of this Ph.D. and coffee is naturally better when shared. Cheers to the repeated breaks, some thrilling (!) time, and the refreshing conversations!

The whole team at Oldenburg has been very welcoming and helpful, and the experiments we conducted would not have been achieved without their committed support. I would like to thank in particular Michael and Aga for organising barbecues upon my arrival to make sure I would quickly meet everyone, and ensured I had everything I could need both in the lab and to settle in the city. It was a good surprise to see him up bright and early on a Sunday morning to wish good luck to the few of us doing the local half marathon. The weekly group breakfasts were also a good way to spend time with all the team and exchange on a range of topic from the replacement of an NI board to results from the last games, not forgetting the local delicacies that are arguably suited for a 9am snack. All the Ph.D. students, technicians and post-docs in the group have helped me at some point during my stay, be it to install the heavy/bulky set-ups or to brief me on the use of the active grid and the lab facilities in general: it was great to be part of the team and being able to discuss the methods and results with them.

This scientific venture would not have been possible without the support of the European Commission, that funded the project under a Marie Skłodowska-Curie action (MULTISOLVE project, No. 317269).

I am grateful for the friends I have met at ICCCAC, and later on at TVH, without whom the training sessions would not have been anywhere near as enjoyable as they have been, and who kept me motivated during the months off when injuries would strike and shared the joy alongside part of the somewhat $11,000$ km run during the course of this PhD. Along with them, I have come to learn a few life lessons, and I hope that those who either taught me or experienced it with me, will recognise themselves. *Honister Honey* can be a good name for a bike. A beer and tapas are worth the trip to the Canaries, so long as they come after roughly 10 h of racing on a wonderful volcanic island. Cakes and pastries are perfect post-run nutrition on Sunday mornings. When your bike decides that "hit the road" needs to be taken more literally on the way to Brighton, it can be painful. "A little bike ride because it's sunny" does not refer to a little bike ride, prepare for at least five or six hours. One should not forget his running shoes and realise it fifteen minutes before the start of a race. Doing a marathon in the mountains with a brand new pair of shoes can lead to big blood blisters. Welsh weather has the ability to go through snow, hail, rain and stormy winds within one hour, then repeat its cycle. Marsh can be fun to run through, until one of your leg gets thigh-deep into it. The inclining treadmills at Ethos can prove useful in the endeavor of compensating for the pancake-flatness of this part of the country. They also provide a free acclimatisation to the southernmost race locations. When in doubt, do a few more miles.

My friends outside of Imperial, be it in London or in other countries, have helped reminding me about the "real world" outside of academia during those three and a half years. If only for that, or the weekends, holidays and all that I will not write here, I owe them a lot and they deserve my gratitude.

Finally, I would like to say a big thank you to all my family. They have all been there to help and support me at some point during the many years I have spent at university. I owe a lot to my parents, who have always been encouraging me to pursue my ideas, and wanted me to study and do what I enjoyed. They, and my brother, have been by my side during the good and the bad moments that life brings along. This is, naturally, without forgetting my aunts, uncles, grand-parents, cousins and in-law! They were also along the journey during the stress of exams, the joy of holidays, the different steps in life, and the small things that make you what you are. Life goes on, and as some who were so present in my childhood will not be with us when turning this important page, I keep in mind what they brought me and the joy of having a newcomer in the family. It is easier to aim high when you stand on solid grounds. They are these grounds and I would not be who I am today without them.

Abstract

This thesis presents an experimental investigation into the wake of a lifting wing with multiscale cut-in trailing edge serrations. More specifically, it looks into how the wake is affected by the serration patterns, both in terms of mean properties and dynamic and spectral information. The flow is investigated by means of particle image velocimetry and hot-wire anemometry to combine the dynamic and spatial strengths of the two experimental techniques. The response of a wing fitted with such serrations and subjected to unsteady inflows is studied by means of lift measurement and hot-wire anemometry in the wake.

Cut-in trailing edges are found to generate a strong secondary flow from below the peaks towards the troughs. Such a flow pattern increases the velocity deficit behind the peaks while re-energising the wake behind the troughs, giving rise to span-wise inhomogeneity of the velocity deficit and wake width which persists far downstream.

The introduction of cut-in serrations exhibits bluntness that in turn generates vortex shedding that locks into a bent cell structure. The use of multiscale patterns weakens the cell structures which translates into a reduction of vortex shedding intensity as well as a reduction of span-wise correlation at both vortex shedding and low frequencies. The use of an alternative sharp approach offers a compromise that gives less coherence reduction on the edges of the wake but avoids the introduction of a clear vortex shedding signal.

Under unsteady inflow conditions, the 2-iteration multiscale pattern provide the strongest overall reduction of coherence. Statistical analysis of lift fluctuations under unsteady and intermittent inflow conditions reveals that the single tone sinusoidal pattern has the strongest reduction of the distribution's tails. Finally, the multiscale patterns are found to smooth the time-evolution of the lift fluctuations when the wing is submitted to a sinusoidal variation of the flow incidence.

Contents

1 Introduction **13**

1.1 Motivation and thesis outline 13

1.2 literature review 15

1.2.1 Blunt and wavy trailing edges 16

1.2.2 Flat plates 17

1.2.3 Extension plates on airfoils 20

1.2.4 Cut-in approach 23

1.2.5 Multiscale geometries and vortex shedding 23

1.2.6 Unsteady inflows 24

1.3 Aims and thesis outline 25

2 Experimental methodology **26**

2.1 Trailing edge geometries 27

2.1.1 Blunt trailing edges: sinusoidal and multiscale 27

2.1.2 Sharp trailing edges 28

2.2 Apparatus at Imperial College London 29

2.2.1 Hot-wire measurements 30

2.2.2 Boundary layer measurements using hot-wires 31

2.2.3 PIV: cross-stream 2D-3C 32

2.2.4 PIV: span-stream 2D-2C 33

2.3 Apparatus at ForWind - University of Oldenburg 34

2.3.1 Active grid and wing 34

2.3.2 Hot-wire measurements . . . 36
2.3.3 Force measurements . . . 37
2.3.4 Protocols . . . 37
Sinusoidal protocol . . . 37
“45 degree” protocol . . . 38
Gaussian protocol . . . 38
Intermittent protocol . . . 39

3 Sinusoidal serrations **40**
3.1 Mean properties . . . 40
3.2 Spectral analysis . . . 43
3.3 Coherence . . . 49
3.4 Discussion on shedding energy span-wise oscillations . . . 53
3.5 Cell structures in the wake . . . 54
3.5.1 Dephasing . . . 56
3.5.2 Modal decomposition . . . 58
POD modes . . . 59
OMD modes . . . 63
3.5.3 Independence of the cells . . . 67
3.6 Discussion and concluding remarks . . . 69

4 Effecting the coherence **70**
4.1 Multiscale TE . . . 70
4.1.1 PSD . . . 71
4.1.2 Coherence . . . 72
4.1.3 De-phasing . . . 75
4.1.4 OMD modes . . . 77
4.1.5 Reynolds stress . . . 80
4.2 Sharp trailing edge geometry approach . . . 83
4.2.1 Boundary layer measurements . . . 83
4.2.2 Spectra and coherence . . . 85

4.2.3 OMD modes of sharp TE . . . 88
4.3 Discussion and concluding remarks . . . 91

5 Coherent incoming flow **92**
5.1 Background and approach . . . 92
5.2 Coherence . . . 93
5.2.1 Results from the sinusoidal protocol . . . 93
5.2.2 45deg protocol . . . 96
5.2.3 Gaussian protocol . . . 100
5.2.4 Intermediate conclusions . . . 104
5.3 Discussion on vertical asymmetry of the shedding mechanism . . . 105
5.4 Force measurements . . . 106
5.4.1 Gaussian inflow . . . 106
5.4.2 Intermittent inflow . . . 109
5.4.3 Sinusoidal inflow . . . 116
5.5 Discussion and concluding remarks . . . 117

6 Conclusions and future work **118**

List of Figures

1.1 Photographs of an off shore wind farm ©Vattenfall Wind Power (left) and a gliding barn owl (right). . . . 14
1.2 Castellations of a blunt trailing edge. . . . 16
1.3 Sketch of sawtooth serrations, adapted from [32]. . . . 18
1.4 Flat plate serrations 19
1.5 Triangular serrations: flow disruption and noise reduction. . . . 21

2.1 Illustration of the wing with cut-in interchangeable trailing edges. . . . 26
2.2 Illustration of multiscale patterns used for the trailing edges. A is the amplitude of the cut-in serrations. . . . 28
2.3 Side sketch of blunt (blue) and sharp (red) sinusoidal trailing edges. . . . 28
2.4 Hot wires locations for the two types of traverses, conducted at various downstream positions. 30
2.5 Sketch of the cross-stream PIV (2D-3C) apparatus. Left: 3D view, right: top view. . . . 32
2.6 Sketch of the span-stream PIV (2D-2C) apparatus 33
2.7 Active grid from Knebel [39] (a) and current set-up (b), as sketched in fig. 2.4a. . . . 34
2.8 Drawing of the manufactured wing. . . . 35
2.9 Sketch of the hot wire measurements set-up: side view of the wind tunnel (a) and position of the probes relatively to the serration patterns (b). . . . 37
2.10 Illustration and lift output of a sinusoidal protocol. . . . 38

3.1 Mean (a) and RMS (b) wake velocity profiles at $x/c = 0.04$ for three span-wise locations behind $S20W84B$. . . . 41

3.2 Downstream evolution of maximum velocity deficit (a) and semi-wake width (b) at three span-wise locations for $S20W84B$. 42
3.3 PIV maps of mean velocity span-wise component and mean stream-wise vorticity at $x/c = 0.4$. TE peaks (P) and troughs (T) locations indicated on the maps. 43
3.4 Vertical PSD log_{10} map at $x/c = 0.04$ behind the TEs troughs 44
3.5 E_{sh} sensitivity to ΔSt. 45
3.6 Spectra at three span-wise positions for $S20W84B$ and $S20W40B$ at $x/c = 0.04$ (a) and $x/c = 2$ (b). Inserts show a zoom around St_{sh}. Downstream evolution of spectra values at St_{sh} for $S20W84B$ (c). 47
3.7 Span-wise PSD log_{10} map at $x/c = 0.04$ behind four tested wings. 49
3.8 Downstream evolution of span-wise traverses of shedding-associated energy. N.B.: Oscillations at $x/c = 0.04$ are discussed in section 3.4. 50
3.9 γ^2 map between Trough and Mid-point, and Trough and Peak, behind $S20W84B$ at given downstream locations 52
3.10 Vertical traverses of $\gamma^2(St_{sh})$ between two span-wise locations: trough and mid-point. . . 54
3.11 Span-wise γ^2 map at $x/c = 0.04$ behind three blunt cases (a)-(c). Span-wise evolution of γ^2 averaged around its shedding value (d). The reference probe is fixed at the trough ($\tilde{z}/W = 0$) while the second probe is traversed towards the peak ($\tilde{z}/W = -0.5$). 55
3.12 Span-wise traverses of shedding-associated energy at $x/c = 0.04$ and comparison with $S20W00B$. 56
3.13 Sketch of three possible vortex shedding structures behind a serration. 57
3.14 Span-wise and downstream evolution of weighted de-phasing, Γ_{sh}, with reference point fixed at the trough ($z/W = 0$). 58
3.15 POD energy for the two blunt sinusoidal cases. 60
3.16 POD modes (i), (ii) and (iii) for $S20W84B$. 61
3.17 POD modes (i) and (i)-b for $S20W40B$. 62
3.18 POD coefficients' PSD 62
3.19 OMD spectra 64
3.20 OMD modes (i)-(iv) for $S20W84B$. 65
3.21 OMD modes (i) for $S20W40B$. 66

3.22 Comparison between de-phasing obtained by HW and OMD reconstructions with modes (i) (ii) (iii), and (i) (ii) (iii) (iv). 67
3.23 Span-wise traverses of correlation coefficient with references at four span-wise locations, performed at three downstream locations for $S20W40B$. 68

4.1 PSD maps, $x/c = 0.04$ downstream of four tested trailing edges. 71
4.2 Span-wise and downstream evolution of shedding associated energy, E_{sh}. N.B. Oscillations at $x/c = 0.04$ are discussed in section 3.4. 72
4.3 γ^2 maps, $x/c = 0.04$ downstream of four tested trailing edges. 74
4.4 γ^2_{sh}, $x/c = 0.04$ downstream of the trailing edges. 74
4.5 Span-wise and downstream evolution of shedding associated coherence, γ^2_{sh}. 75
4.6 Span-wise and downstream evolution of weighted de-phasing, Γ_{sh}, with reference point fixed at the trough ($\tilde{z}/W = 0$). 76
4.7 OMD spectra 78
4.8 OMD modes (i)-(iv) for $S20W84B$ (top two rows) and $2iS20W84B$ (bottom two rows) . 79
4.9 normalised OMD mode (i) for $S20W40B$ (left) and $2iS20W40B$ (right). Mode (i)-b is a secondary mode of the main peak. 81
4.10 Maps of partial Reynolds stress downstream of four tested trailing edges, from PIV data. . 82
4.11 cross-stream evolution of intermittency for the pressure side of $S20W84B$ at the trough. . 84
4.12 Vertical PSD log_{10} map at $x/c = 0.04$ behind the TEs troughs 86
4.13 Spectra of $S20W84B$ & $S20W84S$ (top) and $S20W40B$ & $S20W40S$ (bottom), at $x/c = 0.04$ 87
4.14 γ^2 map (Trough - Mid-point) behind $S20W84S$, $S20W84B$ and $S00W00S$ at $x/c = 0.04$ 87
4.15 OMD spectra 88
4.16 OMD modes (i)-(iv) for $S20W84S$. 89
4.17 OMD mode (i) and (iv) for $S20W40S$. 90

5.1 Sinusoidal protocol: PSD and coherence without wing. Alternated colours for ease of visualisation. 94
5.2 Sinusoidal protocol: γ^2 downstream of $S00W00S^*$, relative to the trough ($\tilde{z}/W = 0$). Alternated colours for ease of visualisation. 95

5.3 Sinusoidal protocol: γ^2 for all TEs. 97
5.4 Sinusoidal protocol: PSD for all TEs, $\tilde{z}/W = 0$ 98
5.5 45deg protocol: PSD and coherence without wing. Alternated colours for ease of visualisation. 98
5.6 45deg protocol: γ^2 downstream of $S00W00S^*$. Alternated colours for ease of visualisation. 99
5.7 45deg protocol: PSD for all TEs, $\tilde{z}/W = 0$ 100
5.8 45deg protocol: γ^2 for all TEs. 101
5.9 45deg protocol: γ^2_{25Hz} 102
5.10 Gaussian protocol: PSD and coherence without wing. Alternated colours for ease of visualisation. 102
5.11 Gaussian protocol: γ^2 downstream of $S00W00S^*$. Alternated colours for ease of visualisation. 103
5.12 Gaussian protocol: γ^2 for all TEs. 104
5.13 Gaussian protocol: PSD for all TEs, $\tilde{z}/W = 0$ 105
5.14 Sketch of the shedding mechanism at a blunt trailing edge. 106
5.15 Lift curve and standard deviation, for four trailing edges, with Gaussian inflow. 107
5.16 PDF of lift fluctuations for all five wings at four pitch angles (Gaussian inflow). 108
5.17 Lift curve and standard deviation, for four trailing edges, with intermittent inflow. 109
5.18 PDF of lift fluctuations for all five wings at four pitch angles (intermittent inflow). 110
5.19 PDF, shifted for clarity, of lift fluctuations for four trailing edges at all tested pitch angles (intermittent inflow). 111
5.20 PSD of lift fluctuations for four trailing edges at three pitch angles (intermittent inflow). . . 113
5.21 Incremental PDF for four wings at two pitch angles (intermittent inflow). 115
5.22 Phase-averaged lift fluctuations under sinusoidal inflow conditions. 116

Chapter 1

Introduction

1.1 Motivation and thesis outline

The study of turbulent flows lies on a fine line, balancing complex fundamental interrogations with technological applications. Industry often looks to the scientific community to develop the underpinning knowledge of challenging flows, sometimes even opening new fields of research. This intrinsic relationship illustrates the beauty of fluid mechanics; inherently abstract, yet omnipresent in our everyday life.

The recent surge in interest in wind turbine technology came with the challenge of better understanding the noise production mechanisms involved, in addition to optimising their aerodynamic properties. In a very different application, the airframe noise of an aircraft is becoming relatively more important, given the progress made on the engines. Both cases are linked to the topic of an isolated airfoil's noise production, which has been shown to be highly dependent on the fluid mechanics involved. In other contexts, airfoils are installed in a cascade arrangement, or directly in the wake of one another, in which case not only the airfoil behaviour, but also the properties of its wake are important, along with its response to a turbulent, possibly coherent, incoming flow.

The trailing edge is a key part of an airfoil: on the one hand it is responsible for noise production due to the interaction of the turbulent boundary layers with its solid edge, and, on the other hand it impacts the development of the wake. Nature can often inspire scientific research by the sheer number of adaptations developed to tackle hunting, or survival challenges. The ability of birds of prey to fly silently is one such example, as they need to glide towards their prey without attracting attention. Barn owls, depicted in fig. 1.1,



Figure 1.1: Photographs of an off shore wind farm ©Vattenfall Wind Power (left) and a gliding barn owl (right).

are amongst the most silent of these, and on top of their extremely light weight, one can notice some peculiar characteristics of their wings. The feathers have two key properties: they offer porosity at the trailing edge, and their layout creates an irregular pattern. Both aspects have been studied to understand their links with the ability to glide silently. Research has indeed been conducted on the topic of trailing edge noise and serrations have been proposed as an effective means of mitigating its production.

Several studies have investigated the flow structures generated around such geometrical modifications, and their impact on the far field noise. Trailing edge noise is in fact produced by the scattering of pressure fluctuations at the solid edge, and by modifying either the scattering efficiency or the correlation of such fluctuations, the noise production can be affected. However, there is still extensive work to be carried out to fully understand the different mechanisms involved and how they would be affected by different geometrical patterns. Trailing edge serrations are usually placed on an extension plate, and recent studies have looked into the use of more complex serration geometries to further reduce noise production.

A novel approach has been presented recently, where serrations are cut into the wing instead of using an extension plate. In terms of acoustics properties, and although a full understanding of the flow properties was still lacking, it was found that broadband noise reduction could be achieved, at the cost of a shedding-associated tonal noise. Furthermore, previous studies have shown the important role that the flow disruption plays in the noise reduction mechanisms, which adds to the reduction of scattering efficiency due to geometrical arrangement at the edge. It is thus important to look into this novel design with a focus on the relevant flow features, to offer a better understanding on the fluid dynamics implications of such modifications. One should also keep in mind that beyond the noise produced by an isolated airfoil, flow disruption may also affect the wake development, and the way it impinges on neighbouring blades or wings,

such as in wind farms as illustrated in fig. 1.1.

Following on the investigation of the cut-in serrations, a natural second step is the introduction of geometries aimed at mitigating potential drawbacks of such serrations. Given the promising potential of multiscale geometries in terms of reducing vortex shedding; multiscale serration patterns can be one of the paths to investigate.

The present study offers a better understanding of the wake development with cut-in sinusoidal serrations. Coherence measurements show the clear impact of the serrations compared to reference wings. It is found that vortex shedding is locked into cells, spatio-temporal structures that are investigated by means of modal decomposition of time resolved data.

Two new types of geometries are introduced: multiscale patterns for the cut-in serrations, and sharp sinusoidal modulations of the trailing edge, both detailed in section 2.1. Their impact on the spectra in the wake and coherence is reported, in particular the reduction of coherence at the vortex shedding frequency is linked to their effect on the cells.

Finally, the study offers an exploratory investigation of the behaviour of wings with such serrations with unsteady incoming flows. In particular, the effect of serrations on incoming coherence and on the dynamics of lift are presented.

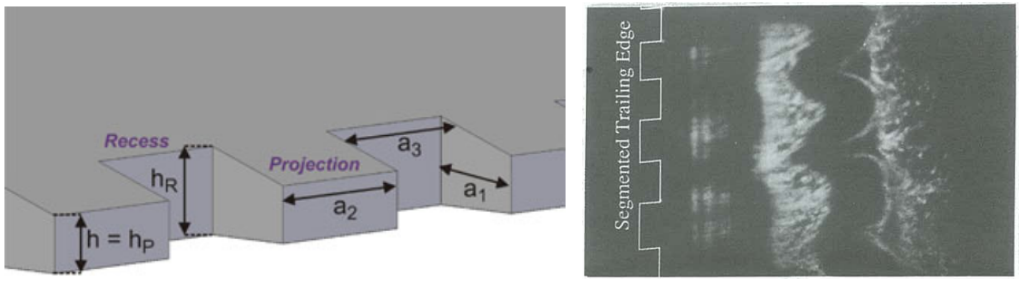
1.2 literature review

The following highlights the work previously done on the topics directly linked to cut-in trailing edge serrations. It is relevant to better understand the context in which the present work is set and to draw the main goals of this study. Technical references, e.g. relevant to some aspects of the data processing, are given within the later chapters. Since the cut-in approach exhibits bluntness at the roots, section 1.2.1 presents previous studies on geometrical span-wise modification of blunt trailing edges. Section 1.2.2 then presents trailing edges serrations in the benchmark case of flat plates. Following this, section 1.2.3 introduces similar patterns on airfoils fitted with extension plates. The recent cut-in approach is presented in section 1.2.4. Section 1.2.5 highlights some key results from studies of fractal grids or more generally fractal-forced flows, with regards to vortex shedding intensity. Finally, section 1.2.6 highlights the necessity for an investigation of the airfoil's performance under unsteady inflow conditions.

1.2.1 Blunt and wavy trailing edges

It is well known that modification of trailing edge geometry can have a significant influence on the performance of an airfoil. Previous studies [66, 29, 61, 67] have shown that truncation of the aft part of the trailing edge could produce an increase in maximum lift coefficient (C_{Lmax}). A structural benefit was also obtained, without the need to increase the maximum thickness of the airfoil, which could be particularly interesting for large wind turbines. However, the introduction of trailing edge bluntness also led to an increase of drag, tempering any aerodynamic performance gain. Such blunt wings had a constant section, and further studies introduced a span-wise geometric variation to the blunt trailing edge [68, 54, 40] in an effort to increase the base pressure and therefore reduce base drag.

It was understood that the span-wise coherent vortices shed by the blunt trailing edge were responsible for low base pressure, which resulted in a base drag increase. Tanner [68] studied different blunt span-wise patterns and found that up to a 64% reduction in base drag, compared to a straight blunt trailing edge, could be obtained. Segmented trailing edges (square-wave/castellation-like shapes) were indeed found [54] to break down the vortex street structures generated by a straight blunt trailing edge by the introduction of stream-wise vorticity at the edges of the castellations. Such patterns are depicted in fig. 1.2a from [40] and their effect on shed vortices is illustrated in fig. 1.2b with a bubble visualisation from [54]. In the latter figure, it is clear that the vortices are broken down along the span-wise extent of the square-wave patterns, which limits the base drag pressure drop mentioned earlier and explains the reduction of drag, relative to an airfoil with straight blunt trailing edge, previously observed.



(a) 3D view of trailing edge castellations. From [40]

(b) Bubble visualisation of vortices behind a castellated trailing edge. From [54]

Figure 1.2: Castellations of a blunt trailing edge.

These geometric modifications show the possible amelioration of blunt trailing edges' main drawbacks: strong vortex shedding and base drag. However, airfoil modifications should be considered in the context of key industrial challenges, such as open-rotors or wind farms, where self-noise or wake-blade interactions are particularly relevant. Vortex shedding at a straight blunt trailing edge not only impacts wing performance, but also wake properties as it generates a periodic vortex street over a large span-wise extent. It is therefore also important to understand how the shape modifications will affect the wake which may subsequently impact on a downstream blade or rotor. Tombazis & Bearman [69] studied a non-lifting plate with a sinusoidal blunt trailing edge. The flow was found to be characterised by the co-existence of modes in the shedding in the wake, which inherently alter the single tone characteristics of blunt trailing edges.

In parallel, non-blunt shape modifications inspired by nature were investigated, with the aim of improving aerodynamic performance as well as reducing noise. Waviness was primarily studied at the leading-edge, with studies inspired by humpback whales [33, 46, 23] , and showed the possibility to increase resistance to stall thanks to leading edge tubercles acting like vortex generators for the horizontal fins. It was introduced onto the trailing edge with studies such as Werle & Paterson [72] who focused on vertical undulation of the trailing edge, creating a rippled surface. The authors observed that the modified geometry introduced a span-wise component to the velocity, which seemed to re-energise the boundary layer and prevent stall. This translated into a 12% C_{Lmax} increase, with only a small corresponding increase in drag.

1.2.2 Flat plates

Widespread interest in noise reduction, and in particular trailing edge noise, has motivated the study of trailing edge serrations as a means of disrupting noise production mechanisms. Most of the airfoil self-noise mechanisms are due to the interaction of the flow disturbances with the trailing edge [12] , and therefore referred to as trailing edge noise. In fact, this interaction is mainly the scattering of surface pressure fluctuations. Such pressure fluctuations can be directly induced by the turbulent boundary layer close to the surface, or generated by the periodic vortex shedding in the case of a blunt trailing edge [30]. For a straight trailing edge, the far field noise spectrum linearly depends on the span-wise correlation length of the surface pressure [1]; which therefore also links to coherence in the velocity fluctuations based on the previous observations.

The study of trailing edge serrations - illustrated in fig. 1.3 - goes back several decades, with analytical modelling of trailing edge noise scattering by serrations on flat plates by Howe [31] [32]. The point was

made that the noise scattering at the trailing edge depends essentially on the angle between the wave-number vector of the surface pressure fluctuations and the solid edge. Under low Mach number condition, the author explains that this results in a stronger reduction of noise scattering if the serrations have an angle of no more that 45° with the free stream direction, which corresponds to narrow serrations.

More recent work has been carried out by Azarpeyvand *et al.* [6] to build models of both classic and complex serrations, and compare to experimental data. Howe's prediction is reported to poorly predict the amplitude of the noise reduction, and the authors emphasise the importance of the reduction of the correlation length of pressure fluctuations along the trailing edge as well as the role of destructive interference of the noise sources when scattering at the edge. Lyu *et al.* [42] [43] have worked on a new mathematical model to better fit with experimental or numerical data, and also reported the importance of the destructive interference of the scattering of pressure fluctuations in the vicinity of the edge, which leads to noise reduction.

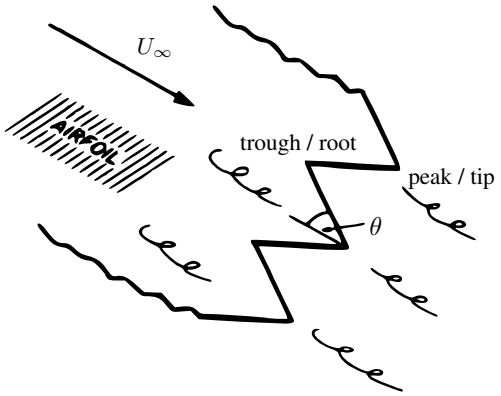
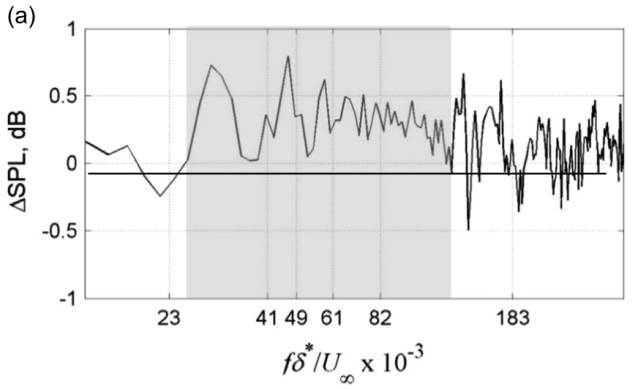
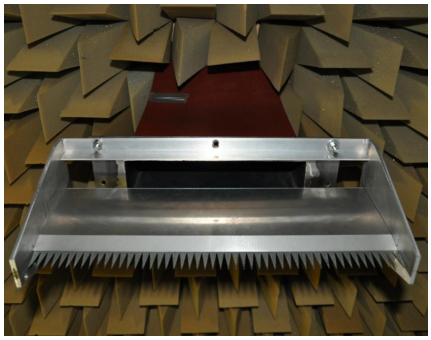


Figure 1.3: Sketch of sawtooth serrations, adapted from [32].

A study of the flow over the trailing edge serrations for flat plate at zero incidence and its aeroacoustic impact was conducted by Chong *et al.* [16]. Fig. 1.4a reports the variation of noise level between a straight reference and a narrow sawtooth serration. The authors show a reduction of noise over a large range of frequencies, depicted by the greyed area. The reduction is observed to be lower than expected since only one side of the plate was subjected to the flow, however, preliminary results suggest that the observation could be extrapolated to airfoils. A detailed investigation of the turbulent flow over and near the serrations



(a) Noise reduction (positive ΔSPL) between a straight case and sawtooth serrations (amplitude 20 mm, angle 25°). From [16]



(b) From [47]

Figure 1.4: Flat plate serrations

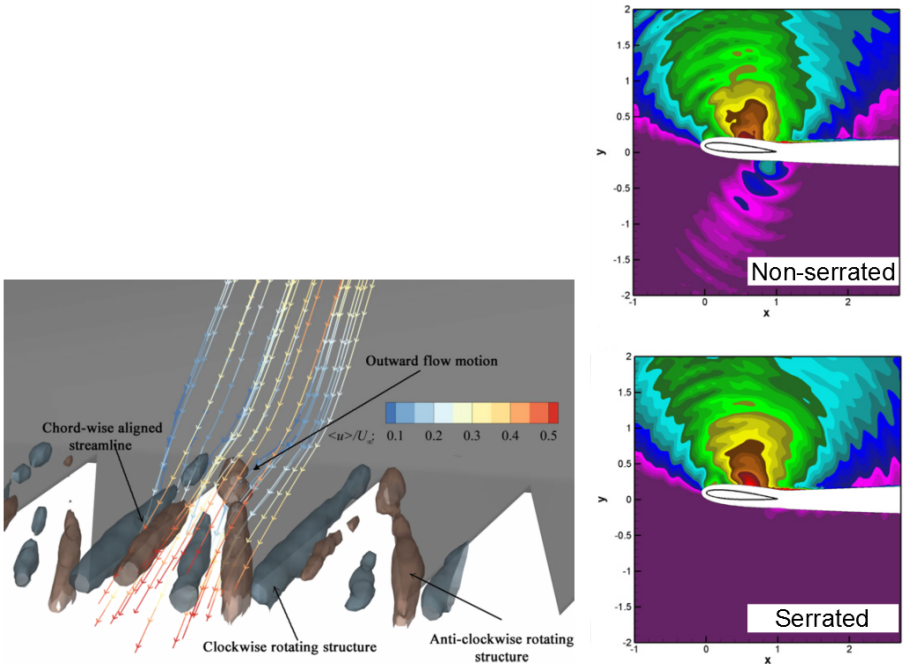
shows the existence of coherent structures, that interact with the vortices present in the turbulent boundary layer that has formed on the plate and reaches the trailing edge. The authors postulate that this mechanism reduces the efficiency of the scattering of incoming pressure waves, and, therefore, reduces the emission of noise. Moreau *et al.* [47] and Moreau and Doolan [48] also studied the trailing edge noise generated by flat plates with narrow triangular serrations, with an amplitude to wavelength ratio of 0.2 and 0.6. They found a broadband reduction of the order of 3 dB, which is higher than that measured by Chong *et al.* [16], however both sides of the plate were subjected to the flow. The plate had a finite bluntness and the associated shedding noise was greatly reduced, by up to 13 dB. The authors show that contrary to the prediction from theory, the larger wavelength (with constant amplitude) gave better sound reduction. They also found that the hydrodynamics of the turbulent near wake were also affected, suggesting that the effect of the serrations was not only on scattering efficiency, but also on the flow properties, explaining some discrepancy with the models. Indeed, the same authors [49] later focused on the mechanism of tonal noise reduction, and found that narrow wavelength serrations permitted the creation of intense coherent vortex structures, that were not observed for larger wavelengths.

1.2.3 Extension plates on airfoils

The flow around a lifting surface will inherently be different from the flat plate case, and it is thus necessary to study the serrations' impact on the former. The first approach taken was to fit extension plates at the aft of airfoils, with serrations cut out of them.

Jones and Sandberg [34, 35] conducted a Direct Numerical Simulation of a NACA0012 fitted with both serrated and classic extension plates, at moderate incidence. Two serrations are tested, with amplitude (tip to root) to wavelength ratios of $6/5$ and $12/5$. For the serrations with the higher amplitude, a significant noise reduction was seen for all frequencies above a specific threshold. The flow appeared unchanged upstream of the serrations, in terms of turbulence intensity, span-wise correlation etc. which led the authors to the conclusion that the noise reduction was due to either or both of the reduced scattering efficiency and the alteration of the flow around the serrations themselves. Furthermore, the serrated trailing edge was observed to generate stronger turbulent mixing in the near wake. The same authors later focused on the effect of the serrations on tonal noise due to the loop amplification of noise with the suction side separation bubble [59]. Fig. 1.5b, from [59], shows the contours of modulus of pressure at a given frequency, to visualise radiated noise for serrated and non-serrated extension plates. The noise radiated above the airfoil is dominated by the suction side, with no significant differences evident; however the trailing edge noise radiation is clearly visible under the airfoil, where the serrations cancel this contribution. The authors report a threshold of efficiency in frequency, under which the serrations have no acoustic effect. The frequency chosen for this figure is above the threshold of efficiency for the serrations which is why the radiation is affected. However, the acoustic feedback to the transition bubble occurs at a frequency too low to be affected, which is why the hydrodynamic part is not disrupted by the serration.

Experimental investigations of airfoils with serrated extension plates by Arce Léon *et al.* [2] [3] also reported trailing edge noise reduction. The authors observed a strong span-wise inhomogeneity in the wake behind the serrations, with, in particular, pairs of contra-rotating stream-wise vortices downstream of the roots, similar to those observed in the previously discussed studies. These vortices are attributed to the pressure difference between the two sides and create an up-wash behind the roots and a down-wash behind the tips. Fig. 1.5a, from tomographic PIV by Avallone *et al.* [5], depicts these vortices. As a result, the streamlines are distorted and no longer aligned in the stream-wise direction, a fact which may account for the disparities between the measured noise reduction and the analytical models which assume straight streamlines and only consider noise scattering. Avallone *et al.* [4] [5], studied a similar configuration using



(a) Iso-surface of streamwise vorticity and streamlines along the serration surface. From [5]

(b) Logarithmically spaced contours of one-third octave averaged modulus of pressure at target frequency. Adapted from [59]

Figure 1.5: Triangular serrations: flow disruption and noise reduction.

tomographic particle image velocimetry. The authors comfirm the findings of the previous studies regarding the strong span-wise inhomogeneity and the creation of stream-wise vortices distorting the flow. The higher turbulence intensity at the root - attributed to a stronger interaction of the pressure and suction side flows - is another disruption of the flow which the authors argue adds to the limitations of analytical models which assume unaffected flow for the prediction of the far field noise. Gruber *et al.* [26] [25] also studied an airfoil fitted with serrated extension plates. On top of the previously discussed disparities with Howe's prediction, the authors reported a thicker than normal boundary layer at the tip and a thinner than expected at the roots. No effect was observed upstream of the serrations, adding weight to the belief that most of the noise reduction is due to the 3D modifications induced in the flow around the serrations, associated with the

reduced scattering efficiency.

Chong *et al.* [15] observed the strong reduction of tonal noise by the serrations. In that case, the effect is reported to be a combination of two aspects; first, the serrations break down the two dimensionality of the Tollmien-Schlichting waves by introducing a span-wise evolution of the trailing edge pattern. Secondly, if boundary layer separation occurs close enough to the trailing edge, serrations will reduce or cancel it, and since it acts as an amplifier, such reduction will dampen the tonal noise emission. Liu *et al.* [41] gave a first insight into the aerodynamic properties of such serrations, and showed that for both symmetric and non-symmetric airfoils, the serrations had the same effects: reducing the lift coefficient pre-stall and maintaining slightly higher values post-stall, compared to non-serrated extensions.

Trailing edge serrations on extension plates have thus shown benefits in terms of noise reduction and are in fact now used in industrial applications. On-shore wind turbines now integrate such serrations in their design - cf Mathew *et al.* [44] - for which noise reduction has been reported by Oerlemans *et al.* [53] [52] and Buck *et al.* [13]. However, Vathylakis *et al.* [70] focused on the effect of the serrations' penetration angle into the flow and reported a strong dependence of the noise reduction on this parameter. In the case of wind turbines, serrations are invariably added after the blade has been manufactured and their angle to the blade's chord is not precisely determined, which shows a possible limitation of the use of serrations in such applications where their position is not well controlled.

Other applications involving arrays of blades could also be feasible. In fact, the noise reduction due to serrations was investigated in blade cascades by Finez *et al.* [21] who found similar broadband noise reduction to that reported in previous studies on isolated blades. In addition, Sanjosé *et al.* [60] simulated the flow and acoustics around a controlled diffusion airfoil with serrations and reported a broadband noise reduction.

The vast majority of studies have focused on simple patterns of serrations, and very few have considered more complex geometries. One such study was that of slitted sawtooth, investigated by Gruber *et al.*[27] and Arce Léon *et al.* [2] with the aim of combining a flow permeability at the trailing edge with a geometry that could better tackle high frequency noise. The noise reduction variation between a solid sawtooth and a slitted sawtooth vary within the two studies, which suggest that the amplitude to wavelength ratio is an important parameter for the efficiency of those compound geometries.

1.2.4 Cut-in approach

A recent approach has been to directly cut serrations into a wing [17, 14, 50, 55] instead of using an extension plate, with the potential aim of improving structural robustness. Indeed, whilst being structurally strong in comparison to a serrated extension plate, cut-in serrated trailing edges are observed to lead to broadband noise reduction as presented by Chong *et al.* [14]. However, the exhibited bluntness induces vortex shedding and an associated tonal noise, which is a clear limitation to the approach [14]. Additionaly, wings with blunt trailing edges are known to produce a higher lift coefficient, and Nedić *et al.* [50] indeed observed a slight increase in lift to drag ratio compared to an unmodified wing when using fractal cut-in serrations. One objective of the current research is thus to better understand the impact this shedding has on an airfoil's wake and to devise ways to mitigate this effect. Studies with extension plates have shown that noise reduction is achieved not only due to scattering, but to a large extent due to the modification of the flow around the serrations. Having a clear picture of the flow for simple cut-in serrations, and their near wake development, is therefore a key complement to the existing studies.

1.2.5 Multiscale geometries and vortex shedding

Chong *et al.* [14] have reported that a limitation to the cut-in approach is the introduction of vortex shedding that creates noise at a particular frequency. Recent studies by Nedić and Vassilicos [51], and Nedić *et al.* [50], have shown the possible use of multiscale/fractal geometries to reduce vortex shedding, in the context of cross-stream plates and trailing edge serrations, respectively. Melina *et al.* [45] have studied the flow behind a fractal grid for an investigation of heat-transfer, and found as a side effect that grid vortex shedding was reduced for the fractal cases. In the context of pre-mixed flames, Goh *et al.* [24] reported that fractal grids reduced the sensitivity to upstream condition, which raises the question as to whether this could be transferred to the context of airfoils trailing edges. This multiscale approach could thus prove useful as a means to reduce vortex shedding intensity, and shall be explored in a second step.

To avoid the introduction of sharp angles that could hinder the reduction of vortex shedding intensity, for instance by the generation of stream-wise vorticity, smooth patterns are chosen. Furthermore, span-wise coherence close to the trailing edge can be an indication of acoustic noise sources - or base drag in the case of vortex shedding by blunt wings, its reduction has potential benefits for industrial applications. Since not much is known about the effect of the serrations on span-wise coherence in the wake, this shall be one of the focuses of this study.

1.2.6 Unsteady inflows

As previously presented, the main application for trailing edge serrations so far is the wind turbine industry. By its nature, it raises a number a questions that need to be addressed. The noise generation is important for inland installations, and has been studied as already discussed. However, wind farms tend to put the wind turbines relatively close to each other, in an attempt to maximise the energy extracted from a given site. Variation of wind incidence means that the wake of a wind turbine can impact onto following ones [9, 10]. Typical power loss due to wake-turbine interaction is reported to be of the order of $10 - 20\%$ [9] and can reach up to 40% for individual turbines within the farm [10]. Thus, a better understanding of the wake development for serrated trailing edge is needed to assess the impact it may have on this matter. On the other hand, the response of a wind turbine to an impinging wake is key to understanding the variations in its power output, but also its potential early fatigue due to unsteady loading. This means that not only the wake properties are of interest, but also how a turbine reacts to incoming turbulent or unsteady flow.

Schottler *et al.* [65] studied a scale model of an horizontal-axis wind turbine, subjected to intermittent inflows, to study the impact of non-Gaussian wind statistics on the performance of such turbines. They found that the intermittent inflow characteristics resulted in intermittent turbine data. Wachter *et al.* [71] also reported that wind turbines subjected to intermittent inflows generate extreme events in thrust and torque. This means that down to the sub-rotor scales they investigated, the turbines do not filter out the fluctuations but rather translate the incoming flow statistics into similar output statistics. This outlines the importance of the inflow statistics in the tests conducted for various turbines or blades.

Knebel *et al.* [39] have shown that the use of active grids enables the generation of intermittent turbulent flow conditions. Indeed, the authors focused on the possibility to re-create, in a wind tunnel, flow statistics comparable to that found in the atmospheric boundary layer. Their chosen approach was to select the incremental distributions of velocity fluctuations (that is the distribution of $u(t + \tau) - u(t)$ for a given τ) as a means of comparison, and found that by tailoring the way the active grid is controlled, a good match could be achieved.

In the process of studying the technology of airfoils with adaptive camber, a number of studies [19, 37, 22] have looked into the use of an active grid to generate unsteady inflows and therefore unsteady loads. The authors reported that by tailoring the proper control protocol, unsteady loads could be obtained on the airfoils. For example, some protocols were designed to periodically vary the incidence of the flow and therefore simulate a sinusoidal variation of the pitch angle.

These studies highlight the potential for airfoils with a serrated trailing edge to be studied under unsteady inflow conditions and the relevance of doing so. An active grid is an appropriate means to do so.

1.3 Aims and thesis outline

In summary, this chapter has shown that the new approach of cut-in serrations offers the interesting potential of noise reduction but introduces bluntness that modifies the flow due to vortex shedding and therefore produces an extraneous tonal noise. Previous studies on flat plates and airfoils with extension plates have highlighted the importance of flow disruption in the noise production mechanism, and its reduction with serrations. The fluid mechanics are thus key to the performance of the airfoil, even for noise reduction. Furthermore, the behaviour of the wing under unsteady inflow conditions is key for applications such as wind turbines. In light of this, the aims of this thesis are as follows:

- To improve the understanding of how cut-in sinusoidal serrations affect the flow around them and in the wake.
- To explore the potential of geometric modifications to mitigate drawbacks induced by the modification of the flow, and in particular the shedding-associated structures.
- To study such geometric modifications under unsteady inflow conditions.

To tackle these challenges, the thesis is structured as follows. Chapter 2 presents the experimental approach and methodology, and describes the apparatus used for the various experiments. Chapter 3 presents and discusses the results related to sinusoidal cut-in serrations. Chapter 4 looks into new geometries aiming at reducing span-wise coherence and shedding intensity. Chapter 5 investigates the behaviour of wings with such serrations under unsteady turbulent inflows. Finally, concluding remarks and outlines for future work to complement this thesis are offered in chapter 6.

Chapter 2

Experimental methodology

Based on the goals previously listed, a series of experiments has been designed to conduct the relevant investigations. They have been performed at both Imperial College London and the University of Oldenburg.

A NACA0012 wing with a removable TE section is used, following Chong *et al.* [17][14], and Nedić and Vassilicos [51]. The interchangeable trailing edge allows an efficient investigation of various geometries, with the possibility to 3D-print new geometries in a short time. A 3D illustration of the wing with cut-in serrations is given in fig. 2.1.

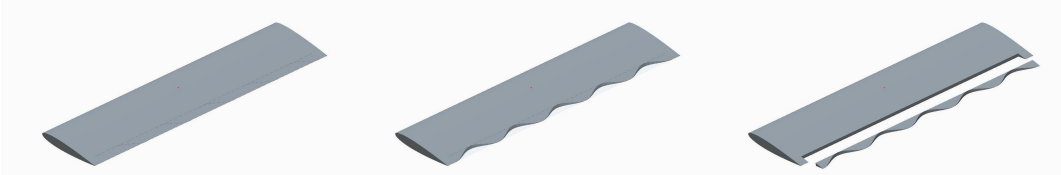


Figure 2.1: Illustration of the wing with cut-in interchangeable trailing edges.

To investigate how the flow is disrupted by the sinusoidal serrations, a combination of hot-wire measurements and Particle Image Velocimetry have been performed. The former provides high temporal resolution and is most suited to spectral analysis of the data, such as obtaining the power spectral density or coherence; and can be quickly traversed across the wake to obtain mean profiles. The latter gives a better spatial overview by encompassing a full field of view, but is more complicated to move across the test section and offers less temporal resolution.

In order to study the behaviour of serrated airfoils under unsteady inflow conditions, an active grid was used to generate bespoke inflows. A force balance was installed to provide information on the dynamics of the lift force.

This chapter is structured as follows: section 2.1 presents the approach followed for the design of the tested trailing edges. Section 2.2 lists the trailing edge parameters investigated at Imperial College and the apparatus designed to do so, both with hot-wire anemometry and particle image velocimetry. Section 2.3 focuses on the experiments conducted with the active grid at Oldenburg University, detailing both hot-wire and force balance apparatus and the trailing edges tested in those cases.

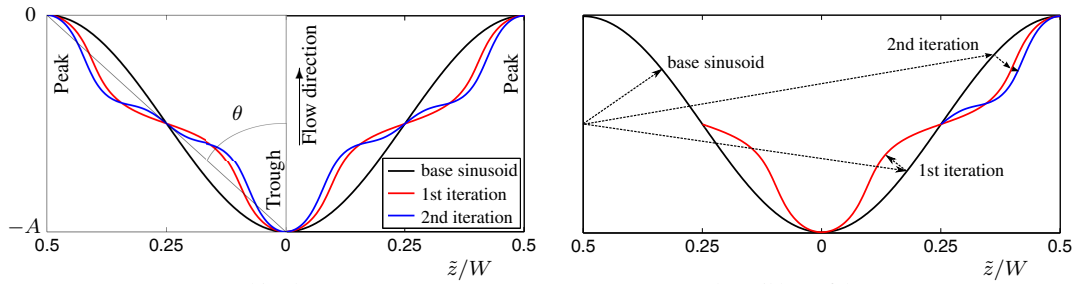
2.1 Trailing edge geometries

This section presents the two approaches followed for the design of the trailing edges. The parameters used in the experiments are detailed in tables 2.1 & 2.3 for the apparatus used at Imperial College and Oldenburg University, respectively.

2.1.1 Blunt trailing edges: sinusoidal and multiscale

As previously mentioned, the first step in the study of the serrations is to use sinusoidal cut-in serrations. The simplicity of this geometry offers a better understanding of the flow structure, and they do not exhibit sharp angles. Such patterns correspond to the "base sinusoid" in fig. 2.2. To obtain multiscale patterns and explore their potential to breakdown coherent structures shed by the serrations (cf chapters 3 & 4), stronger span-wise variation was needed. Furthermore, as discussed in the introduction, previous studies had illustrated the potential effect of multiscale/fractal geometries in the reduction of vortex shedding intensity.

The approach chosen here is to create multiscale sinusoidal patterns, not in the sense of a Fourier sum, but by adding the variations on the previous curve. In a few words, they correspond to the iterative addition of a sinusoidal curve normally to the previous one. This process is illustrated in fig. 2.2b. In practice, the curves were generated with a Matlab script: for each point of the original curve, a new displaced point was created, based on the local tangent to the original curve. The displacement was varied sinusoidally, with odd harmonics, that is to say the simple sinusoidal curve was made with a plane cosine function of frequency 1, increased to 3 and 5 for the one and two iterations patterns, respectively. To find a balance between having significant perturbation of the curves and keeping a smooth evolution, the ratio between



(a) Multiscale patterns

(b) Build-up of the patterns

Figure 2.2: Illustration of multiscale patterns used for the trailing edges. A is the amplitude of the cut-in serrations.

successive amplitudes was set at 0.25. Finally, the patterns were scaled down to $[-1, 1]$, so that the peaks and troughs extrema would not be affected. One should note that the constraint on the amplitude gives the appearance of having used the harmonics 1, 2 and 4, while it was indeed 1, 3 and 5 as previously stated.

2.1.2 Sharp trailing edges

Because of the cut-in approach, the trailing edges exhibit bluntness in the troughs. One option to mitigate the drawbacks (cf chapter 3) of such bluntness is to introduce a geometry that will maintain a sharp trailing edge on the serrations. The idea is illustrated in fig. 2.3 and in table 2.1, where instead of cutting into the trailing edge, its aft part is modulated so that the sharp end will follow a sinusoidal variation of amplitude A. Therefore, the profile at the peaks will be an unmodified NACA0012, while at the trough the part after $0.83c$ will steeply converge towards the sharp edge. This approach creates a wavy surface along the aft part of the trailing edge.

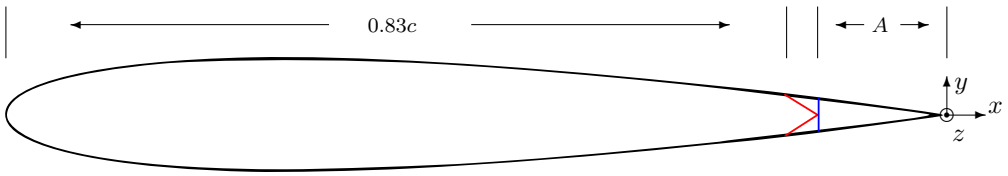


Figure 2.3: Side sketch of blunt (blue) and sharp (red) sinusoidal trailing edges.

2.2 Apparatus at Imperial College London

For the experiments conducted at Imperial College London, the wing itself has a chord $c = 150\,\text{mm}$, the boundary layer is tripped at $0.2c$ by a 5 mm wide single strip of sand paper on both upper and lower surfaces, and the removable trailing edge section covers 92% of the $455\,\text{mm}$ span. Both the main body of the wing and the trailing edges are 3D printed in plastic (Rigur RGD450®). The wing is placed at a 5° angle of attack which produces moderate lift with a large margin to stall.

Experiments have been conducted in two low speed wind tunnels in the Department of Aeronautics. The test section in both tunnels measures $455 \times 455\,\text{mm}$ and the background turbulence intensities were measured to be 0.15%. The tunnel speeds were set with a PID controller to match $Re_c = 150,000$.

Details of the trailing edges studied in these experiments are given in table 2.1.

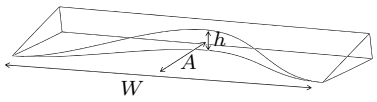
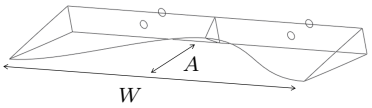
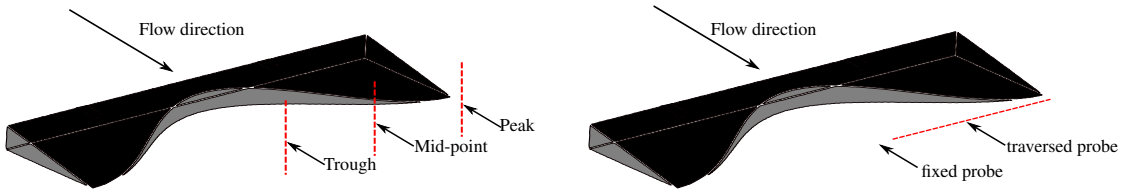
Name	Iteration	A [mm]	W [mm]	Bluntness	Illustration
$S20W84B$	none	20	84	blunt	
$1iS20W84B$	1	20	84	blunt	
$2iS20W84B$	2	20	84	blunt	
$S20W40B$	none	20	40	blunt	
$1iS20W40B$	1	20	40	blunt	
$2iS20W40B$	2	20	40	blunt	
$S20W00B$	none	20	N/A	blunt	
$S20W84S$	none	20	84	sharp	
$S20W40S$	none	20	40	sharp	
$S00W00S$	none	00	N/A	sharp	
Nomenclature for $\sim S$—W__†: $\sim$ iteration **S**ine patterns, A=—[mm], **W**=__[mm],†**B**lunt or **S**harp					

Table 2.1: Trailing edges used at Imperial College with geometric parameters.



(a) vertical traverses

(b) spanwise traverses

Figure 2.4: Hot wires locations for the two types of traverses, conducted at various downstream positions.

2.2.1 Hot-wire measurements

To perform vertical traverses, a custom probe holder was manufactured for each TE wavelength, to position three hot wires downstream of the peak, trough and mid-point (quarter wavelength from the trough), as illustrated in fig. 2.4a. Cross-stream traverses were then performed to cover the full vertical extent of the wake and study its downstream evolution. These measurements were conducted at different downstream position, corresponding to $x/c = \{0.04\,;\ 0.12\,;\ 0.2\,;\ 0.4\,;\ 0.6\,;\ 1.2\,;\ 1.6\,;\ 2\,;\ 3.2\}$, where $x/c = 0$ is the tip of the unmodified trailing edge.

Three gold plated Dantec 55P01 hot-wires were used, connected to a Dantec StreamLine 90N10-Frame CTA powered by an isolated power supply. The square wave responses of the hot wires were all above $40\,$kHz, while a low-pass filter was set at $30\,$kHz. The sampling frequency of $100\,$kHz ensures that Shannon's principle is respected to avoid aliasing. Acquisition at each point lasted for $30\,$s to allow convergence of the statistics, covering about $16,000$ shedding cycles. The over heat ratio was set at 1.8. Calibration was performed before each traverse, with a range of free-stream velocities spanning from $8\,$m/s ($Re_c = 75,000$) to $23\,$m/s ($Re_c = 225,000$). The size of the sensing wire is $l_{hw} = 1.25\,$mm, and to get an insight of how it scales with regards to the flow, one can use the following approach. The longitudinal one-dimensional spectra $E_{11}^{(1)}(k_1)$ can be used to give an expression of the Taylor length scale λ_1 as [7]

$$\left(\frac{1}{\lambda_1}\right)^2 = \int_0^\infty \frac{K_1^2 E_{11}^{(1)}(k_1)}{\overline{u_1'^2}}.$$

Assuming the frozen turbulence hypothesis to write $k_1 = f/u_b$ where u_b is a local convective velocity, one can take $u_b = 0.9\,U_\infty$ and $\sqrt{\overline{u_1'^2}} = 0.1\,U_\infty$ from fig. 3.1 to get an estimate of λ_1. Although this approach is inaccurate since neither isotropy nor homogeneity is respected, it gives an estimate of $\lambda_1/l_{hw} = 12$ and therefore indicates that the spatial averaging of the hot-wire sensor is satisfactory. Another way of

discussing this matter is to use the frozen turbulence hypothesis to define a cut-off frequency by $f_c = u_b/(2 * l_{hw})$ to convert the spatial resolution into the frequency space. This gives $f_c = 5.6\,\text{kHz}$, which is well above all phenomena discussed hereafter. It must be mentioned that in the near wake, the stream-wise mean velocity is always sufficient so that the hot-wires read the fluctuations of stream-wise velocity without significant contamination from the span-wise velocity.

To measure span-wise coherence, phase shifts and vortex shedding intensity, two-point span-wise traverses were performed in the wake: one hot-wire being fixed downstream of a trailing edge's trough, corresponding to the centreline, while a second was traversed in the span-wise direction, as illustrated in fig. 2.4b. These measurements were conducted at different downstream position, corresponding to $x/c = \{0.04\,;\, 0.12\,;\, 0.2\,;\, 0.4\,;\, 0.6\,;\, 1\,;\, 1.4\,;\, 1.6\,;\, 2\,;\, 3.2\}$, where $x/c = 0$ is the tip of the unmodified trailing edge.

Two gold plated Dantec hot-wires were used (one 55P01 and one 55P05), with the sensing wire orientated vertically to allow for smaller separation between them. The minimum separation for the different traverses is $1.5 - 2\,\text{mm}$, and $\overline{U}$ and $\sqrt{\overline{u'^2}}$ were monitored when moving the probes together to ensure there was no aerodynamic probe interference. Acquisition at each point lasted for $40\,\text{s}$ to allow convergence of the statistics and the rest of the technical parameters are as reported for the vertical traverses.

2.2.2 Boundary layer measurements using hot-wires

Hot-wire measurements were conducted close to the airfoil's surface to determine the boundary layer displacement thickness at the roots of the serrations. The initial position of the probe was controlled by a microscope, and the closest distance to the wall was of the order of $200\,\mu\text{m}$. For the blunt serrations, this initial position was $1\,\text{mm}$ upstream of the cut at the trough, while for the sharp serrations, the initial position was $1\,\text{mm}$ upstream of the point where the surface angle changes ($0.83c$ point in fig. 2.3). The probe was then vertically traversed away from the airfoil, with initial steps of $20\,\mu\text{m}$ (minimum step to ensure accuracy of the traverse rig), followed by a logarithmic spacing then a linear spacing to cap the traverse separations.

A Dantec gold plated boundary layer probe (55P05) was used with a Dantec StreamLine 90N10-Frame CTA. Acquisition was run at $100\,\text{kHz}$ for $60\,\text{s}$ per measurement location. Calibration of the probes was done with a velocity range from $0\,\text{m/s}$ to $21\,\text{m/s}$ and a Kings law was used to fit the data. One should note that setting the wind tunnel flow velocity in the range of $1\,\text{m/s}$ to $5\,\text{m/s}$ is not straightforward, hence in this range the focus was put on stabilising the velocity and measuring its real value rather than targeting a

specific value.

2.2.3 PIV: cross-stream 2D-3C

Stereoscopic Particle Image Velocimetry (PIV) was conducted in a span-wise/cross-stream ($y-z$) plane, $x/c = 0.04$ downstream of the trailing edge. Fig.2.5 illustrates the field of view (94×59 mm) which is normal to the stream-wise direction and encompasses a full wavelength of $S20W84B$.

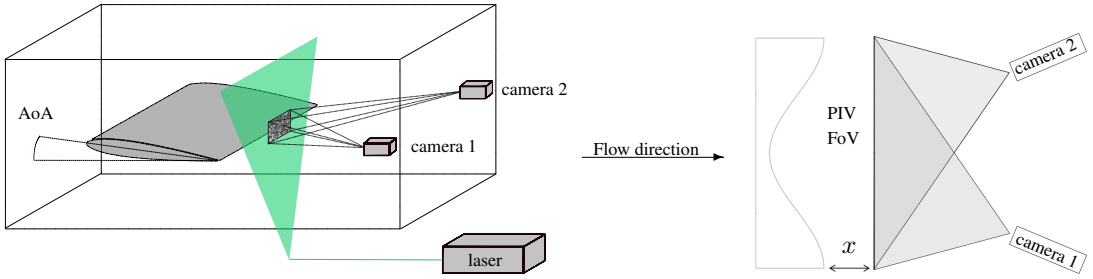


Figure 2.5: Sketch of the cross-stream PIV (2D-3C) apparatus. Left: 3D view, right: top view.

The illumination was made using a Litron LDY300 (Nd:YLF) laser, and two Phantom M310 cameras (25.6×16.0 mm/1280×800 px sensors) with Nikon *135* mm *f/2 DC* lenses were used for imaging. The illumination and imaging set-up was controlled by the commercial software LaVision's Davis 8.2. Data was acquired at 250 Hz with a double frame separation time of 12 μs.

The tunnel was seeded with a water/glycol (4:1) solution with particle diameters $d_p = 2-3\,\mu$m. Stokes number, defined as

$$St_K = \frac{t_0 U_{rms}}{l}; \text{ where } t_0 = \frac{\rho_p d_p^2}{18\mu_f}, \tag{2.1}$$

with U_{rms} the local standard deviation of velocity, ρ_p the particle density, μ_f the fluid dynamic viscosity and l the PIV spatial resolution. This gives a value of $St_K = 0.02$, within the $St_K << 1$ range, which is the criteria for particles to behave as tracers.

Images were pre-processed to subtract the background luminosity, and a sliding background average was applied to account for non-uniformity in the illumination. Recursive processing was done with an initial window size of 64×64 px, final window size of 32×32 px and 75% overlap, giving a spatial resolution of 1.8 mm. The velocity vector fields were then post-processed to remove spurious vectors, with rejected vectors being fewer than 1%.

2.2.4 PIV: span-stream 2D-2C

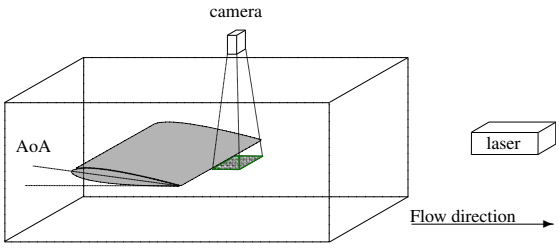


Figure 2.6: Sketch of the span-stream PIV (2D-2C) apparatus

Planar (2D-2C) Particle Image Velocimetry (PIV) was conducted in a span-wise/stream-wise plane ($x - z$), with a field of view encompassing the largest TE wavelength. Fig. 2.6 illustrates the apparatus.

Illumination and imaging was made using the same equipment as previously described, giving a laser sheet thickness of 0.5 mm, with only one camera. Data were acquired at 1500 Hz with an inter-frame separation time of $12\,\mu$s. The horizontal laser sheet was placed 1 mm under the tip of the non-modified trailing edge, thus being under the wing at the maximum amplitude of the cut-in patterns, and in the middle of the wake right after the trailing edge.

Seeding was done as previously described, which gives here a Stokes number $St_K = 0.03$, indicating the particle behave as tracers.

Images were pre-processed to subtract the background luminosity, and a sliding background average was applied to account for non-uniformity in the illumination. Recursive processing was done with an initial window size of 48×48 px, final window size of 16×16 px and 50% overlap, giving a spatial resolution of 1.2 mm. The velocity vector fields were then post-processed to remove spurious vectors with a universal outlier method, with processed/rejected vectors being within $2 - 2.5\%$.

Experiment	Acq. rate	Initial/Final window size	overlap	spatial resolution
cross-stream 2D-3C	250 Hz	64×64 px / 32×32 px	75%	1.8 mm
span-stream 2D-2C	1500 Hz	48×48 px / 16×16 px	50%	1.2 mm

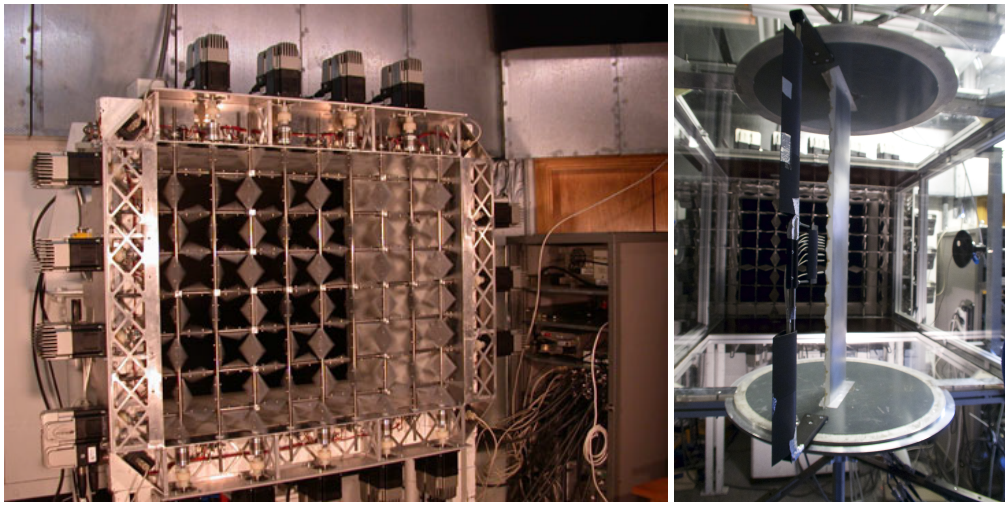
Table 2.2: Key parameters of the two PIV set-ups.

2.3 Apparatus at ForWind - University of Oldenburg

2.3.1 Active grid and wing

Experiments were conducted in a wind tunnel equipped with an active grid at the University of Oldenburg in Germany. The active grid was developed to pursue research in atmospheric turbulence, and re-create similar statistics in wind tunnels, as presented by Knebel *et al.* [39]. The active grid used in this study is made of 9 vertical and 7 horizontal axes, independently controlled by stepper motors with a maximum speed of $900°s^{-1}$, on which a total of 126 square flaps are mounted, as illustrated in fig. 2.7a. Fig. 2.7a shows the former active grid that has since then been updated with more streamlined attachments and junctions between the flaps and axes and was also designed and tested by the research team at ForWind & Institute for Physics.

The active grid is controlled by a protocol, that is a time series of positions, sent to the stepper motors to move the different axes. All protocols presented hereafter use the vertical axis only, and the horizontal ones are fixed with the flaps aligned with the flow. For repeatability of the measurements, a triggering signal is added to the protocols, so that measurements always start at the same time.



(a) (b)

Figure 2.7: Active grid from Knebel [39] (a) and current set-up (b), as sketched in fig. 2.4a.

The wind tunnel has a $1.0\,\text{m}\times0.8\,\text{m}$ closed test section with a length of $2.6\,\text{m}$. The wing was installed vertically $1.1\,\text{m}$ downstream of the grid, with a span of $0.8\,\text{m}$ and a chord of $0.2\,\text{m}$, as illustrated in fig. 2.7b. These specifications were scaled to match existing attachment plates at the roof and floor of the test section, that can rotate to change the pitch of the wing. Given the variation in time of the grid blockage during the protocol, the wind speed is not controlled with a PID but by imposing constant voltage to the wind tunnel fan. With all flaps aligned with the flow, this gives an incoming velocity of $22\,\text{m/s}$ and a chord-based Reynolds number of $Re_c = 280,000$.

By rotating the plate, the pitch angle of the wing is varied from 0° to 20° by steps of 2°. A Kuebler 5850 series encoder is used to control this pitch angle, while the plates are rotated by two motors at both the roof and floor of the test section to limit the torque imposed on the wing.

The wing itself follows the previous approach of having a main body and interchangeable trailing edges. The profile is also a NACA0012, with span $805\,\text{mm}$ and chord $200\,\text{mm}$ as previously mentioned. The main part was manufactured in Germany, milled out of aluminium with a roughness under $0.8\,\mu\text{m}$, over 70% of the chord, the aft part being 3D printed and fixed with a lap joint as illustrated in fig. 2.8. This airfoil's boundary layers were not tripped.

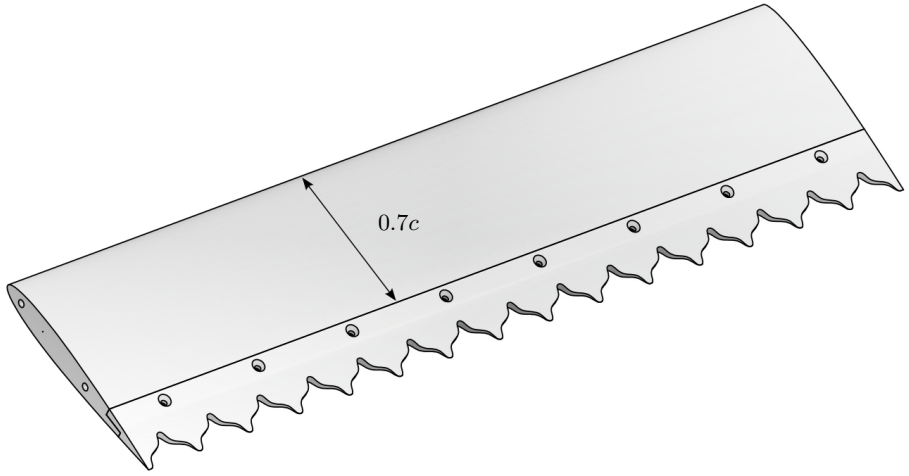


Figure 2.8: Drawing of the manufactured wing.

The trailing edges fitted to this wing correspond to the up-scaling of those tested at Imperial College

(see table 2.1) by a factor $4/3$ to adapt to the new chord. To limit the number of test cases, the short wavelength of 40 mm corresponding to a serration angle of $45°$ was chosen based on the results presented in chapters 3 & 4. The relevant parameters are listed in table 2.3.

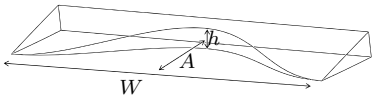
Name	Iteration	A [mm]	W [mm]	Bluntness	Illustration
$S20W40B^*$	none	26.7	53.3	blunt	
$1iS20W40B^*$	1	26.7	53.3	blunt	
$2iS20W40B^*$	2	26.7	53.3	blunt	
$S20W00B^*$	none	26.7	53.3	blunt	
$S00W00S^*$	none	00	N/A	sharp	
Nomenclature for $\sim S$—W__†*: $\sim$ iteration **S**ine patterns, A=—[mm], **W**=__[mm],†**B**lunt or **S**harp. The symbol * denotes the scale-up from the ones used at Imperial College.					

Table 2.3: Trailing edges used in Oldenburg's wind tunnel with geometric parameters.

2.3.2 Hot-wire measurements

A custom probe holder was manufactured, to position all 8 hot-wire probes at $0.04c$ downstream of the trailing edge, fixed on the rotating plate so that it follows the rotation of the wing. The span-wise positions of the probes matched the patterns of the serrations, covering $1.5W$ as depicted in fig. 2.9b.

The hot-wire probes were Dantec model 55P11 miniature wire probes, connected to a mini-CTA. The acquisition was run at 10 kHz for 45 s simultaneously for all 8 probes, thus allowing the study of coherence between signals. Those sensing wires have a length of $l_{hw} = 1.25$ mm as well, and following the same approach as presented before, assuming frozen turbulence hypothesis leads to a cut-off frequency of $f_c = 8$ kHz, which is above the 5 kHz limit imposed by the acquisition frequency. Calibration was done by moving the probe holder away from the airfoil's wake and fitting two Pitot sensors alongside the hot-wires.

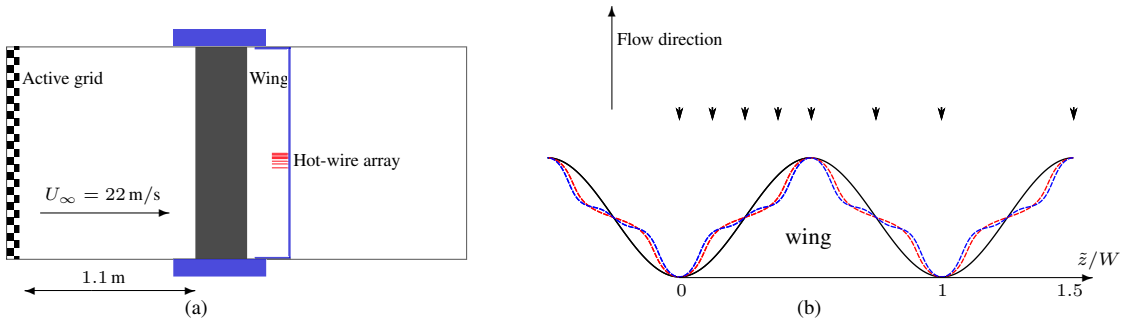


Figure 2.9: Sketch of the hot wire measurements set-up: side view of the wind tunnel (a) and position of the probes relatively to the serration patterns (b).

2.3.3 Force measurements

Aerodynamic forces were measured using two ME Systeme K3D120 3-component load cells fixed on the wing's rotating axis. An offset measurement was performed prior to acquisition to subtract static loads created by the installation. Acquisition was run at 1 kHz for the whole duration of the protocols. This set-up was designed by the research team at Oldenburg, and has been reported in previous studies [22] [37].

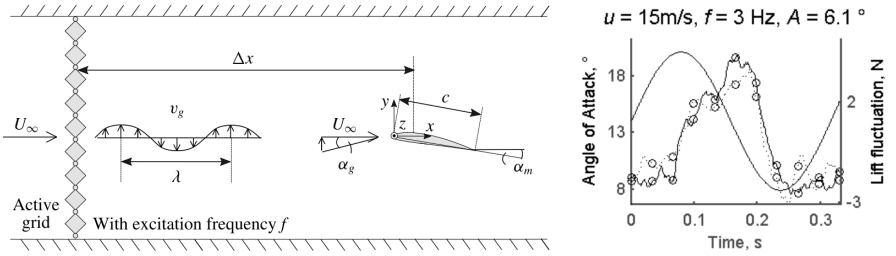
2.3.4 Protocols

The protocols are the control sequences sent to the active grid. They consist of an array of time series of angular positions, one series for each stepper motor, that independently activate the axis and therefore allow for a wide range of possible movements. The outcome is an inflow that is dynamically modulated during the experiments, and can recreate flow statistics similar to that of real world wind field [39] or enable dynamic change of the load imposed on an airfoil [22] [37]. The experiments conducted for this thesis used four protocols, described hereafter.

Sinusoidal protocol

The sinusoidal protocol creates a variation of the effective angle of attack of the pitched airfoil. Indeed, all vertical axes (parallel to the span-wise direction) sinusoidally oscillate with a pre-determined phasing so as to not create high blockage, and rather alternately redirect the flow to each side of the test section. Such

protocols have previously been used to study the dynamic load response of an airfoil, as reported by Cordes *et al.* [19] and Fischer *et al.* [22], with a frequency of oscillation in the range of 2 Hz to 6 Hz and amplitude from $2°$ to $8°$. The authors have used cross hot-wires to study the variation of the angle of the flow in the wind tunnel prior to the installation of the airfoil, at seven vertical position. They report a good match of both frequency and amplitude of the angle variations with that imposed on the grid. Fig. 2.10b illustrates the lift responses of two wings to a slightly different sinusoidal protocol than that used in the present work [18].



(a) Illustration of the sinusoidal protocol, top view of the test section. From [20].

(b) Example of lift fluctuations under a sinusoidal protocol. From [18].

Figure 2.10: Illustration and lift output of a sinusoidal protocol.

The reduced frequency associated to this protocol, defined as $k = \frac{\pi * f_{flaps} * c}{U_\infty}$, gives a value $k = 0.07$ which indicates unsteady aerodynamics.

"45 degree" protocol

The "45 degree" protocol uses the active grid to create a high blockage on the centre line. The three vertical middle axes are positioned around a mean value of $45°$ and oscillate at 25 Hz with an amplitude of $5°$. The aim of this protocol is to create a turbulent wake with high vertical (span-wise) extent of correlation at a given frequency, and let it impinge onto the airfoil.

Gaussian protocol

One of the main ideas behind the tailoring of flows with given statistical properties is that the mean and standard deviation alone cannot fully describe the impact of the flow on, say, a wind turbine load. Indeed, two flows can have the same mean velocity and the same standard deviation of velocity fluctuations, with

different distributions of the latter. As discussed in the introduction, the characteristics of the distribution (e.g. high intermittency) will be observed in the turbine output as well. This is why the distribution of the fluctuations, either Gaussian or non-Gaussian (heavy-tailed) is of interest and has been studied for wind turbine applications [65]. The present work studies the impact of two protocols on the statistics of lift, with the first protocol of interest making the flaps constantly rotate, with a Gaussian distribution of their angular positions.

Intermittent protocol

The so-called intermittent protocol makes the flaps lightly oscillate parallel to the flow with non-regular strong motions to re-create gusts. The distribution of the flaps' angular positions is therefore non-Gaussian, and thus so is the distribution of the velocity fluctuations in the created inflow.

These protocols are intended to give different distribution of lift, but also different incremental distributions. The former reflects the statistics of the values of lift, while the latter shows the distribution of lift variation for a given time lag (increment) and therefore reflects the abruptness of load variations. Both Gaussian and Intermittent protocols have been designed by the research team at Oldenburg and are not yet reported in published studies.

Chapter 3

Sinusoidal serrations

The results presented in sections 3.1, 3.2 and 3.3 have been published in the following article: S.L. Prigent, O.R.H. Buxton and P.J.K. Bruce, "Wake of a lifting wing with cut-in sinusoidal trailing edges", AIAA Journal, 55(5):15901601, May 2017. Section 3.5 is part of an article submitted to the journal *Physics of Fluids* as: S.L. Prigent, O.R.H. Buxton and P.J.K. Bruce, "Coherent structures shed by multiscale cut-in trailing edge serrations on lifting wings", *Physics of Fluids*, under review.

3.1 Mean properties

The first step into the characterisation of the wake is the investigation of single-point statistical properties such as mean velocity and standard deviation, to offer an overview of the wake in terms of velocity deficit, turbulence intensity and their homogeneity. The introduction discussed the interest of a better knowledge of such properties in applications where the wake impinges on another blade. They also highlight the presence of dynamical phenomena that will be discussed in the subsequent sections.

Mean velocity profiles, obtained from hot-wire anemometry measurements behind the trough ($\tilde{z}/W = 0$), peak ($\tilde{z}/W = 0.5$) and mid-point ($\tilde{z}/W = 0.25$), are plotted in fig. 3.1a for wing $S20W84B$ at $x/c = 0.04$. The three profiles collapse on the whole traverse except at the centre of the wake, where the maximum velocity deficit exhibits a span-wise dependence. One also notices that the mean velocity recovers to the free stream under the wing, within a margin of 0.5%, while an increase of up to 7% is observed above the wing (out of plot range in fig. 3.1a). This is expected as the wing is a lifting body and

hence generates an increase of the speed above the wing. This effect is thought to be further increased by the proximity of the upper wall of the wind tunnel (located at $y/c = 1.5c$). Fig. 3.1b shows the turbulence intensity profiles of the three span-wise locations. The trough's profile shows a higher turbulence intensity as well as a wider shear layer.

It is logical to expect higher turbulence intensity in the wake of the trough, because it is blunt, however it would also be expected to have a higher velocity deficit, contrary to what is observed in fig. 3.1a. This observation is partly attributed to the alignment of the hot wires that gives a longer distance for the wake to develop downstream of the troughs than downstream of the peaks. Using a corrected downstream position, x^* defined as $x^* \equiv (x + A(z))$, hence allows comparison of these span-wise positions without the bias of this downstream offset.

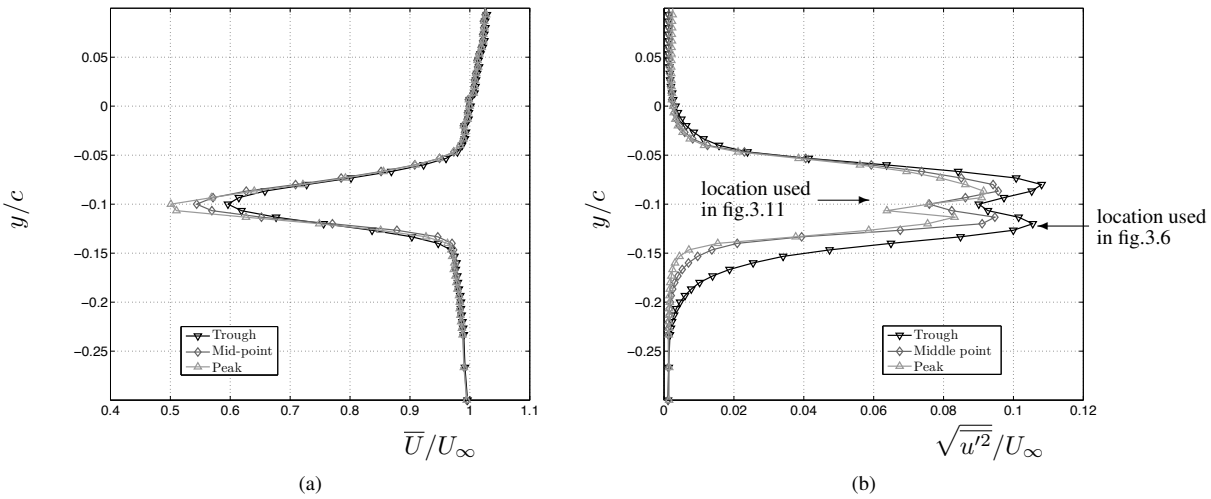
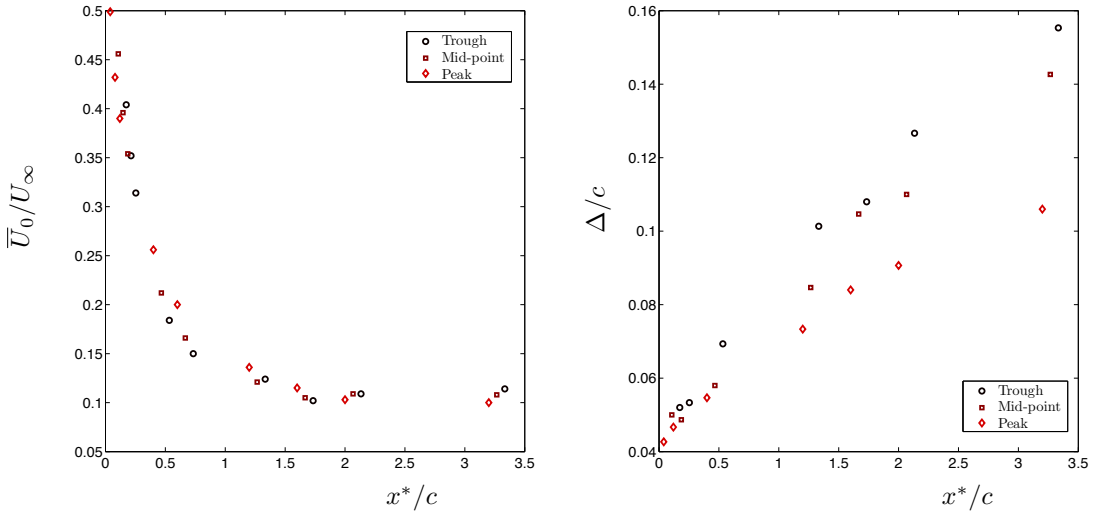


Figure 3.1: Mean (a) and RMS (b) wake velocity profiles at $x/c = 0.04$ for three span-wise locations behind $S20W84B$.

Fig. 3.2 shows the downstream evolution of the maximum velocity deficit, $\overline{U}_0$, and the semi-wake width, Δ, at the three span-wise locations, based on x^*. The semi-wake width is defined as the width of the wake at half of its maximum velocity deficit, following Hah *et al.* [28].

Fig. 3.2a shows that for $0.25 < x^*/c < 1.75$, the velocity deficits are all very similar. However, the wake widths, plotted on fig. 3.2b, are higher for the trough than for the peak, for the whole range of

downstream positions. Although the trend of velocity deficit for the mid-point's wake is hard to distinguish from the trough, the wake width clearly lies between the peak and trough. Since the wake inhomogeneity is persistent far downstream, it is not possible to solely explain the difference with the downstream distance offset, and another explanation must be given.



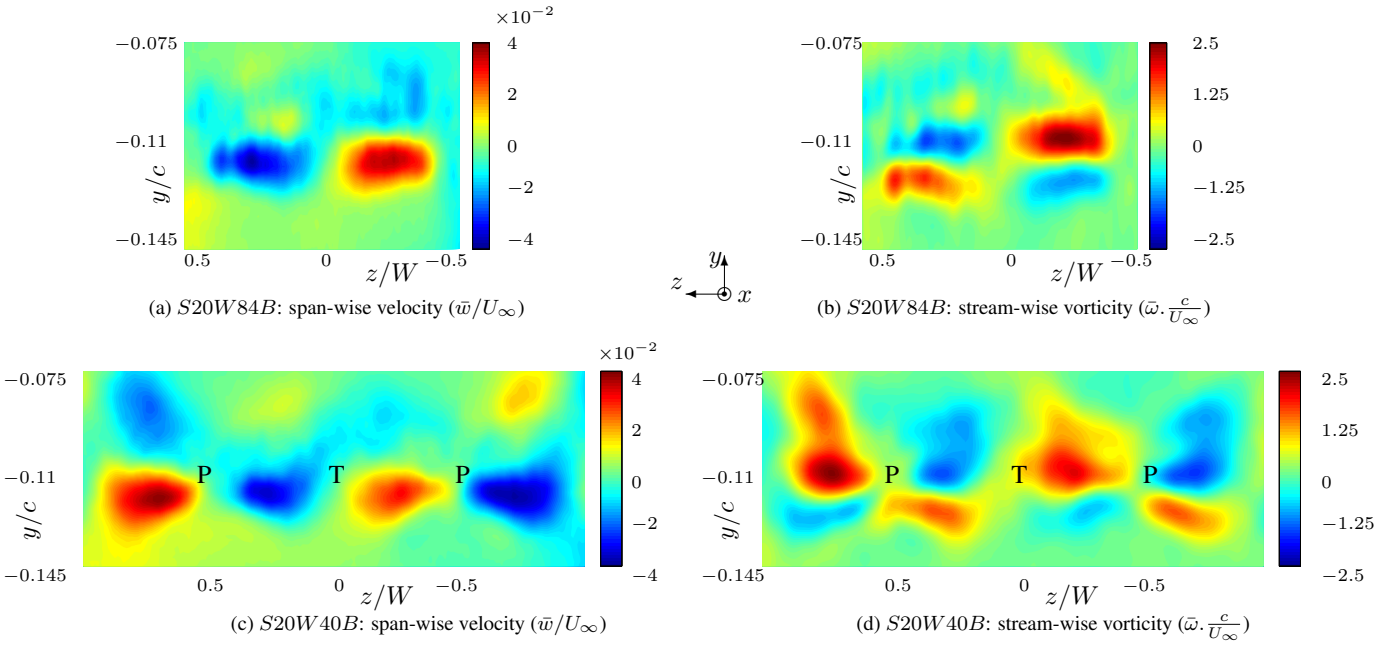
(a) (b)

Figure 3.2: Downstream evolution of maximum velocity deficit (a) and semi-wake width (b) at three span-wise locations for $S20W84B$.

Fig. 3.3 shows $y-z$ planes of span-wise mean velocity and stream-wise mean vorticity, obtained from the PIV measurements, downstream of $S20W84B$ and $S20W40B$ at $x/c = 0.4$. The main feature is the existence of stream-wise vorticity as illustrated in fig. 3.3b and 3.3d, which induces a span-wise flow from under the peaks towards the troughs. However, the counter flow that one could expect from above the trough toward the peak is much weaker, which indicates that overall the added span-wise component tends to push the flow into the troughs. Although the span-wise flow covers a high vertical extent for $S20W40B$, both cases display very similar patterns and show a good repeatability between successive peaks for $S20W40B$.

The pressure difference between the pressure and suction sides of the lifting wing explains the creation of this span-wise flow on the sides of the cut-in sinusoids. In turn, this flow would re-energise the wake behind the trough while increasing the velocity deficit behind the peak. This flow structure is consistent

with the behaviour observed in fig. 3.2.



(a) $S20W84B$: span-wise velocity ($\bar{w}/U_\infty$)

(b) $S20W84B$: stream-wise vorticity ($\bar{\omega}.\frac{c}{U_\infty}$)

(c) $S20W40B$: span-wise velocity ($\bar{w}/U_\infty$)

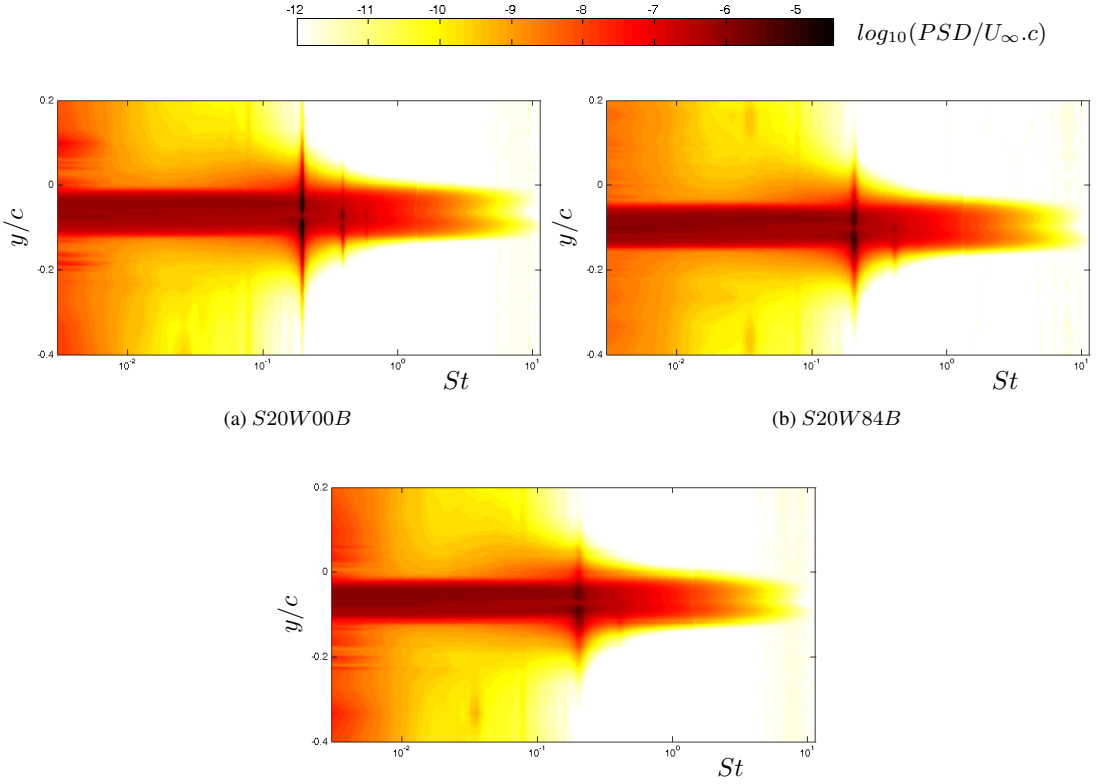
(d) $S20W40B$: stream-wise vorticity ($\bar{\omega}.\frac{c}{U_\infty}$)

Figure 3.3: PIV maps of mean velocity span-wise component and mean stream-wise vorticity at $x/c = 0.4$. TE peaks (P) and troughs (T) locations indicated on the maps.

In summary, fig. 3.2 and 3.3 show that the mean properties exhibit a clear and persistent inhomogeneity of the wake in the span-wise direction, due to a peak-to-trough spanwise flow.

3.2 Spectral analysis

Given that we introduce bluntness in the trailing edge, an important question is the identification of unsteady shedding phenomena, and whether the previously discussed span-wise inhomogeneity is also clear in this aspect. Firstly, three TEs with the same maximum bluntness are investigated: the straight blunt and two wavelengths of blunt sinusoidal TEs. Fig. 3.4 displays maps of spectra for vertical traverses at the same downstream position, $x/c = 0.04$ behind the troughs of $S20W00B$ (3.4a), $S20W84B$ (3.4b) and $S20W40B$ (3.4c). The value plotted is the Power Spectral Density (PSD) normalised by $U_\infty.c$, a product of two external parameters which allows direct comparison between different cases. The Strouhal number,



(a) $S20W00B$

(b) $S20W84B$

(c) $S20W40B$

Figure 3.4: Vertical PSD log_{10} map at $x/c = 0.04$ behind the TEs troughs

St, is based on the maximum bluntness in the trough, $h = 5.5\,\text{mm}$, similar to the study of Tombazis & Bearman [69].

Fig. 3.4 shows a clear shedding at $St = 0.18$ for $S20W00B$. Shedding intensity is seen to depend on the TE wavelength: the second harmonic is visible on fig. 3.4a for $S20W00B$ while for $S20W84B$, fig. 3.4b shows a milder main peak and only the first harmonic is visible. For the shortest wavelength, the main peak is again milder while the first harmonic has almost disappeared from fig. 3.4c. To quantify this trend, one can define the energy associated with the shedding in the wake - similarly to Rind & Castro[57] and Nedić et al. [50] - by:

$$E_{sh} = \int_{\mathbb{Y}} \int_{St_{sh}(1-\Delta St/2)}^{St_{sh}(1+\Delta St/2)} \frac{PSD}{U_\infty.c}\, dSt\, d\frac{y}{c}, \tag{3.1}$$

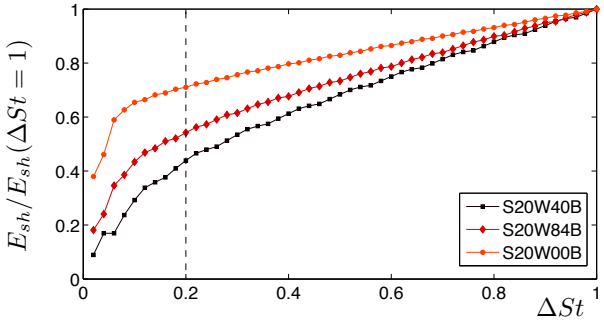


Figure 3.5: E_{sh} sensitivity to ΔSt.

with $\mathbb{Y}$ being the extent of the vertical traverse, ΔSt the range of Strouhal number over which to integrate and St_{sh} the vortex shedding value of St. The value $\Delta St = 0.2$ is chosen after a sensitivity analysis, illustrated in fig. 3.5, and corresponds to the value at which the evolution of E_{sh} becomes linear with ΔSt.

Comparing the shedding intensity at the trough for the two wavy cases with a straight blunt trailing edge shows how waviness impacts the effects of bluntness, via the cut-in approach to modifying the trailing edge. With the above definition, the energy associated with shedding shows a reduction of 39% between $S20W00B$ and $S20W84B$, and 57% between $S20W00B$ and $S20W40B$. It is clear that the shorter wavelength has a stronger reduction of shedding intensity; however, it is important to keep in mind that both cases have relatively large serration angles of at least 45 deg. Chong et al. [14] have studied triangular serrations with angles smaller than 45 deg and observed that the smallest wavelengths produced higher noise level at the shedding frequency. In terms of noise reduction, a trade-off should thus be sought, although this study focuses on the fluid mechanics side of the matter.

Fig. 3.4 shows a slight asymmetry in the wake since the shedding is stronger in the lower half, corresponding to the part of the wake downstream of the pressure surface. This is particularly visible in the harmonics for the $S20W84B$ and $S20W40B$ cases. This observation is consistent with the presence of a more energetic (vortical) flow structure observed in the lower half of the wake in fig. 3.3.

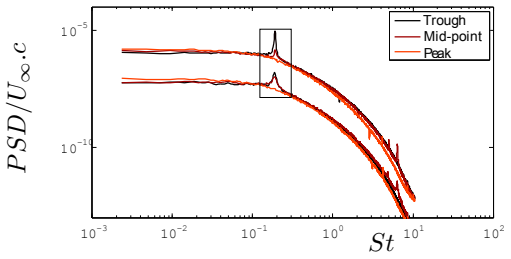
The span-wise inhomogeneity of the mean flow seen in fig. 3.1, 3.2 and 3.3 is also expected in the spectra, as the troughs, mid-points and peaks inherently exhibit different physical phenomena. Fig. 3.6a shows individual spectra measured at $x/c = 0.04$ downstream of $S20W84B$ and $S20W40B$ at three span-wise positions, with a vertical shift for ease of representation. To allow a fair comparison of spectra, at each span-wise location, the vertical position is taken to match the lower peak in the turbulence intensity

profiles, as illustrated in fig. 3.1b. Although the spectra downstream of the trough in fig. 3.6a clearly contain energy in a narrow shedding band, the spectra downstream of the peak does not show a clear shedding peak at all. Fig. 3.6b shows that further downstream, at $x/c = 2$, there is still a difference in the global shape of the spectra between trough and mid-point on one hand and peak on the other hand. This difference is observed even though the shedding spike has almost completely disappeared from all three spectra. Fig. 3.6b also reveals that this difference between spectra downstream of the three span-wise positions is reduced when the wavelength is small. Indeed, the spectra downstream of the trough and the mid-point are almost identical for $S20W40B$ at $x/c = 0.04$, while at $x/c = 2$, there is a good collapse of spectra for all span-wise positions for this case.

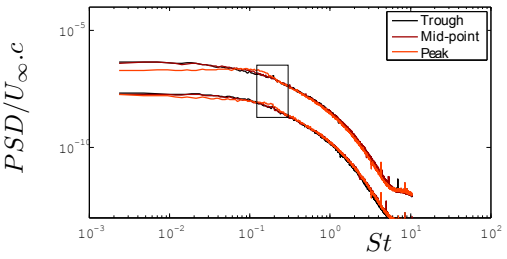
To study how this span-wise variation evolves in the wake, fig. 3.6c shows the downstream evolution of the maximum shedding spike value in the wake of $S20W84B$. The spectra downstream of the peak do not exhibit a shedding spike, hence simply the values of the spectra at St_{sh} are plotted in this figure. As previously observed, the shedding intensity is higher behind the trough than behind the mid-point close to the trailing edge. This difference vanishes around $x^*/c = 1.5$, after which both shedding intensities stay very similar, and continue to decrease. The farthest downstream points, at $x^*/c > 3$, give a value 2 orders of magnitude lower than the initial value, and indeed the shedding peaks are then barely discernible in the spectra.

One may expect that the TE wavelength will affect the inhomogeneity in the wake, and for this, fig. 3.6d shows the same evolution as fig. 3.6c, with the downstream distance normalised by W instead of c. The PSD values at the shedding frequency are also plotted for $S20W40B$ at two downstream positions. Despite the value of trough and mid-point being closer for $S20W40B$ at small x^*/W values, a large difference between mid-point and peak is also observed. Thus, at comparable x^*/W values, the smaller TE wavelength also exhibits span-wise inhomogeneity.

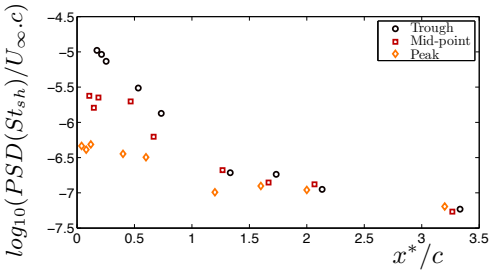
The results presented so far were measured at fixed span-wise locations. Given the strong variations observed, measurements with smaller separations have also been performed. Fig. 3.7 shows the PSD maps of span-wise traverses behind $S20W40B$, $S20W84B$, $S20W00B$ and $S00W00S$ at $x/c = 0.04$. Measurements were done in the middle (cross-stream direction) of the wake, taken as the point of local minimum turbulence intensity. As expected, both straight wings exhibit a span-wisely homogeneous map. Only half of the wavelength is displayed for each case, although symmetry was checked on the full extent of $-1 < \tilde{z}/W < 0$ for $S20W40B$. For both $S20W40B$ and $S20W84B$ the spectral maps show no shedding signature behind the peak ($\tilde{z}/W = -0.5$) and an increasing intensity towards the troughs. One notices



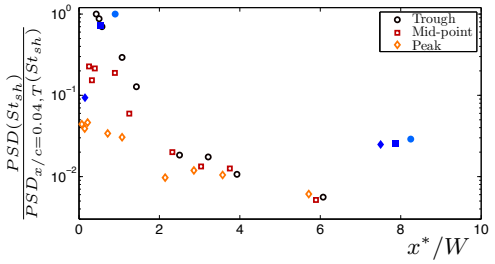
(a) Spectra of $S20W84B$ (top) and $S20W40B$ (bottom) at $x/c = 0.04$



(b) Spectra of $S20W84B$ (top) and $S20W40B$ (bottom) at $x/c = 2$



(c) Downstream evolution of $PSD(St_{sh})$ for $S20W84B$



(d) Downstream evolution of $PSD(St_{sh})$ for $S20W84B$, comparison with $S20W40B$ (blue filled symbols) at two downstream positions normalised by W

Figure 3.6: Spectra at three span-wise positions for $S20W84B$ and $S20W40B$ at $x/c = 0.04$ (a) and $x/c = 2$ (b). Inserts show a zoom around St_{sh}. Downstream evolution of spectra values at St_{sh} for $S20W84B$ (c).

that the trough to peak variation is not monotonic, which is particularly visible in 3.7a. The differences of shedding intensity noted for cross-stream traverses in fig. 3.4 are also visible here, with $S20W40B$ having the lowest intensity.

Given that the peak to mid-point difference in the spectra was observed to reduce from $S20W84B$ to $S20W40B$ in fig. 3.6a, it is interesting to compare an integrated value, taking into account the full wavelength of the pattern to check whether the energy is spread over the wavelength or indeed reduced overall. For this, the value E_{sh} is obtained by integrating around the shedding frequency and along the span-wise direction, similarly to eq. (3.1). When using the normalised value of "$\tilde{z}/W$", the ratio $E_{sh,S20W40B}/E_{sh,S20W84B} = 1.1$ shows an almost equal energy per unit wavelength. However, when using physical units, $E_{sh,S20W40B}/E_{sh,S20W84B} = 0.53$ shows a clear reduction of energy contained within one wavelength. Expressed mathematically, that is to say that

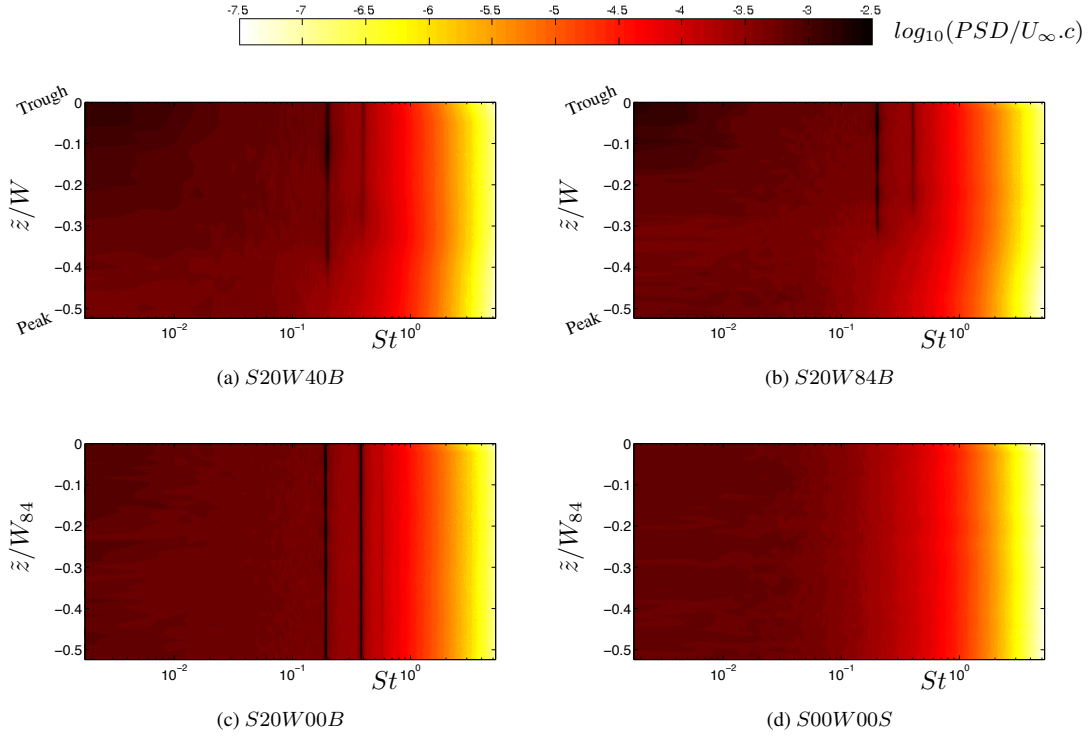
$$\int_0^1 \int_{St_{sh}(1-\Delta St/2)}^{St_{sh}(1+\Delta St/2)} \frac{PSD_{S20W40B}}{U_\infty.c}\, dSt\, d\frac{\tilde{z}}{W} = 1.1 \int_0^1 \int_{St_{sh}(1-\Delta St/2)}^{St_{sh}(1+\Delta St/2)} \frac{PSD_{S20W84B}}{U_\infty.c}\, dSt\, d\frac{\tilde{z}}{W} \quad (3.2)$$

but,

$$\int_0^W \int_{St_{sh}(1-\Delta St/2)}^{St_{sh}(1+\Delta St/2)} \frac{PSD_{S20W40B}}{U_\infty.c}\, dSt\, d\tilde{z} = 0.53 \int_0^W \int_{St_{sh}(1-\Delta St/2)}^{St_{sh}(1+\Delta St/2)} \frac{PSD_{S20W84B}}{U_\infty.c}\, dSt\, d\tilde{z} \quad (3.3)$$

It is thus clear that the total vortex shedding energy produced in one trough is indeed reduced for $S20W40B$ compared to $S20W84B$ and not simply spread over the extent of the TE pattern. Naturally, given the ratio of wavelengths, $S20W40B$ will have more total vortex shedding energy than $S20W84B$ when integrating over the full span of the wing.

Following on the comments made for fig. 3.6 & 3.7, one can also study the span-wise homogeneity of the shedding signal at various downstream positions. For each downstream position, the shedding energy is obtained as a function of z by performing a frequency-only integration, which gives $E_{sh}(z)$ instead of the previously discussed E_{sh}. Fig. 3.8 shows the outcome of these measurements for $S20W84B$ and $S20W40B$. One notices oscillations at $x/c = 0.04$, however this is also visible for the straight blunt trailing edge case. Furthemore, this has not been observed in the wind tunnel study of turbulent boundary layers by Rodriguez-Lopez *et al.* [58]. It could therefore be attributed to an imperfection of the apparatus that could have caused a slight inhomogeneity in the upstream boundary layer, as further discussed in section 3.4. The global trend in fig. 3.8 is to have larger values around the trough ($\tilde{z}/W = 0$) and lower around the peak ($\tilde{z}/W = 0.5$), with the higher levels decreasing when moving downstream. An interesting point is that in both cases, the energy remains in-homogeneously distributed until it reaches low values at



(a) $S20W40B$ (b) $S20W84B$

(c) $S20W00B$ (d) $S00W00S$

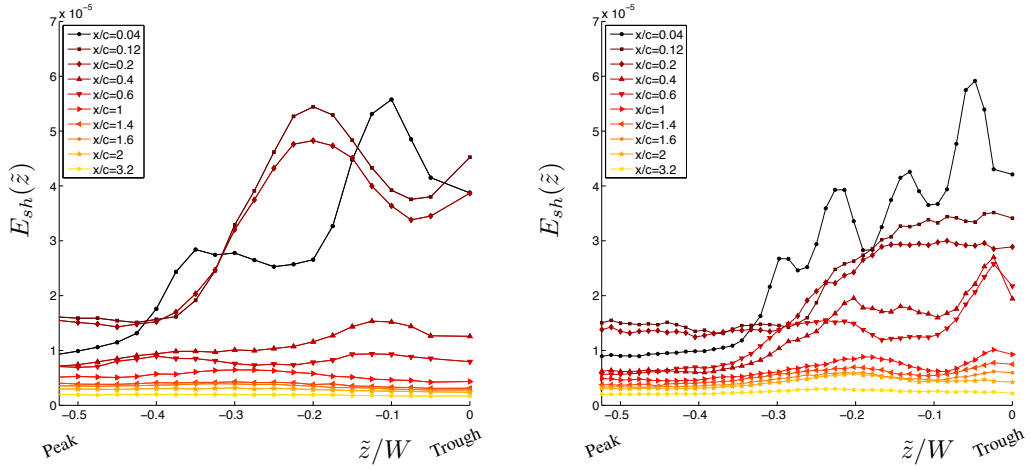
Figure 3.7: Span-wise PSD log_{10} map at $x/c = 0.04$ behind four tested wings.

positions *circa* $x/c = 1.5$, at which according to fig. 3.6 no shedding spike is discernible.

Therefore, the results presented in both fig. 3.6 and fig. 3.8 show that the wakes behind $S20W84B$ and $S20W40B$ do not reach span-wise homogeneity of shedding intensity, even at relatively large downstream distances, where in fact the shedding signal vanishes before this state is reached.

3.3 Coherence

The observation of a distinct shedding in the evolving wake of the wings indicates the possible existence of span-wisely coherent vortex streets which are linked to three topics of interest. Firstly, blunt trailing edges with castellated patterns show a reduction of base drag associated with the conversion of span-wise vorticity into stream-wise vorticity[54], which would translate into partially breaking down the span-wisely coherent vortex street. Secondly, in the case of wake-blade interaction (i.e. blade array, gas turbine, wind farm etc.),



(a) $S20W40B$ (b) $S20W84B$

Figure 3.8: Downstream evolution of span-wise traverses of shedding-associated energy. N.B.: Oscillations at $x/c = 0.04$ are discussed in section 3.4.

such a vortex street might be detrimental as it would impinge onto the subsequent blade, generating noise and potential structural issues. Finally, span-wise correlation close to the trailing edge can be an indication of acoustic sources[14].

In order to study the contribution of coherence at different frequencies in the wake, the following definition is taken for the two points magnitude-square coherence γ^2:

$$\gamma^2 = \frac{|\Phi_{v_1,v_2}|^2}{\Phi_{v_1,v_1}.\Phi_{v_2,v_2}}, \tag{3.4}$$

where Φ_{v_1,v_2} is the cross-power spectral density between two time series v_1 and v_2.

Fig. 3.9 shows vertical traverses of the two-point coherence between trough and mid-point, and trough and peak, at three downstream positions. Therefore, for each position a coherence map displays the value of coherence at each frequencies for a given probes separation. Fig. 3.9a shows that in the wake ($-0.2 < y/c < 0$) there is no coherence between trough and mid-point ($W/4$ separation) except around $St = 0.19$ which corresponds to the shedding previously observed. It is also clear that the lower part of the wake exhibits more coherence at this value than the upper part. Going further downstream, figs. 3.9c & 3.9e, the coherence in the wake decreases and becomes more symmetrical. Figs. 3.9b, 3.9d & 3.9f on the other hand show little variation when moving downstream with the trough-peak separation, although one notices

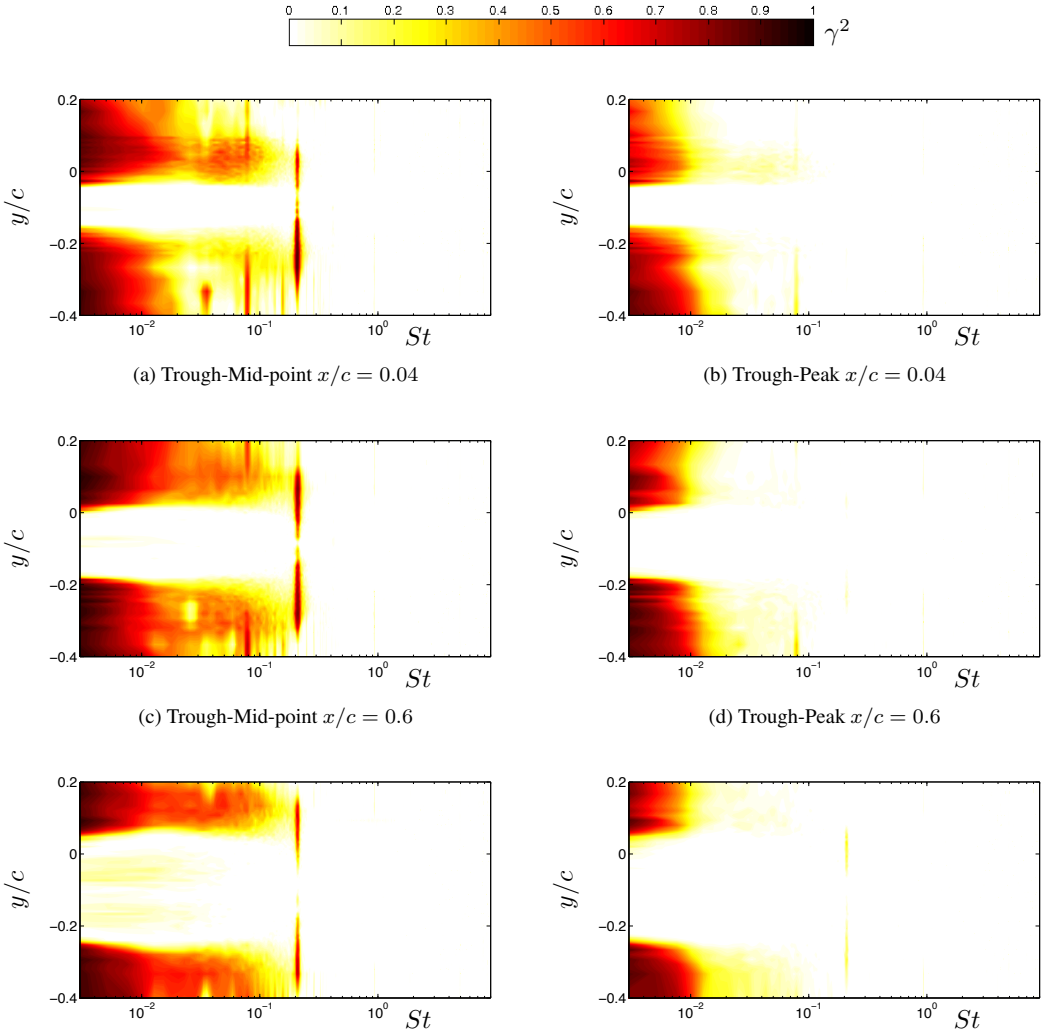
the appearance of very slight coherence between trough and peak at St_{sh} when going downstream. This corresponds to the span-wise spreading of shedding when the wake develops, but the value reached at $x/c = 2$ is much lower between trough and peak than between trough and mid-point. This is in fact in line with the comment made on the spectra, with shedding tending to disappear before it could be uniformly spread over the full TE wavelength, as illustrated in fig.3.6c.

One notices in fig. 3.9e that coherence between trough and mid-point appears in the wake over a broad range of low frequencies, up to $St = 0.03$. Although it could be due to rib structures developing in the wake, it can not be asserted for certain.

To focus on the downstream evolution of the shedding-associated correlation, fig. 3.10a shows the downstream evolution of vertical traverses of γ^2 at St_{sh} between trough and mid-point. Firstly, the strong asymmetry observed between the upper and lower part of the wake at $x/c = 0.04$ has diminished by $x/c = 0.4$ while the maximum values remain close to $\gamma^2 = 0.9$. In a second phase, the correlation slowly diminishes downstream until positions *circa* $x/c = 2$, which correspond to the point where the shedding intensity stops being discernible from the spectra, as pictured in fig.3.6c. The maximum values then decrease more significantly while going further downstream.

The effect of wavelength on γ^2 at St_{sh} is illustrated in fig.3.10b, with vertical traverses for $S20W84B$, $S20W40B$ and $S20W00B$ (whose probes' positions are based on the former TE). A shaded box shows the extent of the wake based on fig. 3.1b. The straight blunt case exhibits high values of γ^2 over a large y-extent, which denotes coherence that is more persistent outside of the wake. Both sinusoidal cases have a shorter y-extent of high γ^2 values, but the maximum is higher than for the straight; 0.85 to 0.9 for $S20W84B$. One should keep in mind, though, that due to the smaller wavelength of $S20W40B$, the probes are closer than in the case of $S20W84B$ and $S20W00B$ since they match the trough and mid-point positions. This shorter separation ($W/4$) could explain the higher maximum value observed for $S20W40B$. Compared to a straight blunt TE, the sinusoidal cut-in TEs reduce coherence in the wake close to the trailing edge. A marginally higher maximal value is observed in the traverse, but this corresponds to a less energetic part of the wake according to fig. 3.4b; and the total y-extent over which coherence is measured is reduced for the sinusoidal TEs.

To look at smaller scale correlations, a span-wise traverse is performed with a reference point on the centreline behind a trough and a second point traversed away in the span-wise direction. Fig. 3.11 a, b & c show the maps of γ^2 measured at $x/c = 0.04$ and in the middle of the wake (as illustrated in fig. 3.1b), which is at the height of the trailing edge tip, for $S20W84B$, $S20W40B$ and $S20W00B$. Therefore, each



(a) Trough-Mid-point $x/c = 0.04$

(b) Trough-Peak $x/c = 0.04$

(c) Trough-Mid-point $x/c = 0.6$

(d) Trough-Peak $x/c = 0.6$

(e) Trough-Mid-point $x/c = 2$

(f) Trough-Peak $x/c = 2$

Figure 3.9: γ^2 map between Trough and Mid-point, and Trough and Peak, behind $S20W84B$ at given downstream locations

map displays the coherence for all separations and all frequencies, at a given height, which differs slightly from the previously presented coherence maps. Fig. 3.11d shows the span-wise evolution of γ^2 averaged around the shedding frequency - with a method similar to eq. (3.1) -, defined as:

$$< \gamma^2 >_{sh} = \frac{1}{\Delta St \, . St_{sh}} . \int_{St_{sh}(1-\Delta St/2)}^{St_{sh}(1+\Delta St/2)} \gamma^2 \, dSt. \tag{3.5}$$

Fig. 3.11c shows a band of correlation at the shedding frequency behind $S20W00B$, and a strong harmonic. Both sinusoidal cases show a clear reduction of the harmonic bands. It is however less straightforward to compare the main shedding band of coherence. Fig. 3.11d shows that despite locally having very similar or even higher values, the sinusoidal cases have an overall reduction of this band of coherence and that in terms of physical extent (not normalised by W), $S20W40B$ has the strongest reduction.

However, both sinusoidal TEs have a higher correlation in the trough (top left corner of the γ^2 plots in fig. 3.11) at low frequency compared to $S20W00B$. Given the span-wise extent over which this is noticeable, a logical explanation is the span-wise flow, outcome of the cut-in approach observed in fig. 3.3. Having a higher mixing in the near wake to reduce shedding thus comes at the price of an increased coherence at low frequency. This effect is reduced with the shorter wavelength, which has a lower maximal value and a smaller physical extent (W being smaller) of coherence.

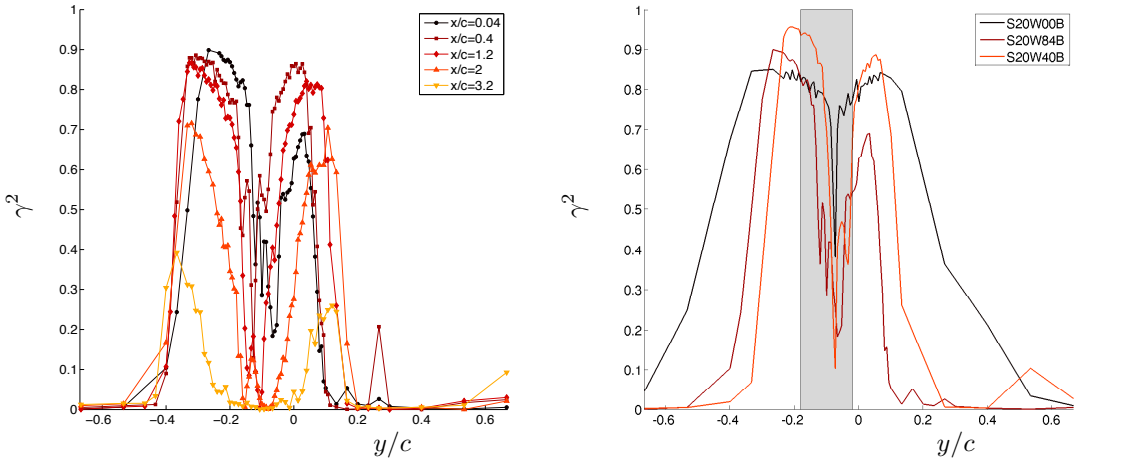
Compared to a straight blunt TE, the sinusoidal cut-in TEs thus appear to reduce span-wise coherence in the wake close to the trailing edge, in both vertical and span-wise extents.

3.4 Discussion on shedding energy span-wise oscillations

The shedding energy plotted in fig. 3.8 exhibits span-wise oscillations for both $S20W40B$ and $S20W84B$ at $x/c = 0.04$. The wavelength of the oscillations is $8\,$mm while $S20W40B$ and $S20W84B$ have wavelengths of $40\,$mm and $84\,$mm respectively. Fig. 3.12 shows the span-wise traverses of shedding-associated energy at $x/c = 0.04$ for $S20W00B$, $S20W40B$ and $S20W84B$. The aforementioned oscillations are also observed in the case of the straight blunt trailing edge: $S20W00B$.

Furthemore, these oscillations have not been observed in that wind tunnel in the study of turbulent boundary layers by Rodriguez-Lopez *et al.* [58]. It is therefore attributed to an imperfection of the apparatus that could have caused a slight inhomogeneity in the upstream boundary layer.

Although unfortunate for the results plotted in fig. 3.8, one can make two observations. Firstly, fig. 3.8



(a) Downstream evolution behind $S20W84B$

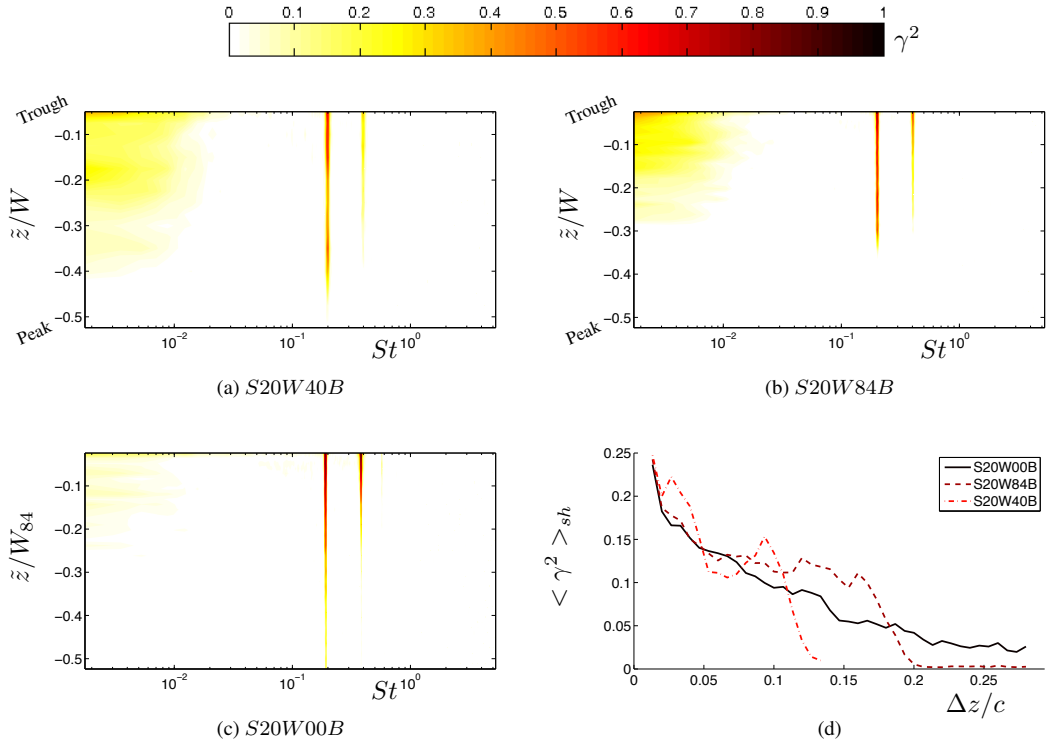
(b) Comparison between blunt cases at $x/c = 0.04$. Shaded box shows the extent of the wake based on fig. 3.1b.

Figure 3.10: Vertical traverses of $\gamma^2(St_{sh})$ between two span-wise locations: trough and mid-point.

(a) and (b) show that these oscillations do not appear further downstream, which indicates they could be levelled off in the trailing edge's wake. Secondly, fig. 3.12 shows that the serrations exhibit weaker oscillations than the straight blunt case, with the biggest difference being observed with $S20W40B$. In this case, the serrations have therefore mitigated incoming disturbances; and this effect would benefit from further study to assess whether or not it could be observed for other types of incoming perturbations. That topic is further developed in chapter 5.

3.5 Cell structures in the wake

Because of the cut-in approach, the exhibited bluntness varies along the span-wise direction, from maximum bluntness at the trough to sharpness at the peak. However, the shedding signal measured in the wake has a single fundamental frequency along the span, which indicates that the shedding is locked into a cell-like mechanism across the trailing edge pattern, instead of a smoothly evolving shedding mechanism. This explains the choice of the maximum bluntness at the trough in the definition of St, rather than the local bluntness. Vortex shedding had previously been observed to be locked into cell structures with other types

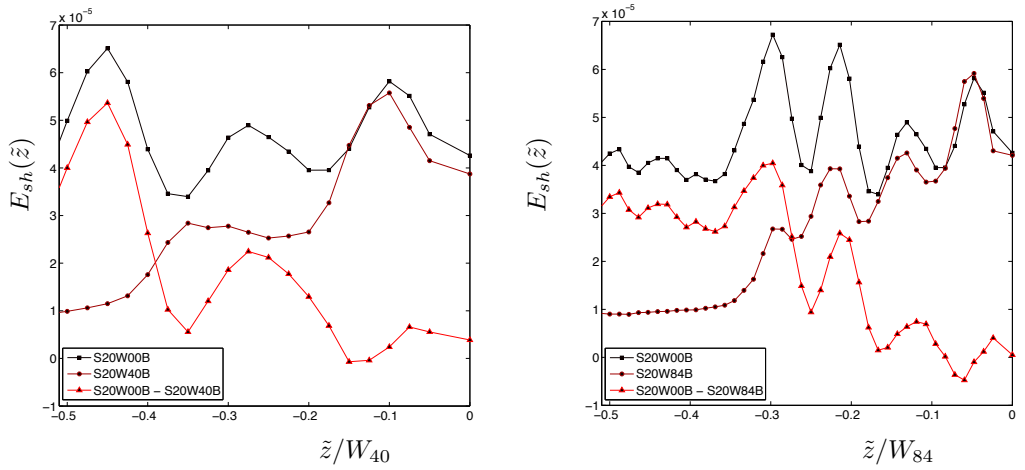


(a) $S20W40B$ (b) $S20W84B$

(c) $S20W00B$ (d)

Figure 3.11: Span-wise γ^2 map at $x/c = 0.04$ behind three blunt cases (a)-(c). Span-wise evolution of γ^2 averaged around its shedding value (d). The reference probe is fixed at the trough ($\tilde{z}/W = 0$) while the second probe is traversed towards the peak ($\tilde{z}/W = -0.5$).

of geometries, such as reported by Tombazis and Bearman [69]. The authors studied the case of a thick plate at zero incidence with a sinusoidal trailing edge of constant bluntness and observed regions (cells) shedding at different frequencies with a spatial arrangement that was observed to alternate in time. Hence a single measurement point could capture different shedding frequencies over time, while in the present case, only one fundamental shedding frequency is measured across the cell. Naturally, the two cases vary on key aspects such as the incidence, the varying bluntness and the curvature of the wing surface, which may explain the observation of different types of shedding cells.



(a) $S20W40B$ (b) $S20W84B$

Figure 3.12: Span-wise traverses of shedding-associated energy at $x/c = 0.04$ and comparison with $S20W00B$.

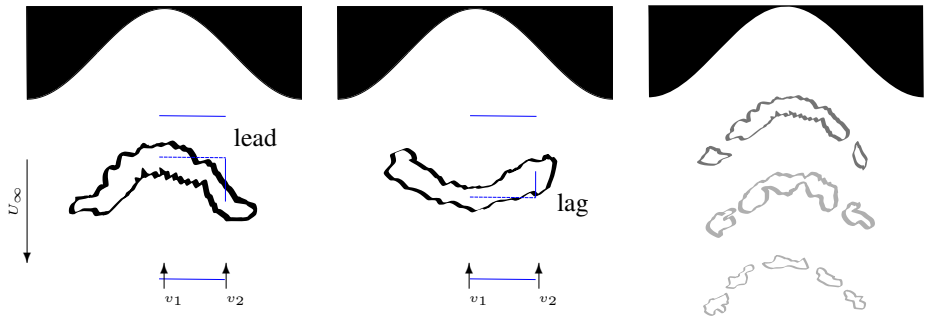
3.5.1 Dephasing

Although the previous observations indicate the presence of cell structures, so far there is no information as to how they develop downstream: either as straight lines or in more complex bent arches. The cross power spectral density provides information on the phase of coherent span-wise structures in the wake. Indeed, it may be written as:

$$\Phi_{v_1,v_2} = |\Phi_{v_1,v_2}|.e^{i\phi_{v_1,v_2}}, \tag{3.6}$$

and corresponds to the Fourier transform of the cross-correlation between the two signals v_1 and v_2. The phase ϕ_{v_1,v_2} thus gives an indication of how much lag there is between the two signals, and will henceforth be referred to as de-phasing. ϕ_{v_1,v_2} is a function of f and of the local convection velocity, since a strong variation of the latter between the measurement points could modulate the lag/lead measured. The value of ϕ_{v_1,v_2} at the shedding frequency, denoted ϕ_{sh}, is defined by averaging across a small range of frequencies, in an approach similar to eq. 3.5. Due to its definition, $\Phi_{v_1,v_2} < 0$ corresponds to v_2 having a lead on v_1. Fig. 3.13a displays a simplified case of a vortical structure shed from the trailing edge shaped as an arch. In the type 1 configuration, v_2 has an increasing lead on v_1 when being traversed away from it. On the other hand, if the arch is inverted, i.e. type 2, v_2 then has a lag compared to v_1. The absence of de-phasing would correspond to a straight vortex, while a chevron-shape one would exhibit a linear progression of

de-phasing when moving along the span-wise direction. Fig. 3.13c illustrates a weaker version of the arch shape structure, and how it might break down with streamwise distance.



(a) type 1 (b) type 2 (c) type 3

Figure 3.13: Sketch of three possible vortex shedding structures behind a serration.

To focus on the values of de-phasing corresponding to significant coherence, Γ_{sh} is introduced as follows:

$$\Gamma_{sh} = \gamma_{sh}^2 \cdot \phi_{sh}. \tag{3.7}$$

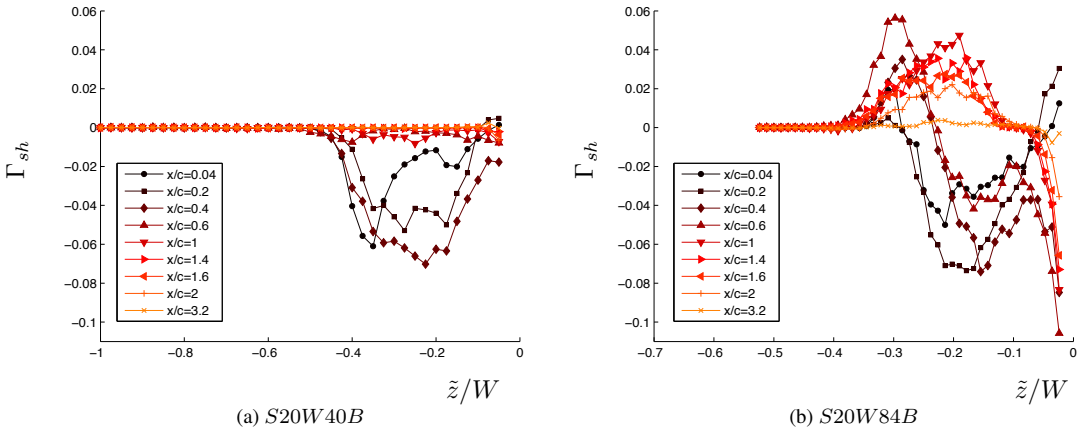
It must be stated that weighting by γ_{sh}^2 does not affect the evolution of ϕ_{sh} discussed hereafter but filters out fluctuations of de-phasing where coherence is negligible.

Fig. 3.14 shows the span-wise and downstream evolution of Γ_{sh} between a reference point (v_1) downstream of the trough and a point traversed in the span-wise direction (v_2) (both at the same x/c), downstream of $S20W40B$, and $S20W84B$.

For $S20W40B$, fig. 3.14a shows a clear spike of de-phasing values for several downstream positions, and no significant de-phasing for $z/W < -0.5$ for any location. When moving downstream, the de-phasing initially decreases with negative values, indicating that the mid-point/peak parts of the wake have a lead time over the trough area, which increases from $\tilde{z}/W = 0$ to around $\tilde{z}/W = -0.3$. This shows that the coherent structures shed by the trailing edge initially have a curved shape. For $\tilde{z}/W < -0.4$, Γ_{sh} quickly drops to zero as both coherence and de-phasing disappear. This corresponds to the edge of the vortex structure. These observations thus correspond to the idealised vortex structure of type 1 as illustrated in fig. 3.13a.

For $S20W84B$, fig. 3.14b shows that the first downstream positions exhibit a similar trend as for

$S20W40B$, with de-phasing initially forming a spike around $\tilde{z}/W = -0.2$. The main difference from the shorter wavelength is the inversion of the de-phasing sign when moving downstream, with positive values first appearing around $\tilde{z}/W = -0.3$ before becoming more widely spread. This means that when moving downstream, the mid-point area of the wake, which exhibited a lead over the trough area at the shedding frequency, starts to have a lag. The shape of the coherent structure would thus be inverted, corresponding to the type 2 structure in fig. 3.13b. This feature would be a logical outcome of the stronger velocity deficit observed at the peaks than at the trough, previously discussed in section 3.1. Another possible explanation, that could add to the previous, is a phenomena similar to the axis switching reported by Zaman [74] and Ramesh *et al.* [56], where the bent vortex would induce velocity fluctuations tending to re-straighten it and eventually invert its curvature. Given that vortex shedding was previous observed to be stronger for $S20W84B$ than $S20W40B$, it is logical to expect this phenomena to appear for the former.



(a) $S20W40B$ (b) $S20W84B$

Figure 3.14: Span-wise and downstream evolution of weighted de-phasing, Γ_{sh}, with reference point fixed at the trough ($z/W = 0$).

3.5.2 Modal decomposition

Up to now, the observation of the locking of vortex shedding into cells has been done by analysing two-probe hot wire data. To complement this study and generate a better understanding of the spatial structure of such cells, a PIV experiment was conducted, as detailed in section 2.2.4. Modal decomposition can be

used to extract spatial structures (modes) that are significant from the data. The term significant is based either on an estimation of the average of the energy content over all of the realisations, or on the dynamical role of each mode in a low order representation of the data.

POD modes

The first decomposition presented hereafter is the Proper Orthogonal Decomposition (POD), which has been extensively applied to fluid mechanics data in the past decades [11]. It takes each of the time steps as a realisation, without consideration for the time separation between them, and proceeds to extract modes based on their cumulated energy over the realisations.

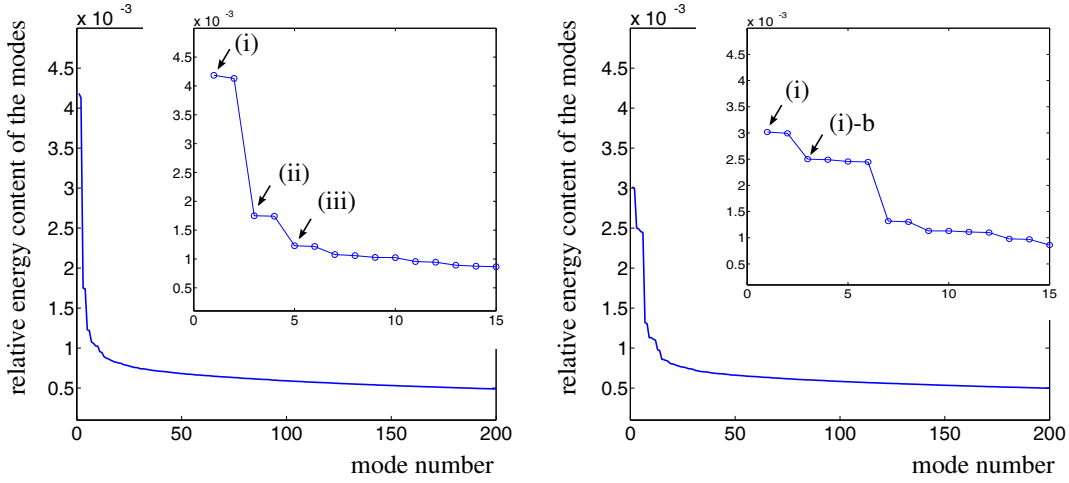
In our case, the PIV data gives, at each time step, a velocity field spanning the field of view, say $u(\mathbf{x}, t)$. The POD thus gives the basis to re-write u, as explained by Berkooz *et al.* [11]:

$$u(\mathbf{x}, t) = \sum_i a_i(t).\psi_i^{POD}(\mathbf{x}), \tag{3.8}$$

with a_i being the time coefficient of the associate spatial mode ψ_i^{POD}.

Fig. 3.15 shows the energy associated with each mode, normalised by the total energy. The real representation of the modes gives pairs, coming from the complex modes. The numbers (i)-(iii) identify the modes plotted in fig. 3.16 & 3.17. It is clear from fig. 3.15 that $S20W84B$ has one dominant mode and a secondary one, mildly distinct from the background. On the other hand, $S20W40B$ has three pairs of dominant modes. This is due to the fact that for this shorter wavelength, the field of view is not restricted to only one trough, and the same physical phenomena is observed for the two neighbouring troughs as well. The fact that this is captured in different modes highlights the independence of consecutive cells, and is discussed further in section 3.5.3.

Fig. 3.16 shows the modes (i), (ii) and (iii) for $S20W84B$. The re-circulation region immediately downstream of the blunt trough is not visible as the field of view is situated slightly under the wing (cf section 2.2.4). From mode (i), one notices the arched shapes predicted from the hot-wire data. The symmetry of the stream-wise component structure is expected, since the vortex shedding will alternately increase and decrease the stream-wise velocity. The anti-symmetry of the span-wise component can be explained by the bending of the vortices: if they were straight and contained only span-wise vorticity, they would not induce span-wise velocity. It is thus the decomposition into stream-wise/span-wise components of the velocity fluctuations induced by the bent shed vortices that creates the anti-symmetric structures. The mode



(a) $S20W84B$ (b) $S20W40B$

Figure 3.15: POD energy for the two blunt sinusoidal cases.

(i) hence corresponds to the idealised arch-shaped vortex shedding.

Section 3.1 reported a span-wise component in the mean flow, from peak to trough in the lower part of the wake. Comparison of fig. 3.16 and fig. 3.3a reveals that the extent of the w structures in mode (i) are similar to that of the mean flow. This modal decomposition is made on the velocity fluctuations, after subtracting the mean, so it is not a visualisation of the same effect. However, the link between the two is not hard to make. The mean flow will tend to bend the vortices shed in the trough; and the velocity fluctuations induced by these vortices will thus have a bent pattern with the symmetry discussed previously.

Modes (ii) is antisymmetric for the stream-wise component, and therefore symmetric for the span-wise component. It appears noisier than mode (i) which is in line with its lower energy as shown in fig. 3.15. Mode (iii) is shown out of interest, although its energy is much lower than (i) or (ii) and similar to that of the rest of the modes, and therefore it is less significant from the POD point of view. It is symmetric, but the structures are not the arches previously observed, and it is part of the noise or background that contribute to de-structure the flow.

Due to the smaller separation of energy between modes for $S20W40B$, fig. 3.17 displays only modes (i) and (i)-b. Although the same symmetry as for $S20W84B$'s mode (i) is observed, the spatial structures

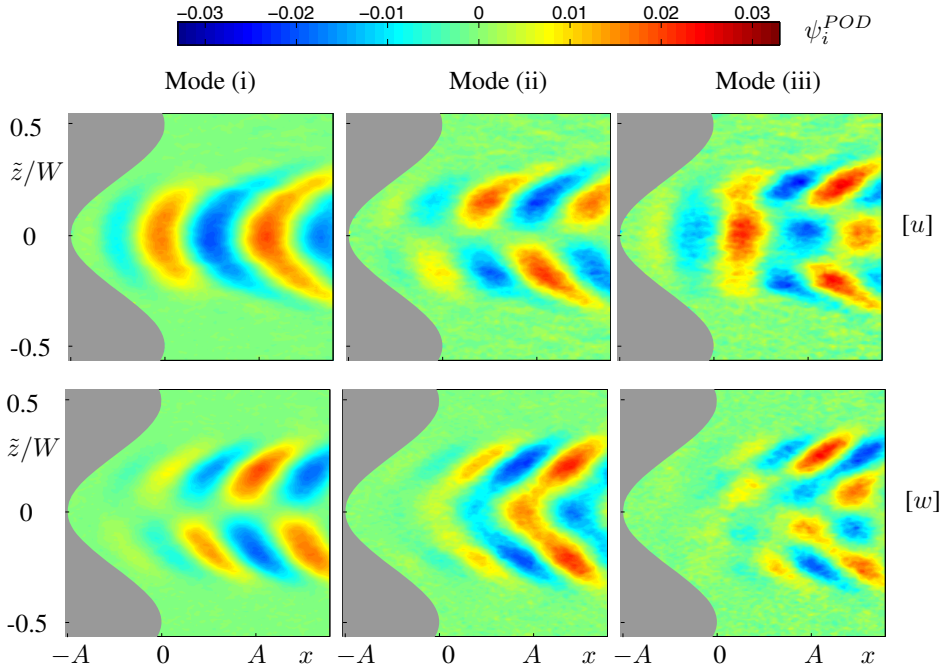


Figure 3.16: POD modes (i), (ii) and (iii) for $S20W84B$.

appear more compact. Fig. 3.17 clearly illustrates that mode (i)-b is the equivalent of mode (i) for the adjacent troughs, and as previously mentioned and further discussed in section 3.5.3, the fact that these are two distinct modes shows the independence of adjacent cells.

Fig. 3.18 shows the PSD of the coefficients a_i as defined in eq. 3.8 for the main modes of $S20W84B$ and $S20W40B$. For both trailing edges, the spectra of mode (i) are very similar, with a well defined peak at the vortex shedding frequency (about 600 Hz). Displayed for $S20W84B$, modes (ii) and (iii) show a reduction of the main peak, and the appearance of a secondary peak at a lower frequency. Although the main mode is clearly attributed to vortex shedding, it is not straightforward to link spatial structure to frequencies with the subsequent modes. POD thus gives a good insight into the spatial structure, but may miss modes that would be dynamically relevant even if not predominant in terms of POD energy.

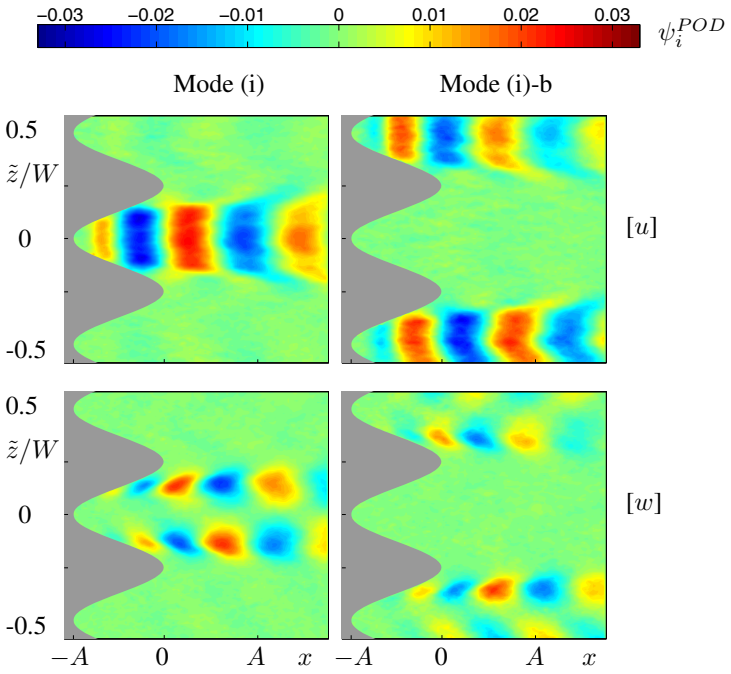
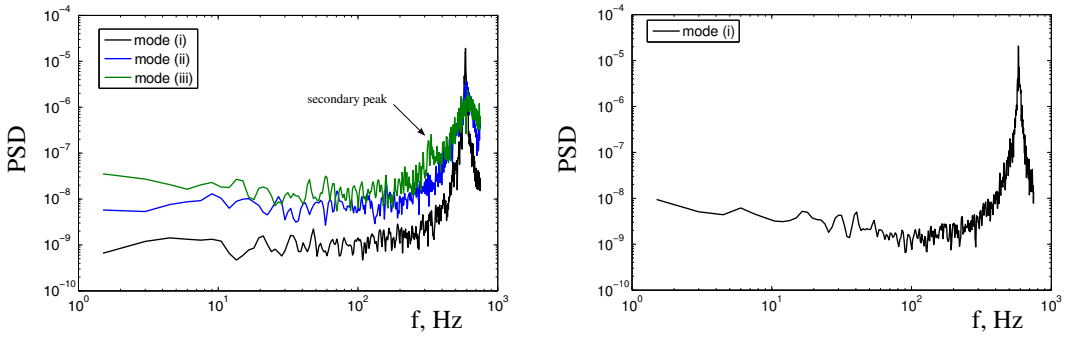


Figure 3.17: POD modes (i) and (i)-b for $S20W40B$.



(a) $S20W84B$ (b) $S20W40B$

Figure 3.18: POD coefficients' PSD

OMD modes

While studying the cell structures, it is of particular interest to attribute each mode to a specific frequency, in order to isolate the modes linked to the vortex shedding. For that reason, a modal decomposition approach that takes advantage of time-resolved data to link the modes to their frequencies can be adopted. In addition, dynamical study of the time-resolved data set enables us to highlight flow features that could be relevant to the dynamics of the vortex shedding structures.

The Optimal Mode Decomposition (OMD), as introduced by Wynn *et al.* [73], provides a low-rank linear approximation of a dynamical system comprising of snapshots

$$\{\psi_0, .., \psi_N\}, \quad \text{with} \quad \psi_i \in \mathbb{R}^k, \quad k \in \mathbb{N} \tag{3.9}$$

where a time-invariant linear evolution is assumed such that

$$\Psi_1 = \mathbf{A}\Psi_0, \quad \text{with} \quad \Psi_1 = [\psi_1, .., \psi_N] \text{ and } \Psi_0 = [\psi_0, .., \psi_{N-1}]. \tag{3.10}$$

OMD is similar to Dynamic Mode Decomposition (DMD) (Schmid [62] [63] and Jovanovic *et al.* [36]) in that it will approximate $\mathbf{A}$ by

$$\mathbf{A} \approx LML^T \quad \text{with} \quad L \in \mathbb{C}^{k,r} \text{ and } M \in \mathbb{C}^{r,r}, \quad r \in \mathbb{N} \text{ is the rank of } M. \tag{3.11}$$

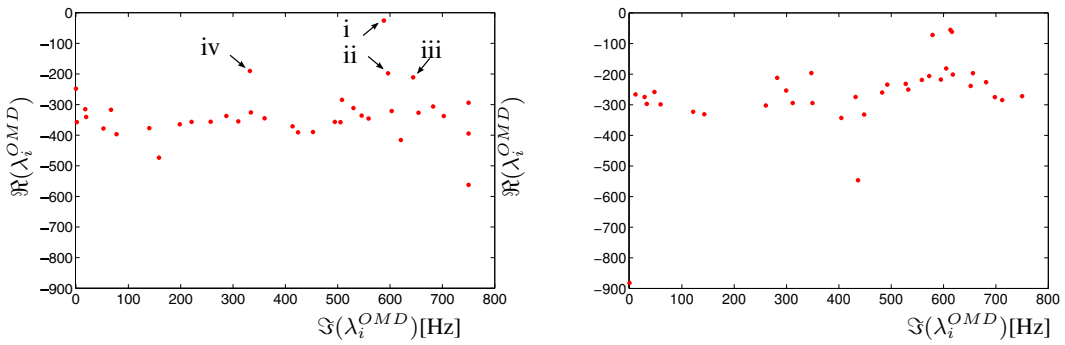
However, DMD takes the Proper Orthogonal Decomposition (POD) modes of Ψ_0 for L. In our case, it is not conceivable to use as many modes as snapshots, and reducing the number of the latter yields unsatisfactory results. A low-rank $r << N$ (i.e. a limited number of modes) is therefore imposed and we do not know *a priori* which basis is the most dynamically significant for L. The Optimal Mode Decomposition (OMD) is thus used to take advantage of its dual optimisation scheme. Indeed, the OMD process finds an optimal lower order representation of $\mathbf{A}$ by the following optimisation:

$$\min_{L,M} \left\| \Psi_1 - LML^T\Psi_0 \right\|^2 \quad \text{such that} \quad L \in \mathbb{C}^{k,r},\ LL^T = I_r \text{ and } M \in \mathbb{C}^{r,r}. \tag{3.12}$$

The matrix M is thus the low-order representation of the dynamic matrix $\mathbf{A}$. It satisfies an eigenvalue problem written as $Mz_i = \lambda_i(M)z_i$ which gives the OMD modes as Lz_i, associated to a decay rate of $\Re(\lambda_i^{OMD})$ and a frequency $\Im(\lambda_i^{OMD})$, such that $\lambda_i^{OMD} = \lambda_i(M)/\Delta t$. The pairs $\Re(\lambda_i^{OMD})$ and $\Im(\lambda_i^{OMD})$ form the OMD spectrum. In our case, r was chosen to be high enough to avoid the dependence of the main peaks' frequencies on the number of modes: a value of $r = 70$ was found to be satisfactory.

The reader is refered to Wynn *et al.* [73] for further details, and to Rodríguez-López *et al.* [58] and Baj *et al.* [8] for other studies applying OMD to PIV data, in strongly disturbed boundary layers and behind multiscale arrays of bars.

Fig. 3.19 shows the OMD spectra for $S20W84B$ and $S20W40B$. The modes being complex conjugate, only the positive half of the spectra is plotted. The numbers i-iv identify the modes being plotted in fig. 3.20. They are the least damped modes, and therefore the most dynamically relevant. It is clear from fig. 3.19a that $S20W84B$ exhibits two peak frequencies, one corresponding to the vortex shedding (i), at ~ 590 Hz ($S_t \simeq 0.19$) and a secondary one at ~ 340 Hz (iv). The modes (ii) and (iii) correspond to frequencies just above the one of (i) but their $\Re(\lambda_i^{OMD})$ is of the same level as iv. Fig. 3.19b shows that in the case of $S20W40B$, the main peak is not comprised of one mode, but three distinct ones. This corroborates the fact that successive serrations shed independently, as observed with the POD modes. Out of interest, the OMD procedure was also run with a very limited number of modes, and these main modes were still separated for consecutive troughs, reinforcing the previous comment.



(a) $S20W84B$ (b) $S20W40B$

Figure 3.19: OMD spectra

Fig. 3.20 shows the stream-wise and span-wise velocity components of modes (i)-(iv) for $S20W84B$. Mode (i) is nearly identical to the POD's mode (i) which means that both methods pick-up the same dominant flow features associated with the vortex shedding. Modes(ii) and (iii) are antisymmetric for the stream-wise component, and therefore symmetric for the span-wise component. They are well structured for $S20W84B$, although not as neat as mode (i). They both look similar to the POD's mode (ii), but exhibit

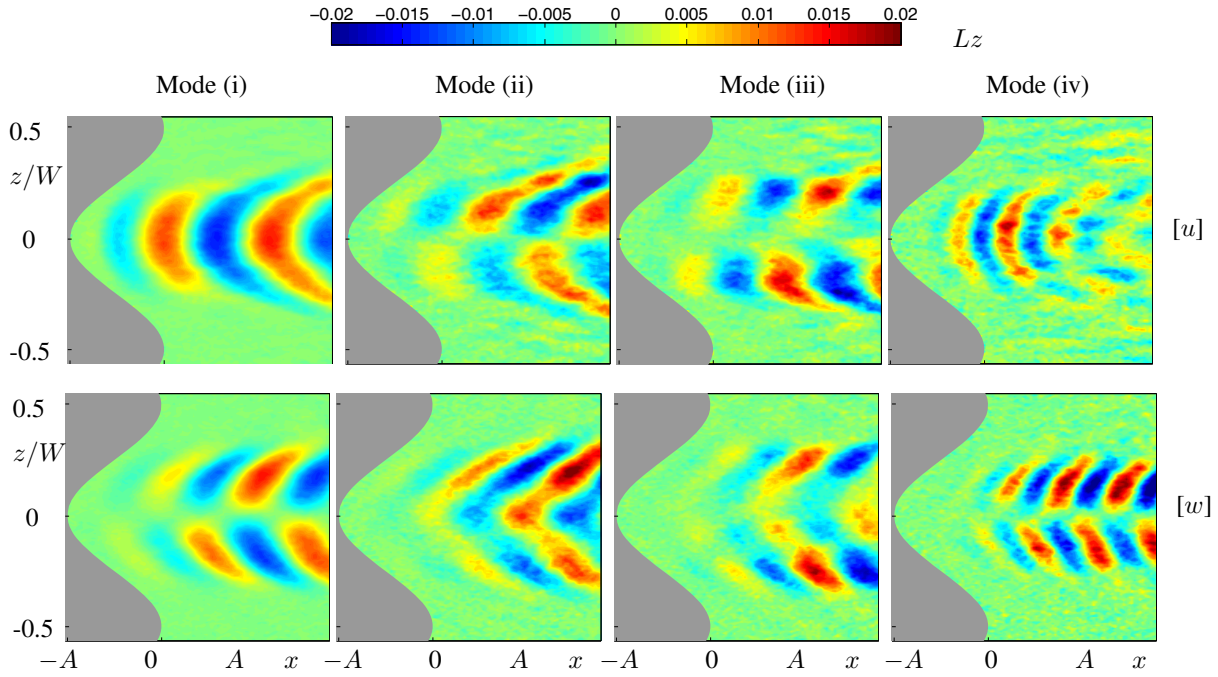


Figure 3.20: OMD modes (i)-(iv) for $S20W84B$.

variations in their spatial structure. Having two distinct frequencies associated with each of them also shows a more broadband characteristic of these de-structuring modes.

Mode (iv) is similar to mode (i), however, the wavelength of the structure is smaller, as well as the associated frequency in the spectra, and there is no harmonic relation between the two. It is most likely a mode adding rippling and breaking down the spatial organisation of mode (i), to tend towards a weaker structure as depicted in fig. 3.13c. This mode is different from the POD's mode (iii), but appears at the frequency of the secondary peak observed in fig. 3.18. The ability to separate frequencies between modes thus allows us to pick up a mode that could be dynamically relevant but previously missed out.

Fig. 3.21 shows mode (i) for $S20W40B$. The symmetric/anti-symmetric structures are also found. As noted before, the OMD spectra for this case showed three modes for the main peak. This indeed corresponds to the three consecutive troughs visible in the field of view. Only the ones relative to the central trough are plotted here.

Overall, both approaches are complementary and it appears that the cell structures described by the

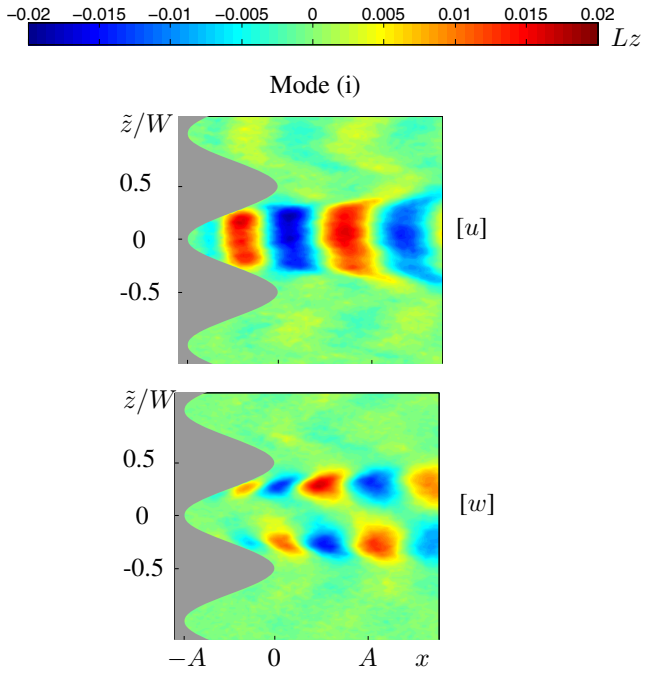


Figure 3.21: OMD modes (i) for $S20W40B$.

hot-wire data analysis are qualitatively found with the first modes of the OMD decomposition. However, to link the two sets of data more quantitatively, the main OMD modes can be used to reconstruct a set of velocity fields. The i^{th} reconstructed snapshot is taken as the sum of the OMD modes weighted by the projection of the original i^{th} snapshot onto said modes. The modes being complex, the real part of the sum is taken. The set of reconstructed snapshots thus gives, for each position of the field of view, a time series extracted from the original data.

Fig. 3.22 shows the span-wise evolution of de-phasing ϕ_{sh} at $x/c = 0.04$ downstream of $S20W84B$ obtained from hot-wire data, and OMD reconstructions with modes (i), (ii) and (iii), and with modes (i), (ii), (iii) and (iv). The time series obtained from this method are shorter than those obtained with the hot-wires, and the periodogram methods can only be used with a limited number of windows. The spectral analysis of reconstructed data thus yields higher noise than that of the hot-wire data, and the comparison is hence made using the de-phasing without weighting by the coherence. Given that for $\tilde{z}/W < -0.4$, the data are noisier and coherence drops down, this range is not included in the plot. Using the four main modes actually

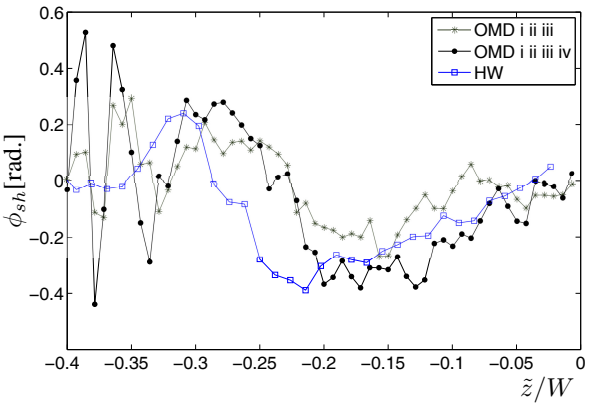


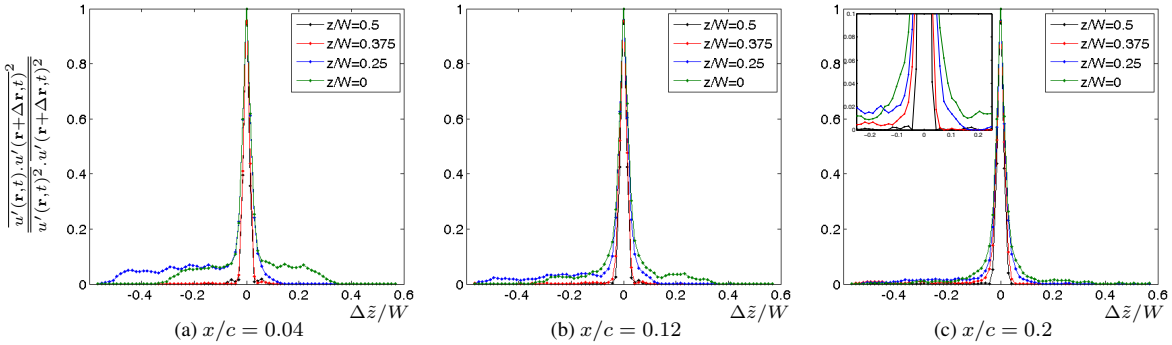
Figure 3.22: Comparison between de-phasing obtained by HW and OMD reconstructions with modes (i) (ii) (iii), and (i) (ii) (iii) (iv).

gives a better matching of the hot-wire data, despite the fact that mode (iv) is actually not associated to the shedding frequency. This demonstrates its importance in the structure of the shedding cells. From $\tilde{z}/W = 0$ to -0.35, there is a reasonably good match of the hot-wire data with four modes reconstruction, noticing a decrease of ϕ_{sh} until around $\tilde{z}/W = -0.2$, and the extrema values are the same. After $\tilde{z}/W = -0.35$, the OMD data become more noisy, but coherence is very low in that area, so it is of lesser significance. Since this mode (iv) was not observed with POD, it also highlights the use of OMD to pick-up dynamically relevant modes. Overall, this comparison shows that the approach proposed for the study of de-phasing not only shows qualitative information on the shape of the modes, but also corresponds to a quantitative match of the cell structures.

3.5.3 Independence of the cells

The observation of distinct modes for the shed structures of adjacent serrations hints at the independence of the shedding mechanism for consecutive cells. As previously mentioned, this was observed for both POD and OMD, particularly illustrated in fig. 3.17.

In fact, the study of spanwise coherence corroborates this interpretation. Fig. 3.11a shows that coherence with reference to the trough is contained within $|\tilde{z}/W| < 0.4$, and although the figure is truncated at the peak to match the display of the longer wavelength, no coherence is found when moving further away



(a) $x/c = 0.04$ (b) $x/c = 0.12$ (c) $x/c = 0.2$

Figure 3.23: Span-wise traverses of correlation coefficient with references at four span-wise locations, performed at three downstream locations for $S20W40B$.

towards the adjacent trough.

Using the time-resolved PIV data, it is possible to obtain correlation traverses with other locations of the reference. Fig. 3.23 shows spanwise traverses of the correlation coefficient, defined as

$$\frac{\overline{u'(\mathbf{r},t).u'(\mathbf{r}+\Delta\mathbf{r},t)}^2}{\overline{u'(\mathbf{r},t)^2}.\overline{u'(\mathbf{r}+\Delta\mathbf{r},t)^2}} \tag{3.13}$$

between two time series u' taken at locations $\mathbf{r}$ and $\mathbf{r}+\Delta\mathbf{r}$. The traverses are performed at three downstream locations, with four spanwise positions of the reference for each. These positions match the trough ($\tilde{z}/W = 0$), mid-point ($\tilde{z}/W = 0.25$) and peak ($\tilde{z}/W = 0.5$), as well as an intermediary point between mid-point and peak ($\tilde{z}/W = 0.375$). At $x/c = 0.04$, the correlation centred at the trough is symmetric, as expected from the shape of the cell structures, and drops to zero before going downstream of the adjacent serrations. When using $\tilde{z}/W = 0.25$ as a reference, the correlation traverse becomes asymmetric, with non-zero values towards the negative separation, that is towards $\tilde{z}/W = 0$. Putting the reference close to the peak does not show any correlation apart from the main peak, due to the absence of shedding cell. Moving downstream, at $x/c = 0.12$, the overall values decay, but the same asymmetry is observed. However, when moving to $x/c = 0.2$, it is interesting to note that the traverse with reference at $\tilde{z}/W = 0.375$ starts exhibiting a similar, but weaker, asymmetry. Overall, this shows that the velocity fluctuations in the wake of the serrations are only correlated behind their own serration, and not with the part of the wake behind the adjacent one.

Thus, both the presence of distinct modes for adjacent cells and the absence of correlation behind

adjacent serrations show that the shedding mechanism is independent between neighbouring cells.

3.6 Discussion and concluding remarks

Experiments have been conducted on a NACA0012 wing at moderate angle of attack to study the impact of cut-in sinusoidal trailing edge modifications on the wake generated by a lifting body.

The cut-in approach for the trailing edges generates a flow from below the peaks towards the troughs. Such a flow pattern increases the velocity deficit behind the peaks while re-energising the wake behind the troughs. Therefore, span-wise inhomogeneity of the velocity deficit and wake width is observed and persists far downstream, particularly for the wake width.

Span-wise inhomogeneity is also observed in spectral analysis, where the shedding signature slowly spreads out, in the span-wise direction from the troughs. Downstream evolution of the shedding intensity shows that the shedding signature disappears from the spectra before span-wise homogeneity is reached. Furthermore, the shedding intensity strongly decreases with shorter wavelength of the sinusoidal patterns (within our cases of serration angles higher than 45 deg), with up to 57% reduction compared to the straight blunt case.

The span-wise coherence is in turn affected by the modified TE. Span-wise coherence is mostly seen at the shedding St and is greatly reduced by the sinusoidal patterns compared to the blunt straight one, which however comes at the price of an increase in low frequency coherence.

Vortex shedding is found to be locked into cell structures behind the cut-in serrations. The study of dephasing between the trough position and other span-wise locations shows that these cell structures are bent and can be reversed (for the large wavelength) by the span-wise inhomogeneity of the stream-wise velocity. Analysis of the PIV data by Optimal Mode Decomposition offers an insight into the spatio-temporal organisation of these structures. The bent shape is indeed clearly observed for modes corresponding to the vortex shedding frequency. The lack of coherence between adjacent cells and the existence of distinct modes for each of them shows that the shedding is independent between neighbouring serrations.

The shedding of coherent structures by the serrated trailing edge can be a source of noise and even drag in the blunt part of the troughs. Moreover, these structures once shed into the wake, could impinge onto a second blade or wing and in turn deteriorate the acoustic and/or aerodynamic performance of a blade array. For both reasons, it would be interesting to devise a way to break these cell structures down, and to reduce the low frequency coherence introduced by these cut-in serrations. This endeavour is the topic of chapter 4

Chapter 4

Effecting the coherence

The previous chapter has shown that the introduction of bluntness by the cut-in approach generates vortex shedding locked into a cell structure. Vortical structures shed into the wake can be problematic in the context of blades arrays or rotor/stator interaction. Moreover, close to the trailing edge, coherent vortical structures can be a source of base drag, or even noise depending on their alignment with the solid edge. This chapter looks into means of breaking down these coherent structures, while maintaining a serrated trailing edge without extension plate.

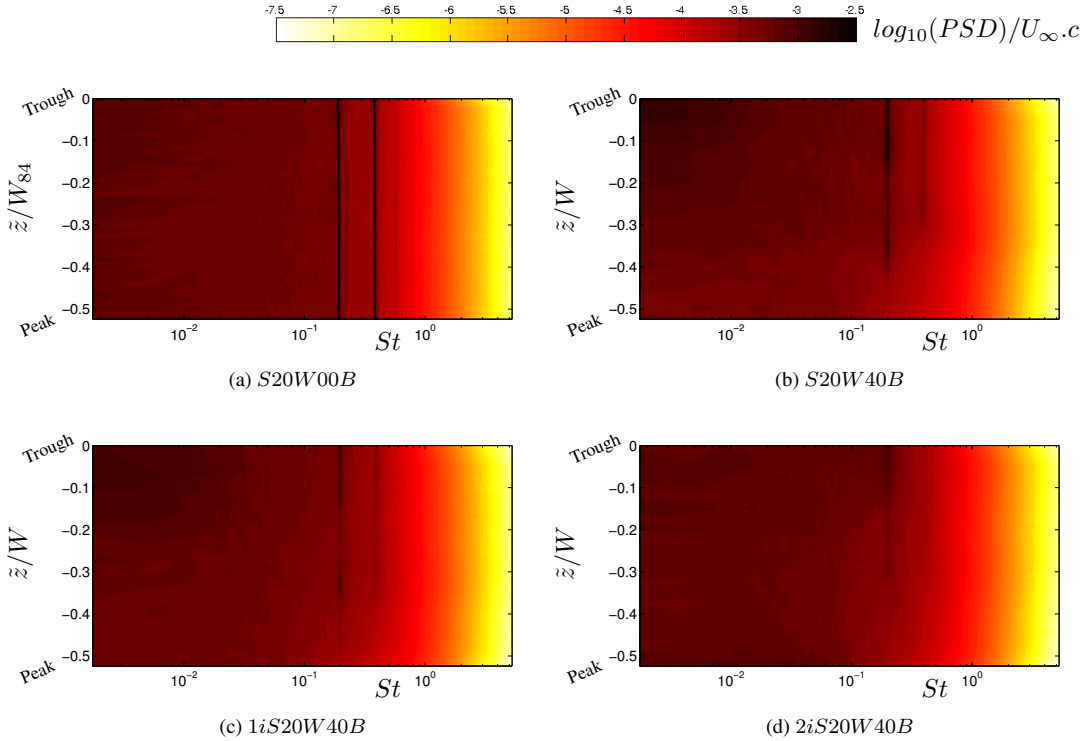
4.1 Multiscale TE

The first option chosen for this endeavour is the use of multiscale patterns. The reduction of vortex shedding intensity by the introduction of fractal shapes in other applications has been presented in section 1.2. Furthermore, the cell structure observed in chapter 3 is clearly shaped by the trailing edge patterns and the cross flow observed between the peaks and the troughs. Modifying such geometrics could thus disrupt the build-up of the cell structures and in turn reduce the coherence and vortex shedding intensity previously measured.

The trailing edge patterns used in this study are illustrated in section 2.1.1, they correspond to the iterative addition of a sinusoidal curve normally to the previous one. The goal is to locally reduce the wavelength while adding multiscale features.

4.1.1 PSD

The first step in assessing the impact of multiscale patterns on the cell structure is to check the intensity of the vortex shedding. Fig. 4.1 shows PSD maps of spanwise traverses behind $S20W00B$, $S20W40B$, $1iS20W40B$ and $2iS20W40B$. As observed in the previous chapter, $S20W00B$ exhibits almost no spanwise variation of its spectra, with a strong vortex shedding peak and two additional harmonics visible. $S20W40B$ on the other hand exhibits a strong spanwise variation of its spectra, resulting from the cell structures discussed in the previous chapter. Only the fundamental and the first harmonic of the vortex shedding are visible for this sinusoidal serration. For $1iS20W40B$ and even more for $2iS20W40B$, the shedding peak is milder than for $S20W40B$ with the harmonic hardly visible for the 2-iteration pattern. Since the intensity at the vortex shedding frequency appears to be the most affected, the study of its spanwise and downstream evolution should bring valuable information as to how these multiscale patterns affect the PSD in their wake and offer a first insight into their effect on the shedding cells.



(a) $S20W00B$

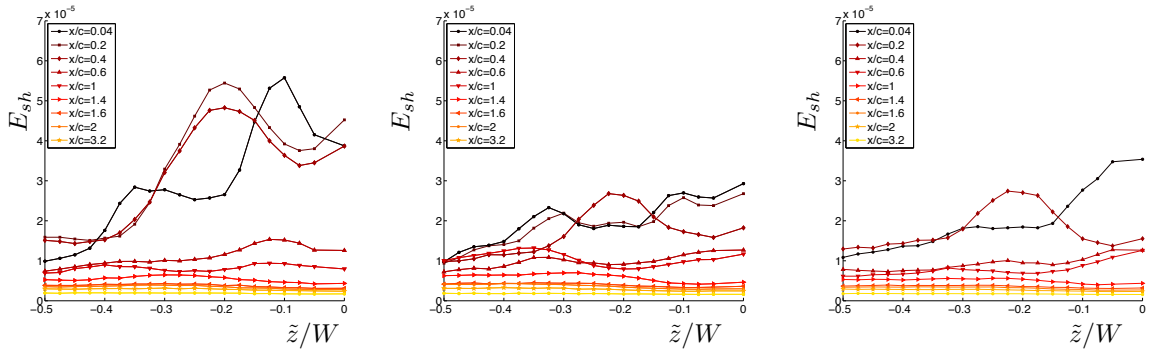
(b) $S20W40B$

(c) $1iS20W40B$

(d) $2iS20W40B$

Figure 4.1: PSD maps, $x/c = 0.04$ downstream of four tested trailing edges.

Fig. 4.2 shows the span-wise and downstream evolution of E_{sh} (as introduced in section 3.2) for a single tone pattern ($S20W40B$), and for one ($1iS20W40B$) and two ($2iS20W40B$) additional iterations. The multiscale patterns clearly show a lower energy in the shedding signature compared to the single tone pattern. Far downstream, for $x/c > 1.6$, the energy involved is not significant as no shedding spike is discernible in the spectra any more (cf. fig. 3.6), and the differences are minimal. Both multiscale TEs exhibit similar shedding intensity levels and the introduction of the second iteration does not seem to have a clear effect.



(a) $S20W40B$ (b) $1iS20W40B$ (c) $2iS20W40B$

Figure 4.2: Span-wise and downstream evolution of shedding associated energy, E_{sh}. N.B. Oscillations at $x/c = 0.04$ are discussed in section 3.4.

As discussed in section 3.4, oscillations at $x/c = 0.04$ are noticed in fig. 4.2. It is nonetheless clear that these oscillations are weakened by the multiscale patterns, particularly by $2iS20W40B$, for which they have almost disappeared. This would indicate the possible effect of the multiscale patterns on breaking down incoming perturbation which, although interesting, is not the primary focus of this chapter and is discussed further in chapter 5.

4.1.2 Coherence

Chapter 3 has shown a reduction of coherence at St_{sh} with the introduction of sinusoidal patterns, in comparison to a straight blunt trailing edge ($S20W00B$). However, as illustrated by fig. 3.11, such sinusoidal patterns introduce coherence over a broadband range of low frequencies, especially in the trough.

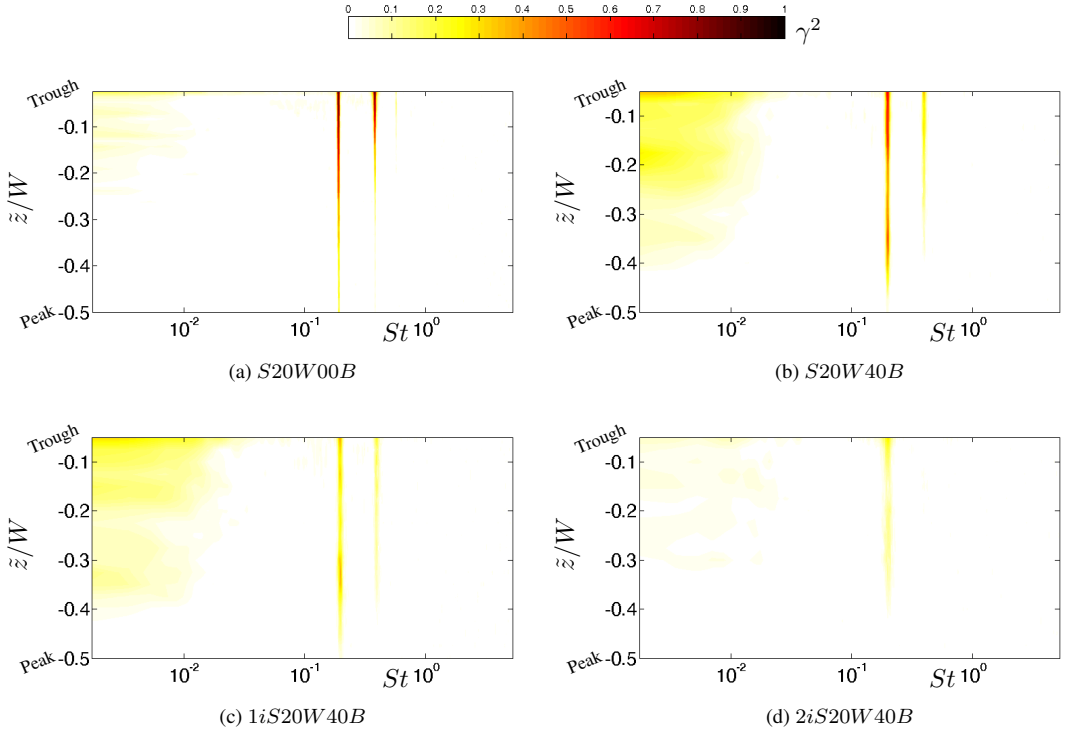
Fig. 4.3 shows that the use of multiscale patterns mitigates this effect. Indeed, when comparing the total low frequency content of coherence - obtained by integrating γ^2 over $-0.5 < \tilde{z}/W < 0$ and $St < 0.07$ - a reduction of 8% is achieved between $S20W40B$ and $1iS20W40B$, and 57% between $S20W40B$ and $2iS20W40B$. The corresponding PSD maps (cf fig. 3.7) show that the low frequency region of high coherence downstream of the trough corresponds to high values of energy; hence adverse effects such as acoustic noise emission would be non-negligible. Therefore, reduction of coherence in this region is of particular interest.

It is clear from fig. 4.3 that the introduction of multiscale patterns also reduces coherence at the vortex shedding frequency and its second harmonic. For ease of comparison, γ^2 can be directly plotted at St_{sh} with the definition given by eq. 3.5.

Fig. 4.4 shows the span-wise evolution of γ^2_{sh} at $x/c = 0.04$ behind the sinusoidal and multiscale trailing edges for both wavelengths. The values are plotted against $\tilde{z}/c$ to provide a comparison of the physical extent over which coherence is observed for the different TEs. As reported in chapter 3, the single tone serrations already reduce the extent over which coherence is measured compared to a straight blunt geometry, despite some locally higher values. All TEs with $W = 40\,\text{mm}$ show a significantly shorter extent than those with $W = 84\,\text{mm}$. This is expected given that chapter 3 has shown that vortex shedding was locked into cell structures downstream of the serrations, and that consecutive cells shed independently: the coherence should therefore be limited to the spatial extent of one cell. The introduction of multiscale geometry further reduces these values, the difference being the greatest between $S20W40B$ and $2iS20W40B$.

One can notice that for both $S20W40B$ and $1iS20W40B$, a local peak of coherence at St_{sh} is observed around $\tilde{z}/W = -0.35$ in fig. 4.3, as well as for both wavelengths in fig. 4.4 (note that z/c is used in the latter, with $\tilde{z}/W_{40} = -0.35 \sim \tilde{z}/c \simeq 0.09$). This feature is thought to be due to the cross-flow generated by the serrations themselves, discussed in section 3.1. Note that $2iS20W40B$ does not exhibit this peak and is the TE that reduces coherence the most, which is most likely due to the higher waviness of its pattern following the introduction of the second iteration.

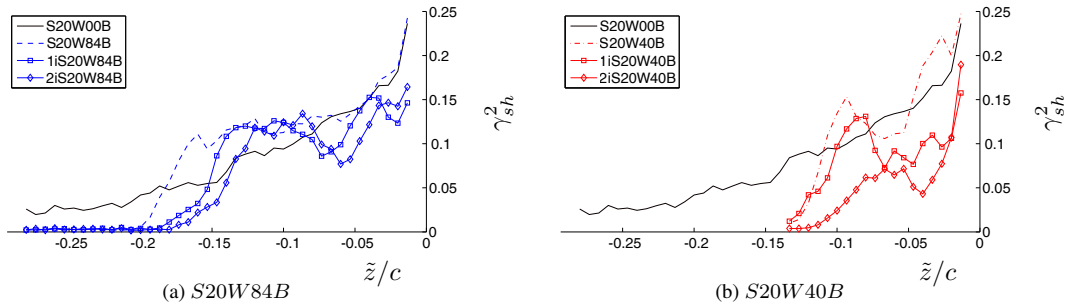
Fig. 4.5 shows the spanwise and downstream evolution of γ^2_{sh} behind $S20W40B$, $1iS20W40B$ and $2iS20W40B$. The $x/c = 0.04$ position was shown in fig. 4.4, and it is interesting to see that the reduction of coherence is not only seen very close to the trailing edge, but also further downstream. For intermediate positions such as $x/c = 0.4$ or $x/c = 0.6$, the reduction is not obvious between $S20W40B$ and $1iS20W40B$ but is rather clear between $S20W40B$ and $2iS20W40B$. The study of shedding energy had shown little difference between the two multiscale patterns, while the study of coherence shows that



(a) $S20W00B$ (b) $S20W40B$

(c) $1iS20W40B$ (d) $2iS20W40B$

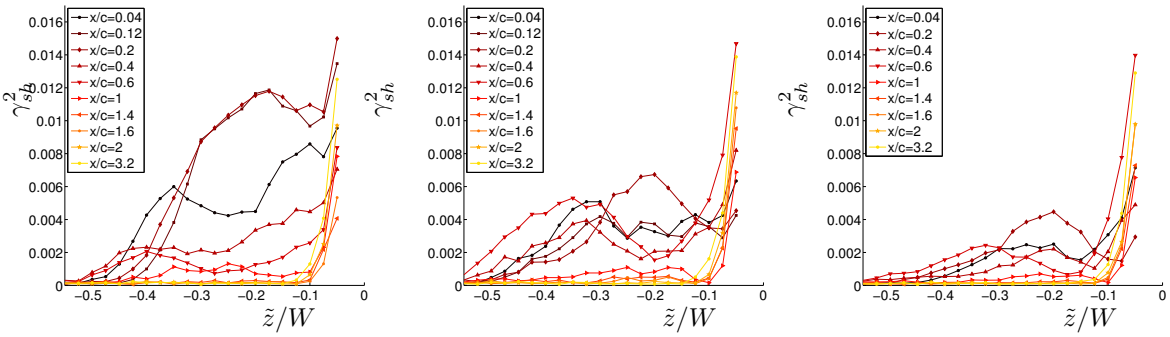
Figure 4.3: γ^2 maps, $x/c = 0.04$ downstream of four tested trailing edges.



(a) $S20W84B$ (b) $S20W40B$

Figure 4.4: γ^2_{sh}, $x/c = 0.04$ downstream of the trailing edges.

$2iS20W40B$ has the strongest reduction; overall, adding the second iteration has therefore the most significant impact on both energy and coherence of the shed structures. The downstream persistence of reduction



(a) $S20W40B$ (b) $1iS20W40B$ (c) $2iS20W40B$

Figure 4.5: Span-wise and downstream evolution of shedding associated coherence, γ^2_{sh}.

of coherence shows that the multiscale patterns actually reduce the coherence of the shed structure rather than just delaying their formation.

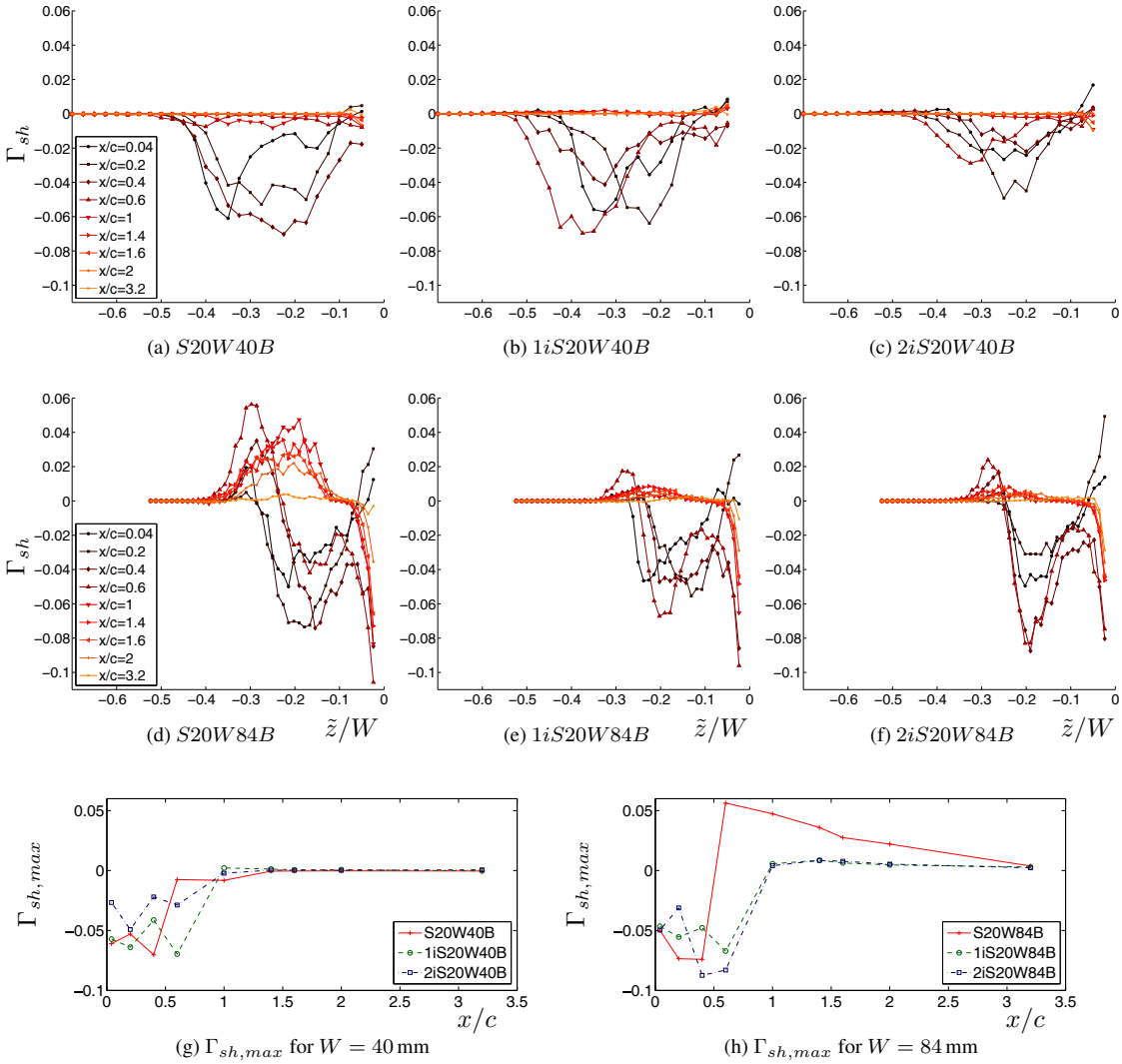
4.1.3 De-phasing

The definition of de-phasing and the rationale behind its use are given in section 3.5.1. Since the study of de-phasing gives an indication of the shape of the cell structures, it is natural to look into the effect of multiscale patterns on its spanwise and downstream evolution.

Fig. 4.6 shows the span-wise and downstream evolution of Γ_{sh} between a reference point downstream of the trough and a point traversed in the span-wise direction (both at the same x/c), downstream of $S20W40B$, $1iS20W40B$ and $2iS20W40B$, and $S20W84B$, $1iS20W84B$ and $2iS20W84B$. The value of Γ_{sh} that has the greatest absolute value for each downstream location is plotted in fig. 4.6g & 4.6h for all serration patterns.

Fig. 4.6b shows that, in the wake of $1iS20W40B$, Γ_{sh} reaches similar values as for $S20W40B$. The spanwise location of maximum de-phasing seems to vary more for $1iS20W40B$, but the wakes appear similar. On the other hand, the downstream evolution of $\Gamma_{sh,max}$ displays smaller values for $2iS20W40B$ (by a factor 2 in most cases) in fig. 4.6c.

As explained in section 3.5.1, the change of sign of the de-phasing downstream of $S20W84B$ indicates an inversion of the vortical structure.



(a) $S20W40B$ (b) $1iS20W40B$ (c) $2iS20W40B$

(d) $S20W84B$ (e) $1iS20W84B$ (f) $2iS20W84B$

(g) $\Gamma_{sh,max}$ for $W = 40\,\text{mm}$ (h) $\Gamma_{sh,max}$ for $W = 84\,\text{mm}$

Figure 4.6: Span-wise and downstream evolution of weighted de-phasing, Γ_{sh}, with reference point fixed at the trough ($\tilde{z}/W = 0$).

Fig. 4.6e & 4.6f show that for both multiscale geometries there is no significant extent of de-phasing sign inversion. This difference is also seen in fig. 4.6h where $\Gamma_{sh,max}$ has greater positive values for $S20W84B$ than for the multiscale TEs. This implies that the introduction of multiscale patterns weakens

the coherent structures before they are bent either by the flow or by a mechanism resembling axis switching as discussed in section 3.5.1. Both multiscale cases have weaker de-phasing than the single tone pattern in the near wake, but exhibit strong span-wise variation when going further downstream, before de-phasing disappears at around $x/c = 1$. The plots in fig. 4.6 also reveal that the effect of multiscale observed for $1iS20W84B$ (fig. 4.6e) and $2iS20W84B$ (fig. 4.6f) is lesser than for $1iS20W40B$ (fig. 4.6b) and $2iS20W40B$ (fig. 4.6c); and in turn this would explain why fig. 4.4 shows less reduction for the large wavelength than for the small one.

These results point towards the fact that multi-scale geometries weaken the cell structure of the vortex shedding, that was characteristic of single tone sinusoidal trailing edge cut-in serrations.

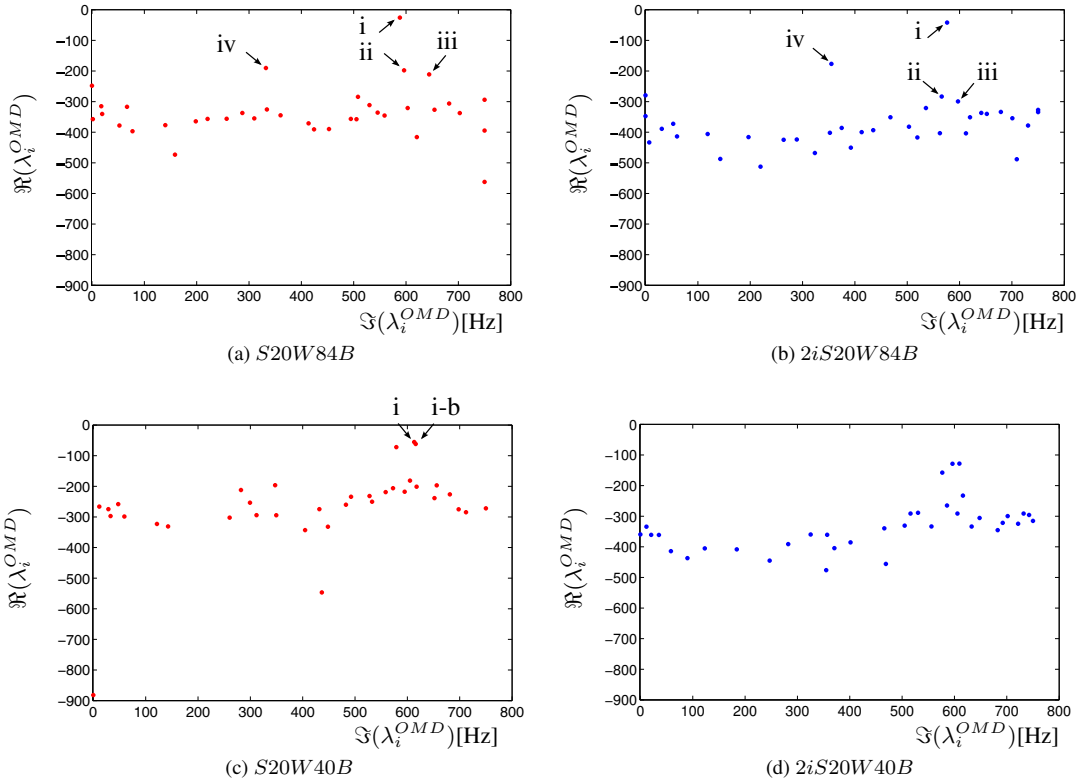
4.1.4 OMD modes

The Optimal Mode Decomposition process was explained in section 3.5.2 along with its application to the wake of the single tone sinusoidal trailing edges. This section presents the difference of the cells' spatio-temporal structures between single tone patterns and multiscale ones. Given the previous results, the focus is put on the 2-iteration patterns which reduce both shedding energy and coherence the most.

Fig. 4.7 shows the OMD spectra for $S20W84B$, $2iS20W84B$, $S20W40B$ and $2iS20W40B$. The modes being complex conjugate, only the positive half of the spectra is plotted. The numbers (i)-(iv) identify the modes being plotted in fig. 4.8. They are the least damped modes, and therefore the most dynamically relevant. It is clear from fig. 4.7a that $S20W84B$ exhibits two peak frequencies, one corresponding to the vortex shedding (i), at $\sim$ 590 Hz ($St \simeq 0.19$) and a secondary one at $\sim$ 340 Hz (iv). The modes (ii) and (iii) correspond to frequencies just above that of (i) but their $\Re(\lambda_i^{OMD})$ values are at similar level to (iv). Fig. 4.7b shows the OMD spectra for $2iS20W84B$. Although the frequencies differ slightly, two similar peaks are observed for modes (i) and (iv). However, it is clear that modes (ii) and (iii) have a lower $\Re(\lambda_i^{OMD})$ value than for the single tone case. In addition, one notices an overall decrease of the modes' $\Re(\lambda_i^{OMD})$ values.

$2iS20W40B$ also shows an overall reduction of the modes' $\Re(\lambda_i^{OMD})$ values, which is stronger than in the case of $2iS20W84B$. This is in line with the faster decay of span-wise coherence when moving downstream of $2iS20W40B$, as observed in fig 4.5.

Fig. 4.8 shows the stream-wise and span-wise velocity components of the mode (i), (ii), (iii) and (iv) for $S20W84B$ and $2iS20W84B$. Note that the re-circulation region right behind the blunt trough is not visible



(a) $S20W84B$ (b) $2iS20W84B$

(c) $S20W40B$ (d) $2iS20W40B$

Figure 4.7: OMD spectra

as the field of view is situated slightly under the wing (cf section 2.2.4). As a reminder from chapter 3, it is the decomposition into stream-wise/span-wise components of the velocity fluctuations induced by the bent shed vortices that creates the symmetric/antisymmetric structures.

When using the multiscale $2iS20W84B$, it is clear from fig. 4.8 that mode (i)'s structures are modified. They are similar in the fact that they are also bent and the symmetry/antisymmetry is the same as for $S20W84B$, however, they appear to be flatter in the center and to have weaker bent edges. This could be due to the stronger variations of the TE pattern, forcing the shed structures to develop into a smaller span-wise extent. Mode (i) represents the idealised arch-shaped vortex shed by the serrations, as previously discussed, and such a difference in this main mode shows the strong effect that the multiscale patterns have on the cell structures in the wake.

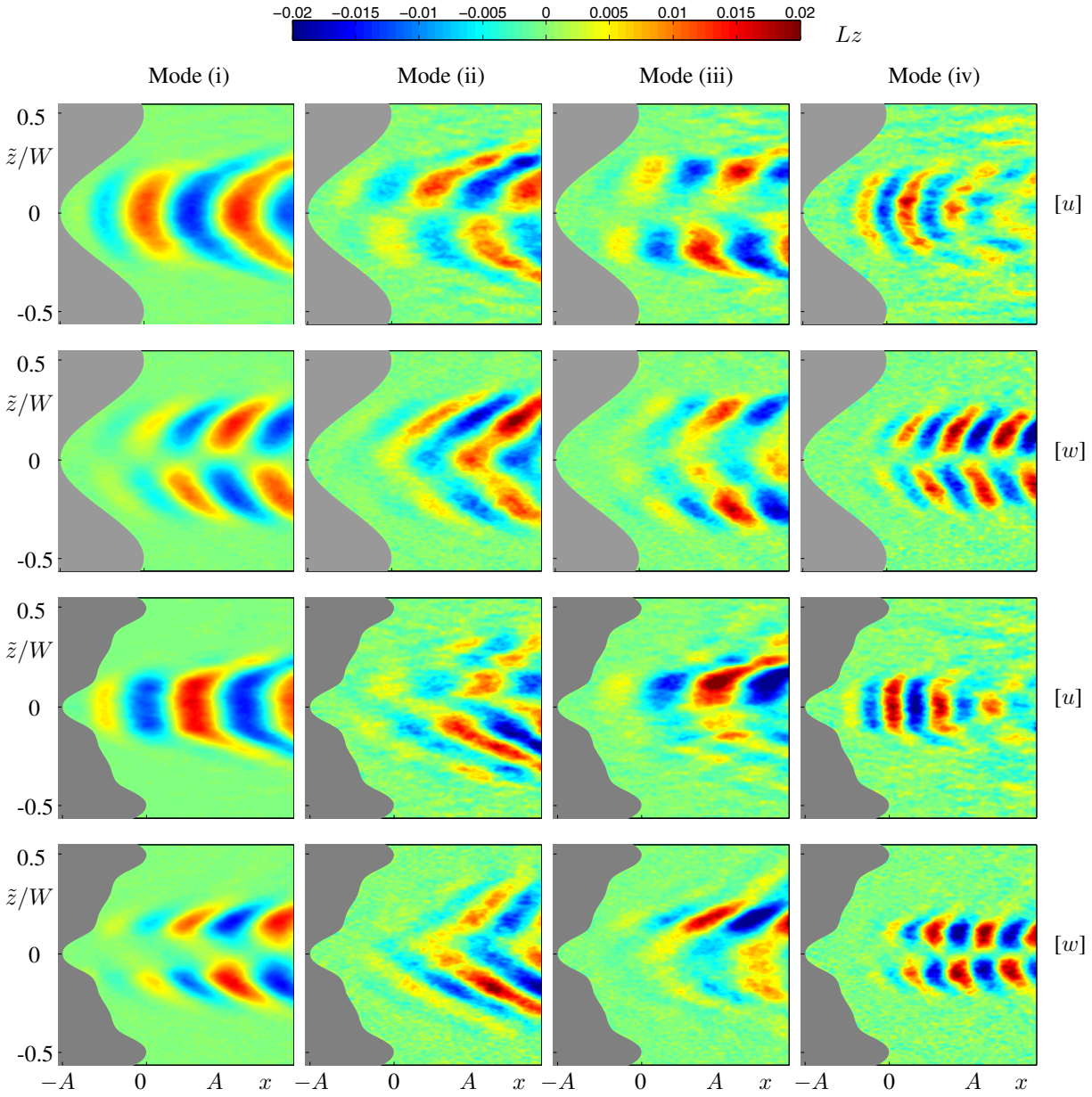


Figure 4.8: OMD modes (i)-(iv) for $S20W84B$ (top two rows) and $2iS20W84B$ (bottom two rows)

Modes (ii) and (iii) are antisymmetric for the stream-wise component, and therefore symmetric for the span-wise component. They are well structured for $S20W84B$, although not as neat as mode (i), but the spatial organisation is less clear for $2iS20W84B$. This is particularly noticeable for mode (ii), as w displays patches in its span-wise evolution unlike the continuous structures of $S20W84B$. This is in fact expected, since $S20W84B$'s spectra showed a clear separation from the $\Re(\lambda_i^{OMD})$ values of modes (ii) and (iii), and those from the rest of the spectra. Such a distinction is not visible for $2iS20W84B$ which means the modes are closer to the background modes, and therefore less meaningful.

Mode (iv) is similar to mode (i), however, the spatial period of the structure is smaller, as well as the associated frequency in the spectra, and there is no harmonic relation between the two. It is most likely a mode adding rippling and breaking down the spatial organisation of mode (i), to tend towards a weaker structure as depicted in fig. 3.13c. The structures in mode (iv) appear more compact and more intense for $2iS20W84B$, which could account for the weaker organisation of the cell downstream of the multiscale trailing edges.

Fig. 4.9 shows mode (i) for $S20W40B$ and $2iS20W40B$. As discussed in section 3.5.2 , the modes are separated for consecutive cells, which is illustrated here by mode (i)-b, corresponding to the main mode of an adjacent cell. For $2iS20W40B$, the structures also appear more compact, similar to what was observed with $2iS20W84B$.

4.1.5 Reynolds stress

In this section, we consider the Reynolds stresses in the wake of the wing to explore the role that such stresses play in shaping the structures shed by the trailing edge. The link between w' and u' had been highlighted with the different structures of the OMD modes, however, this further analysis can be done by looking directly into the time series.

Fig. 4.10 shows the normalised Reynolds stress term $-\overline{u'w'}/U_\infty^2$ in the wake of four trailing edges, obtained from PIV data. For both $S20W40B$ and $S20W84B$, the patterns can be divided in two areas, one close to the trailing edge and one further downstream. However, while $S20W40B$ exhibits high stress close to the trailing edge and little downstream in fig.4.10a, $S20W84B$ shows the opposite in fig.4.10c. In fig.4.10d $2iS20W84B$ shows a reduction of stress downstream and an increase close to the trailing edge, in comparison to $S20W84B$. However, the maximum values remain low compared to the high stress of $S20W40B$. $2iS20W40B$ has very similar patterns to that of $2iS20W84B$. The symmetry observed in all

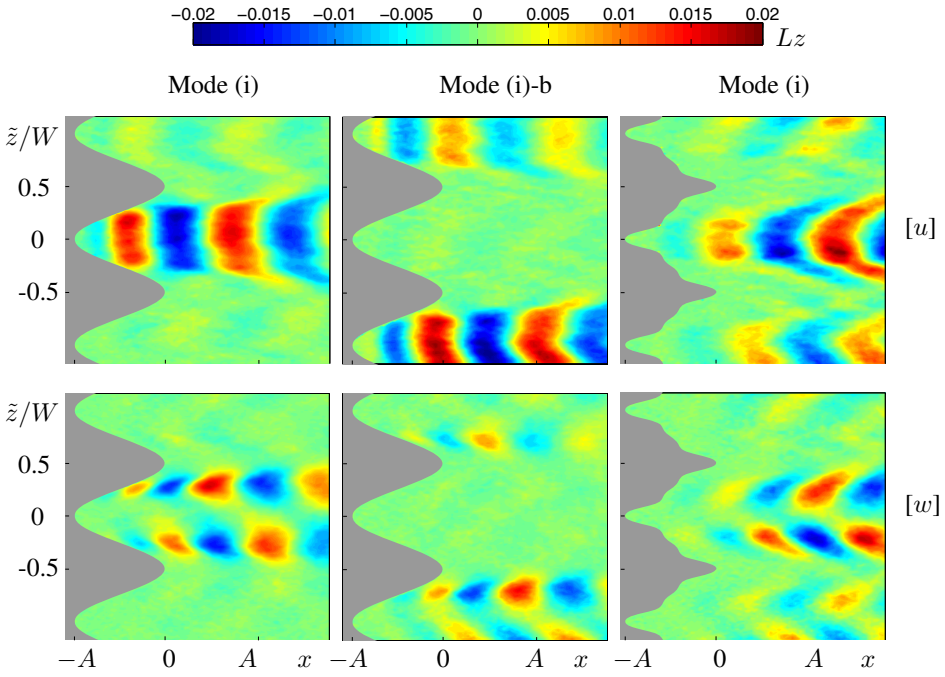


Figure 4.9: normalised OMD mode (i) for $S20W40B$ (left) and $2iS20W40B$ (right). Mode (i)-b is a secondary mode of the main peak.

cases is due to the curvature of the shapes which, as explained for the OMD modes, inverts the sign of the w-component of the fluctuations generated by the shed structures when going from one half of the serration to the other.

Mode (i) for $S20W40B$ is compact and the structure rather straight; and the edges of the structures correspond to the areas of high stress. This high stress, mainly due to u', could thus be constraining the shed structures within a specific area, preventing them from fully developing into a bent shape. On the other hand, $S20W84B$ does not exhibit this region of high stress close to the trailing edge, and its mode (i) is indeed a smoothly bent arch shape. $2iS20W84B$ has a higher stress than $S20W84B$ close to the trailing edge, and its mode (i) displays a structure that is compact and rather straight in the centre, with bent tails, which is in-between those of $S20W84B$'s mode (i) and $S20W40B$'s mode (i).

From hot-wire data, one can estimate the maximum value of $\frac{\partial \overline{U}}{\partial y}$ and compare it to the values found for $\frac{\partial \overline{U}}{\partial z}$ and $\frac{\partial \overline{W}}{\partial x}$ from the PIV data. The two latter are found to be dominated by the first by over an or-

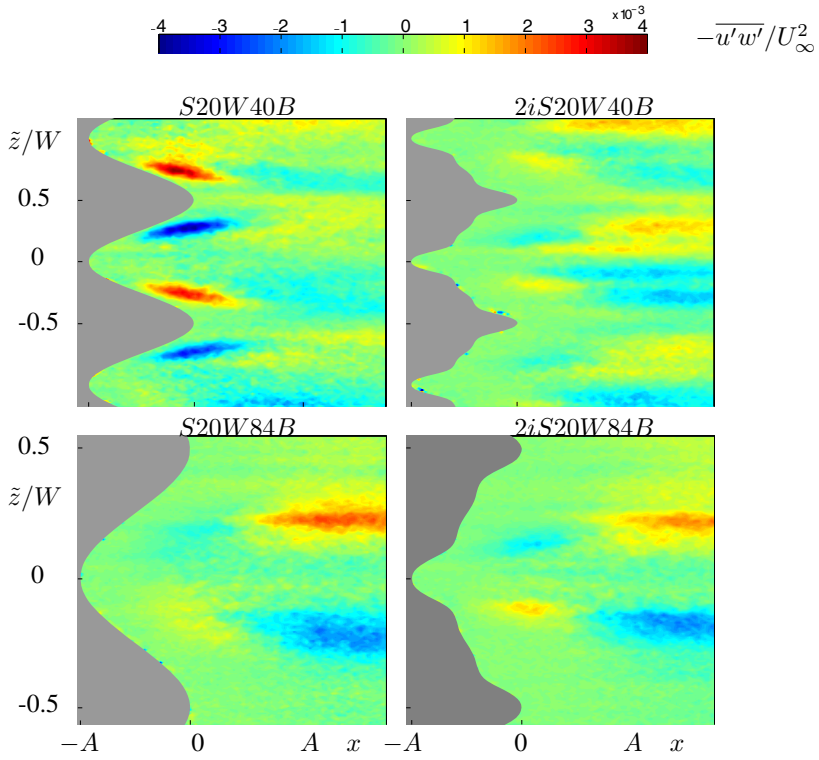


Figure 4.10: Maps of partial Reynolds stress downstream of four tested trailing edges, from PIV data.

der of magnitude. In fact, looking into all production terms available from the PIV data does not provide significant information and does not highlight differences between the tested trailing edges. Indeed, the production term $-\overline{u'w'}\frac{\partial \overline{U}}{\partial z}\frac{c}{U_\infty^3}$ (not plotted here for brevity) displays patterns very similar to that of the previously discussed partial Reynolds stress. Overall, the slight reduction of stress and associated production term downstream of the multiscale trailing edge cannot explain the more rapid downstream decay of coherence and energy previously observed at the shedding frequency. Hence, with these components, one can only say that the stress plays a role in shaping the structures shed by the trailing edges by limiting their span-wise development.

4.2 Sharp trailing edge geometry approach

The cut-in approach followed to obtain the sinusoidal trailing edge inherently produces bluntness at the troughs which causes vortex shedding and coherence at the corresponding St_{sh}. In order to keep the structural benefits of this approach and to mitigate the associated effects, another design is introduced for the trailing edges. Instead of directly cutting into the wing, its aft part is modulated with a sinusoidal pattern, leaving the airfoil section unmodified at the peaks and introducing a steep trailing edge at the trough. Section 2.1.2 provides an illustration of this approach. This modification introduces some inherent waviness to the surface of the trailing edge, which may have some impact on account of the important role of span-wise flow in breaking down coherence, as discussed previously. Indeed, wings with rippled trailing edges were studied by Werle and Patterson [72], who highlighted the presence of span-wise flow on the aft part of such wings.

4.2.1 Boundary layer measurements

The hot-wire measurements used to obtain the data discussed hereafter are detailed in section 2.2.2.

The previous definition of St used for the spectral analysis is not applicable, as h does not represent a real parameter of the sharp cases. Instead, one could consider using an 'effective viscous' bluntness, defined as the sum of boundary layer displacement thickness on upper and lower surfaces: $(\delta^*_{pressure} + \delta^*_{suction})$ where the displacement thickness δ^* is defined as

$$\delta^* \equiv \int_0^\delta 1 - \frac{\bar{U}}{U_\infty}\, dy, \tag{4.1}$$

since it describes the effective separation between the two meeting shear layers. Given that the lifting wing creates a velocity gradient in the free stream, the usual definition of δ_{99} is harder to apply. Instead, one can look into the wall normal evolution of intermittency. Klebanoff [38] proposed an approximation of the intermittency function by the following expression towards the edge of the boundary layer:

$$\gamma_i = 3\frac{\overline{u'^2}^2}{\overline{u'^4}}. \tag{4.2}$$

This corresponds to the inverse of the kurtosis of u', with a factor 3 for normalisation. Fig. 4.11 shows the evolution of γ_i when traversing away from the wall, on the pressure side of $S20W84B$ at the trough. For $y/c < 10^{-2}$, values are comprised between 1 and 1.2, which corresponds to that reported by Klebanoff

[38] for a turbulent boundary layer with zero pressure gradient. The intermittency then drops, which marks the edge of the boundary layer. However, after $y/c = 0.027$, γ_i rises again, which was not expected; for that purpose $\overline{u'^2}$ and $\overline{u'^4}$ are also plotted. Both go to zero at around $y/c = 0.027$ which corresponds to the observed minimum of intermittency, the subsequent high values are thus more likely due to noise in the ratio of two factors tending towards 0. The exact determination of the boundary layer thickness is done by Klebanoff [38] by fitting the function $\frac{1}{2}.(1 - erf(5.(y/\delta - 0.78)))$. In the present case however, the boundary layer is likely to be subjected to an adverse pressure gradient, and as a result, such fitting does not yield satisfactory results. Given that the study of the boundary layer is not the prime objective but rather a means to the estimation of St^*, the value of δ was determined by using the local minimum of γ_i.

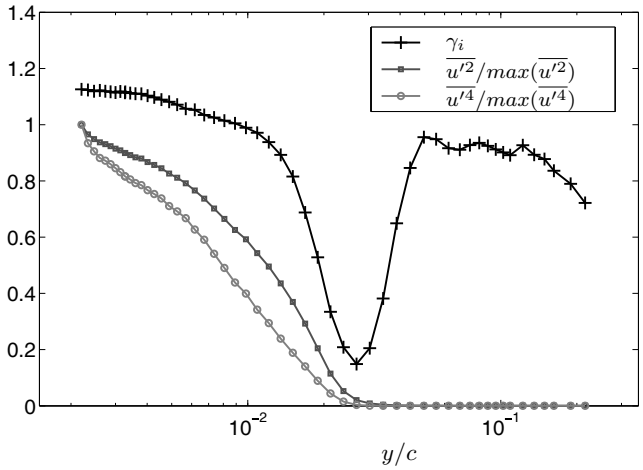


Figure 4.11: cross-stream evolution of intermittency for the pressure side of $S20W84B$ at the trough.

A logical approach is to combine $\delta^*_{pressure}$ and $\delta^*_{suction}$ for the definition of the Strouhal number. This was tested on $S20W00B$, $S20W40B$ and $S20W84B$ since these wings exhibit a clear shedding spike that gives a specific frequency to focus the test on. It was observed the use of both $\delta^*_{pressure}$ and $\delta^*_{suction}$ gives scattered values of St^*_{sh}, which remain close together if only $\delta^*_{pressure}$ is used. Hence, for the sharp cases, the following definition was chosen for St^* and shall be used in the following sections:

$$St^* = f.\delta^*_{pressure}/U_\infty. \tag{4.3}$$

4.2.2 Spectra and coherence

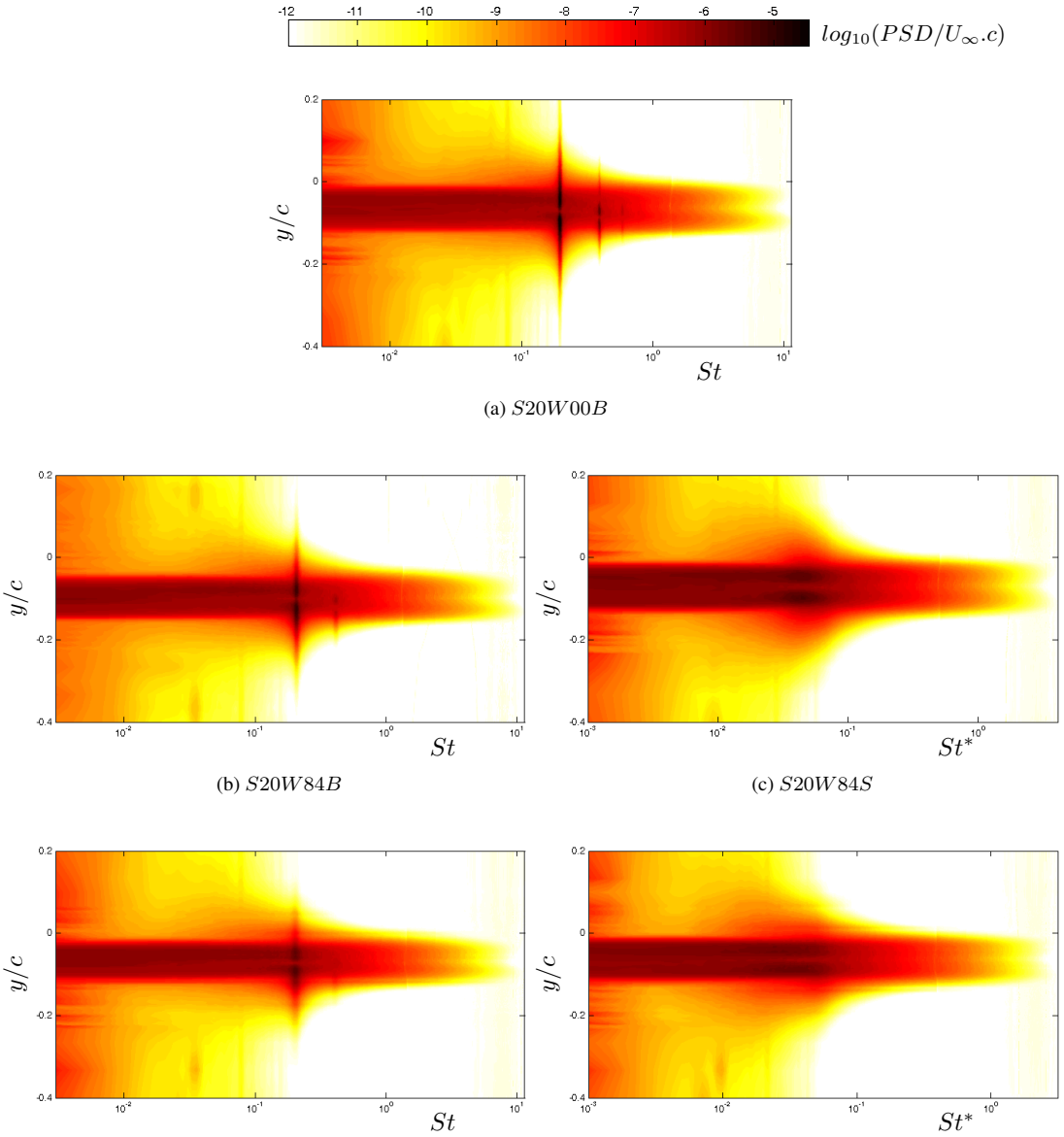
In order to study the effect of the sharpness on the spectra, vertical PSD traverses have been plotted for the sharp TE geometries, alongside the blunt TE in fig. 4.12

Fig. 4.12c and 4.12e show the PSD map for $S20W84S$ and $S20W40S$ respectively, at $x/c = 0.04$. The spectrum map displays a region of higher intensity, more broadband than in the blunt cases and no harmonic is seen. The maximum values are also lower than in the blunt case.

Fig. 4.13 compares the spectra between blunt and sharp trailing edges for both wavelengths at a given vertical position. The spectra are plotted against frequency, as St^* was observed not to collapse the spectra between blunt and sharp. The sharp spectra have indeed lower maximum values and more broadband bumps than the blunt, and a shift towards lower frequencies is observed. This shift to lower frequencies is counter-intuitive; however it is consistent with Zobeiri *et al.* [75], who studied the vortex shedding from an oblique/beveled trailing edge on a hydrofoil and observed a lower shedding frequency than with a blunt trailing edge. The design of the sharp TE in our study could be locally seen as an oblique shape, which would be consistent with the shift we observe. As for the more broad-band nature of the bump in the spectra, a possible explanation is that the waviness of the surface locally increases mixing and therefore alters the single tone characteristic. Both wavelengths show that the sharp trailing edges have higher values of the spectra in the low frequency range. In fact, when integrating the full vertical traverses from fig. 4.12, over both frequencies and vertical extent, the ratio of total energy is 1.6 between $S20W84S$ & $S20W84B$ and 1.3 between $S20W40S$ & $S20W40B$. This means that the sharp trailing edges not only spread the energy over a larger band of frequencies, but actually increase the total energy in the wake.

Fig. 4.14 shows vertical traverses of coherence between trough and mid-point at a position $x/c = 0.04$ downstream of $S20W84S$, $S20W84B$ and $S00W00S$ (the probes' positions being based on the former TE). One notices a band of coherence at $St^* = 9.10^{-3}$ for $S00W00S$, however this is also observed in all other cases at the same frequency [Hz] and thus at different values of St^* and St. This band corresponds to a very low energy content according to fig. 3.4 and is not observed when no wing is installed; it is likely due to a blockage instability caused by the wing.

Contrary to the blunt case, $S20W84S$ does not display coherence in the wake area around the value of St^* for the bump seen in the spectra. In this sense, the coherence between trough and mid-point behind $S20W84S$ is very similar to that of the unmodified wing, $S00W00S$. In contrast, comparison of figs 4.14b and 4.14c reveals a reduction of coherence is achieved over a broad range of St on the edges of



(a) $S20W00B$

(b) $S20W84B$

(c) $S20W84S$

(d) $S20W40B$

(e) $S20W40S$

Figure 4.12: Vertical PSD log_{10} map at $x/c = 0.04$ behind the TEs troughs

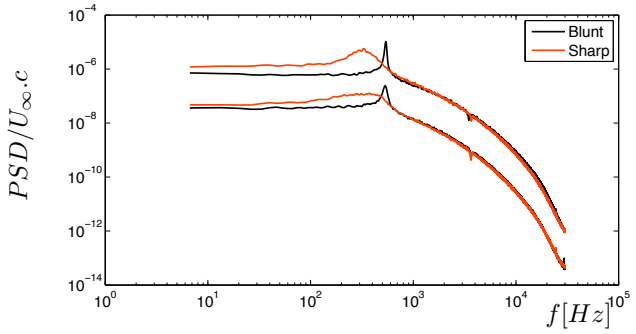
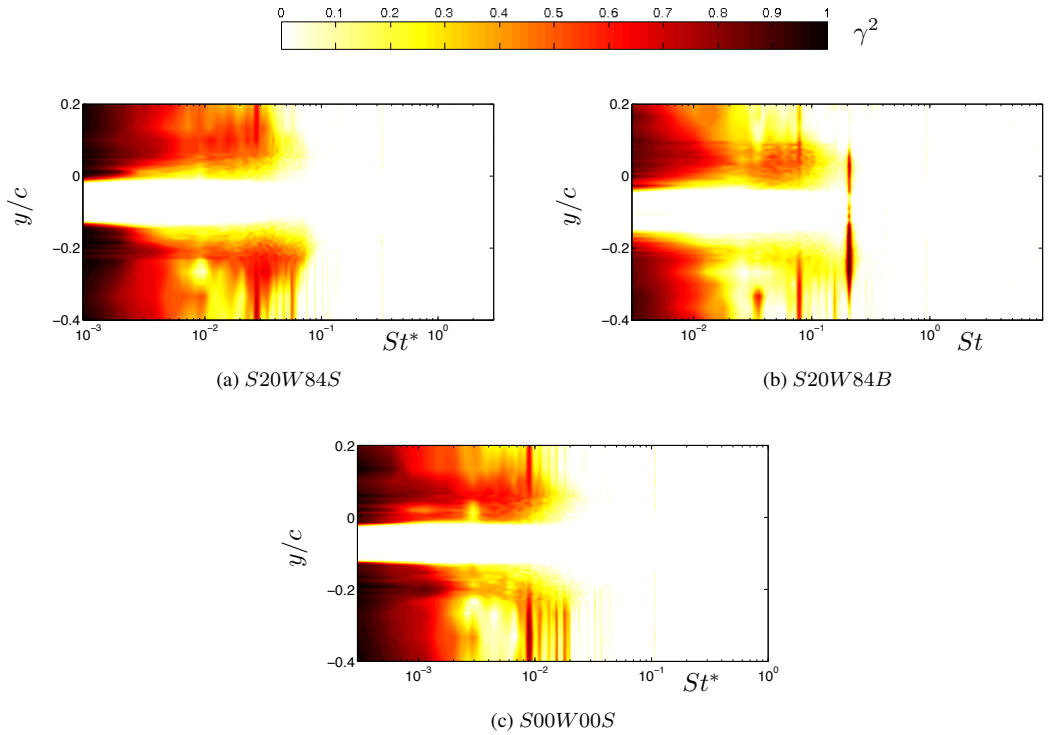


Figure 4.13: Spectra of $S20W84B$ & $S20W84S$ (top) and $S20W40B$ & $S20W40S$ (bottom), at $x/c = 0.04$



(a) $S20W84S$

(b) $S20W84B$

(c) $S00W00S$

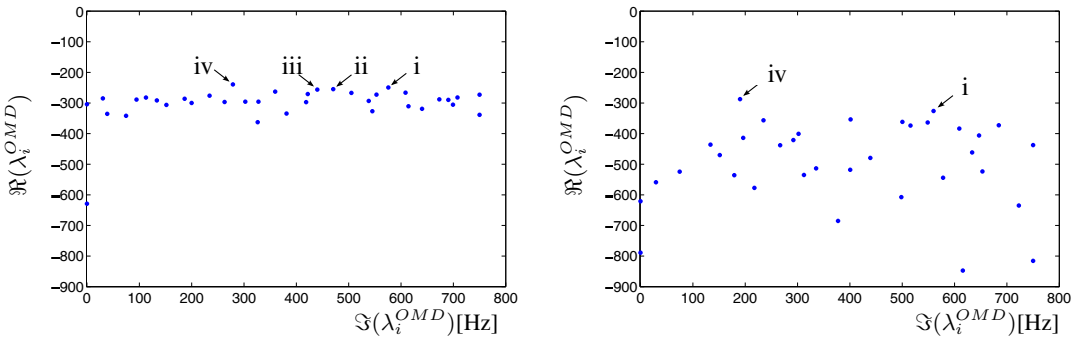
Figure 4.14: γ^2 map (Trough - Mid-point) behind $S20W84S$, $S20W84B$ and $S00W00S$ at $x/c = 0.04$

the wake between $S00W00S$ and $S20W84B$, at the cost of a high correlation at the shedding Strouhal number. $S20W84S$ does not achieve such a significant broadband reduction, but the absence of coherence at a discrete shedding frequency in the wake is encouraging for further studies.

4.2.3 OMD modes of sharp TE

Given the strong effect observed on the coherence and vortex shedding in the wake, the flow structure should also be strongly affected. For that reason, the OMD previously used for the study of the vortex shedding cells is now applied to the flow behind the sharp trailing edges.

Fig. 4.15 shows the OMD spectra for $S20W84S$ and $S20W40S$. The most striking feature is the lack of any distinct dominant mode and also the low values exhibited by all modes, in comparison to the blunt cases from fig. 4.7. Nevertheless, four modes in fig. 4.15a are selected and worth noticing due to their slightly higher values, their clear spatial arrangement contained within a serrations' extent, and for mode (i), its frequency close to that of blunt vortex shedding . Indeed, mode (i) has a frequency just under that of $S20W84B$ mode (i). From fig. 4.13 we know that the sharp cases do not exhibit a clear shedding spike, but rather have a broadband signature at a lower frequency. This first mode could thus be one of the main component of this phenomena. The broadband characteristic means it involves more modes at different frequencies and that they likely interact with each other. It is therefore unsurprising that the linear formalisation of OMD renders it of limited use as a tool for the analysis of the wake in this case. It is nonetheless interesting to highlight the differences observed between the blunt and sharp cases.



(a) $S20W84S$ (b) $S20W40S$

Figure 4.15: OMD spectra

Fig. 4.16 shows the modes (i)-(iv) for $S20W84S$. First of all, one notices that the span-wise components of the modes are relatively weaker than the stream-wise, while more balanced structures (in terms of peak strength) were observed for the blunt cases in fig. 4.8. This is rather surprising as one might expect the

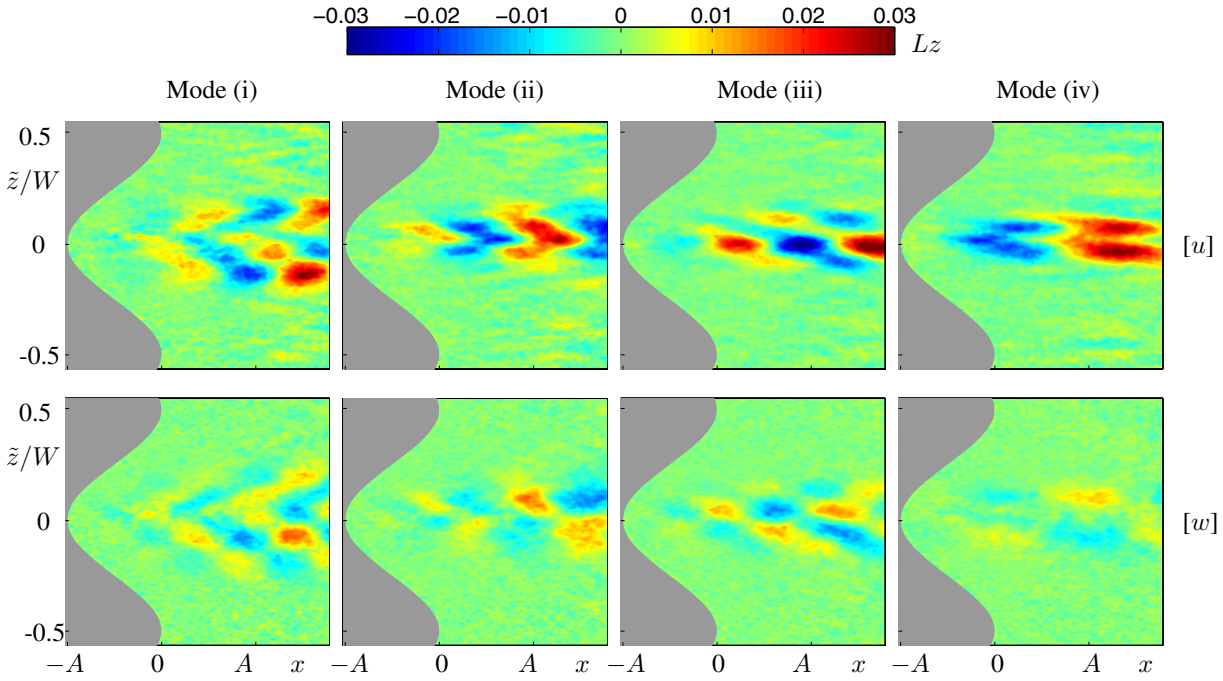


Figure 4.16: OMD modes (i)-(iv) for $S20W84S$.

waviness of the trailing edge surface to promote more span-wise flow. A possible explanation is that due to the absence of bluntness, the previously discussed cross-flow, from peak to trough, is weakened in this configuration and in turns the structures associated to the broadband bump in the spectra are not as bent as in the blunt cases. It has already been mentioned that the span-wise component was the result of the velocity fluctuations induced by non-span-wise vorticity; the lack of bending of the structures would therefore limit this effect.

Mode (i) exhibits a V shape, which somewhat resembles mode (ii) for $2iS20W84B$, although visibly weakened and made out of patches. Other modes, not plotted here, have very similar spatial structures, due to the broadband characteristic of such structures as previously discussed. Mode (iii) is more compact with more focused fluctuations close to the center of the wake. Mode (ii) has an inverted V shape, more compact than the one observed for mode (i), but its span-wise component is very similar to mode (iii). Mode (iv) on the other hand is more elongated in the stream-wise direction, and also compact in the center of the wake.

Over all, the different structures of these modes, and the fact that they occur at various frequencies

playing a role in the dynamics of the wake, shows that the cell structure previously observed cannot be characterised in this case.

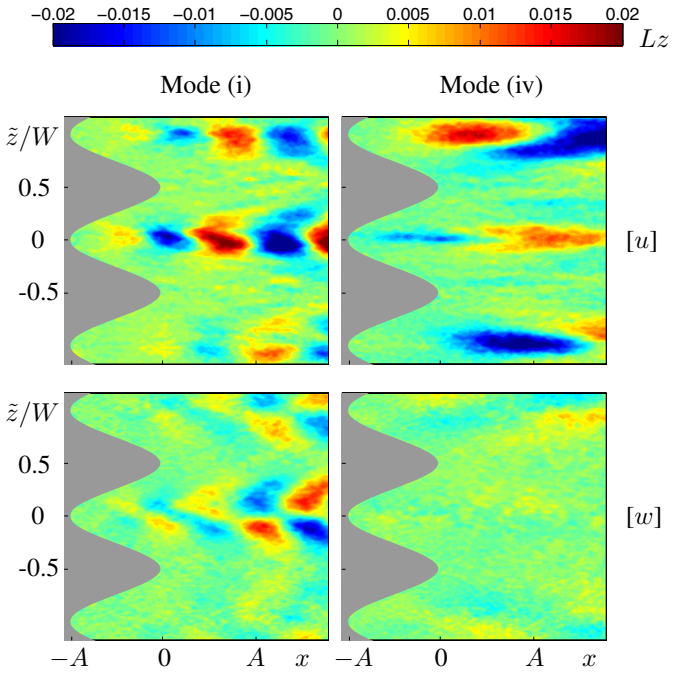


Figure 4.17: OMD mode (i) and (iv) for $S20W40S$.

Fig. 4.15b shows that the spectra values for $S20W40S$ are even lower than for $S20W84S$. One result of this being that two relatively distinct modes can be identified. Mode (i) corresponds to the same frequency as previously, however mode (iv) - the most significant one - is now picked up at a lower frequency. In fig. 4.17, mode(i) displays a compact structure, in the center of the wake, in between mode (i) and (iii) from $S20W84S$. The main difference with the blunt case, even more so with the single tone sinusoidal one, is that the fluctuations are organised in compact patches and not as arch shapes. Mode (iv) represents a very fine structure, elongated in the stream-wise direction. Overall, the modes observed in the wake of sharp trailing edges show a more compact structure with less span-wise component than in the blunt cases. Along with the spectral information, this illustrates the fact that there is no clear vortex shedding in those wakes, which explains the difference in the coherence measured between blunt and sharp sinusoidal trailing edges.

4.3 Discussion and concluding remarks

Two separate approaches were investigated in an effort to modify the previously observed vortex shedding cell structures and the associated span-wise coherence in the wake of a wing with a cut-in sinusoidal trailing edge. The first one is to introduce multiscale patterns to promote flow mixing in the trough and break down those cells. The second is to maintain sharpness at the trailing edge by modulating the aft part of the wing, rather than just cutting into the trailing edge.

Cell structures are observed in the case of multiscale TEs, by both the study of de-phasing and Optimal Mode Decomposition. However, they are weaker than in the single tone cases. By weakening the cell structures, the use of multiscale patterns leads to a strong decrease of vortex shedding energy and associated coherence. It is also observed that the low frequency coherence introduced near the troughs of the single tone sinusoidal TEs is further decreased, by up to 57%.

The introduction of a sharp sinusoidal trailing edge removes the shedding signal measured in the wake behind the trough, and replaces it with a broadband equivalent. On large scales, the span-wise coherence on the edges of the wake is less affected than by a blunt trailing edge, however, no coherence attributed to shedding phenomena is measured. OMD in the wake of such trailing edges reveals a more compact and weaker structure, inducing fluctuations mainly in the stream-wise direction.

In conclusion, the introduction of cut-in serrations exhibits bluntness that in turn generates vortex shedding that locks into a bent cell structure. This shedding is however weaker than that of a straight trailing edge of the same maximal bluntness. The use of multiscale patterns weakens the cell structures which translates into a reduction of vortex shedding intensity as well as a reduction of span-wise correlation at both vortex shedding and low frequencies. The use of an alternative sharp approach is a compromise that gives less coherence reduction on the edges of the wake but avoids the introduction of a clear vortex shedding signal.

Chapter 5

Coherent incoming flow

The work presented in this section was undertaken during a secondment with Forwind research centre for wind energy at the University of Oldenburg, Germany.

5.1 Background and approach

The two previous chapters have looked into the understanding and disruption of the flow structures generated by the cut-in approach chosen for the serrations. However, by essence, these structures are a self-imposed problem. For that reason, the present chapter focuses on the way trailing edge geometry affects the behaviour of wings subjected to unsteady incoming flows. In most applications, the wing or blade is not subjected to a laminar flow at constant angle of attack, but rather to a more complex flow whose properties often vary in time. This is particularly true in the case of wind turbines, that are subjected to atmospheric turbulence, wind gusts, turbulent wakes of upstream turbines etc. Modern wind turbines are capable of adapting themselves to flow conditions by varying their orientation or the pitch of their blades. However, rapid variations of the geometrical angle of attack during a wind gust, or non-uniform variations along the span or chord of the wing, limit these adaptations to slow variations of mean properties.

Research has been conducted in the past years on the topic of atmospheric turbulence and the creation, in wind tunnels, of flows with representative properties. In particular, the use of an active grid at Forwind research center has proven useful in creating flows with specific statistics [39], in order to study the behaviour of wind turbines under unsteady inflow conditions [64][65]. Other studies [37] [19] have

considered isolated blades and looked into their load response under unsteady inflows.

Such flows can thus be used to study how trailing edge serration patterns can affect incoming coherence. The active grid, developed by the research group at Forwind Institute, is presented in section 2.3.1, along with the protocols used hereafter. In short, four protocols are studied: a sinusoidal variation of the flow incidence, Gaussian and intermittent inflows, and a bluff-body-like protocol inducing both a turbulent flow and a strong single tone excitation with high span-wise coherence.

5.2 Coherence

To study the incoming coherence, hot-wire measurements were carried out in the wake of the wing with cut-in serrations, subjected to the protocols previously listed. As detailed in section 2.3.2, eight probes were positioned at $x/c = 0.04$, to span one and a half wavelengths, with the first five closer together to have a higher spatial resolution of the coherence. The probes were in a fixed position with regards to the wing, and therefore rotated along with it at different geometrical mean angles of attack.

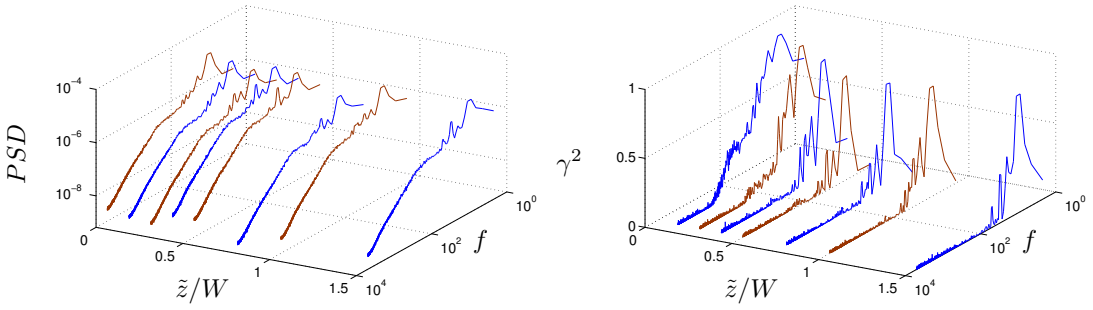
Detailed study of the transient aerodynamics of such a complex set up would require time resolved measurements of the flow around the wing. Since the measurements performed are limited to the wake, a black box approach is taken for the analysis of the coherence: the same inflows are generated for different wings, and the coherence is measured in their wake. It is thus possible that the measured coherence is a combination of that generated by the wing itself (e.g. trailing edge vortex shedding) and that directly from the incoming flow. In both cases, the present section focuses on the differences between the wakes of the tested trailing edges.

5.2.1 Results from the sinusoidal protocol

Before placing the wing into the wind tunnel, measurements were conducted with the hot wires at their final position, corresponding to the set up with zero geometric angle of attack. This enabled the characterisation of the PSD and coherence generated by the protocol. As previously mentioned, the aim is not to obtain a detailed understanding of the flow structures, but rather to highlight the spectral characteristics generated for comparison against the airfoil wake flows.

Fig. 5.1a shows the PSD at each span-wise position and fig. 5.1b the coherence between one trough ($\tilde{z}/W = 0$) and the seven other positions. The PSD shows rather constant spectra across the covered span,

with a main peak corresponding to the frequency of the protocol, harmonics and then a rapid decay. It should be noted that due to the symmetry of the set-up with regards to the $x - z$ plane and the fact that the hot-wire probes are mounted in the z direction, the peak is measured at $10\,\text{Hz}$, which is twice that of the protocol's frequency. Indeed, the hot-wire probes are single wires and will not differentiate the two halves of the shedding period so long as they are symmetric, therefore artificially doubling the frequency of the measured phenomena. The coherence is particularly interesting, as one can see that the initial broadband coherence visible for the smallest separation ($\tilde{z}/W = 0.125$) rapidly diminishes until only the main peak and its harmonics are visible for $\tilde{z}/W \geqslant 0.4$. This broadband coherence can be attributed to the turbulent flow created by the flaps of the grid, and it is therefore expected that its span-wise extent be small. On the other hand, the large span-wise extent of coherence at the protocol's frequency, and its harmonics, is actually the effect of varying the flow direction rather than actual vortical structures.



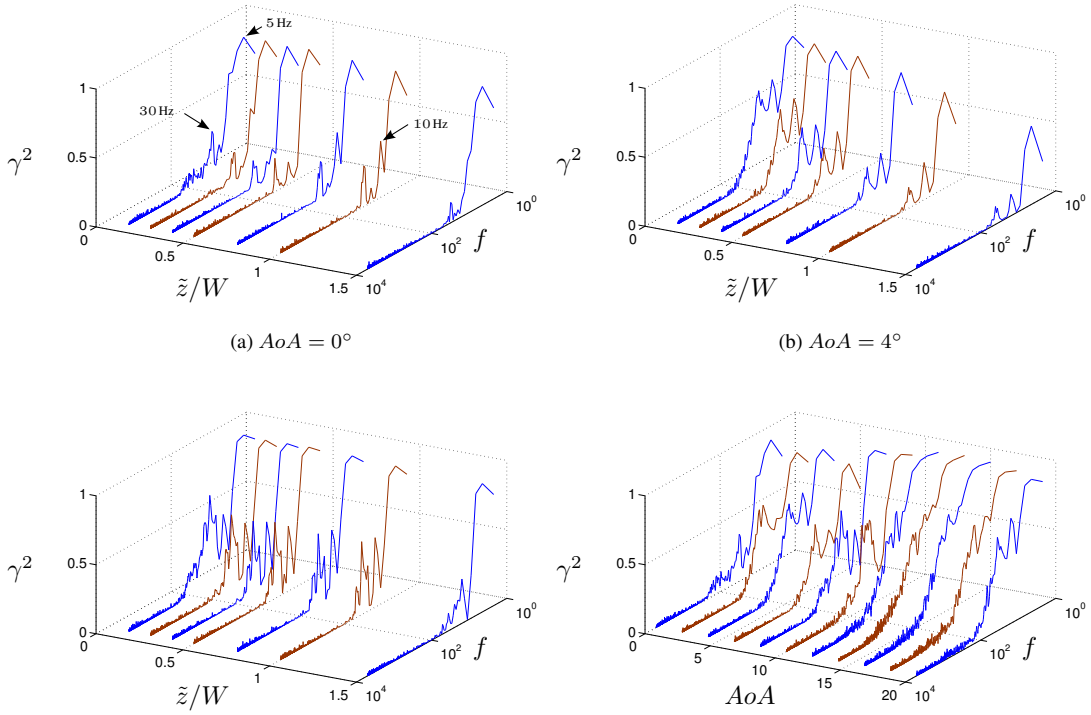
(a) PSD (b) γ^2

Figure 5.1: Sinusoidal protocol: PSD and coherence without wing. Alternated colours for ease of visualisation.

Fig. 5.2a-5.2c show the coherence between a trough ($\tilde{z}/W = 0$) and seven other positions, in the wake of the unmodified wing subjected to the sinusoidal protocol, at three different geometric incidences. Fig. 5.2d shows the $\tilde{z}/W = 1/8$ coherence values for all tested incidences.

At zero incidence, the main peak at $5\,\text{Hz}$ is clear at all positions, with a secondary peak visible at $10\,\text{Hz}$, due to the symmetry of the set-up at zero incidence. Higher harmonics are also visible at $15\,\text{Hz}$ and $30\,\text{Hz}$. At $AoA = 4°$, these higher harmonics appear more coherent in particular at 15, 25 and $35\,\text{Hz}$, as well as a broadband component persistent until $\tilde{z}/W = 0.5$. The $10\,\text{Hz}$ peak is not visible as the incidence removes the symmetry of the set-up and therefore prevents the artificial doubling of measured frequencies.

At $AoA = 8°$, the peak values of these harmonics increase, most likely due to more complex, transient dynamics of the flow approaching pre-stall conditions during part of the protocol period. When isolating the coherence at $\tilde{z}/W = 1/8$ for all incidences, it is clear that increasing the angle of attack first increases the values of such harmonics, then makes the signal more broadband. When getting close to $AoA = 10°$, dynamic stall is expected since the mean value of the angle of attack approaches the stall angle in steady inflow conditions.



(a) $AoA = 0°$

(b) $AoA = 4°$

(c) $AoA = 8°$

(d) All AoA, $Z/W = 1/8$

Figure 5.2: Sinusoidal protocol: γ^2 downstream of $S00W00S^*$, relative to the trough ($\tilde{z}/W = 0$). Alternated colours for ease of visualisation.

Fig. 5.3 shows the coherence with $\tilde{z}/W = 1/8$ separation to the reference in the trough for the four tested trailing edges (and without wing for reference) subjected to the sinusoidal protocol. Fig. 5.3a shows that without geometric incidence, all trailing edges reduce the coherence compared to the case without any wing installed, with the exception of a shedding spike (corresponding to the one discussed in the previous

chapters) for those exhibiting bluntness. With that regard, the unmodified base wing displays the strongest overall reduction of coherence. At zero incidence, $S20W00B^*$ does not exhibit the doubling of frequency for the vortex shedding as the others do; it can be due to 3-D instabilities developing along the span of the blunt edge and reducing the symmetry of the shedding. Fig. 5.3b shows similar results for a geometric incidence of $4°$; the case without the wing (and no incidence of the HW probes) is left for reference. All modified trailing edges have lower broadband levels of coherence than the base wing ($S00W00S^*$), with $2iS20W40B^*$ and $S20W00B^*$ displaying similar values. At the shedding frequency (~ 580 Hz), the sinusoidal serrations have a stronger spike, at $\gamma^2 = 0.44$, than $2iS20W40B^*$ at $\gamma^2 = 0.24$ and $S20W00B^*$ at $\gamma^2 = 0.17$. However, $S20W00B^*$ also exhibits a small spike at the harmonic, so the difference from $2iS20W40B^*$ is in fact smaller.

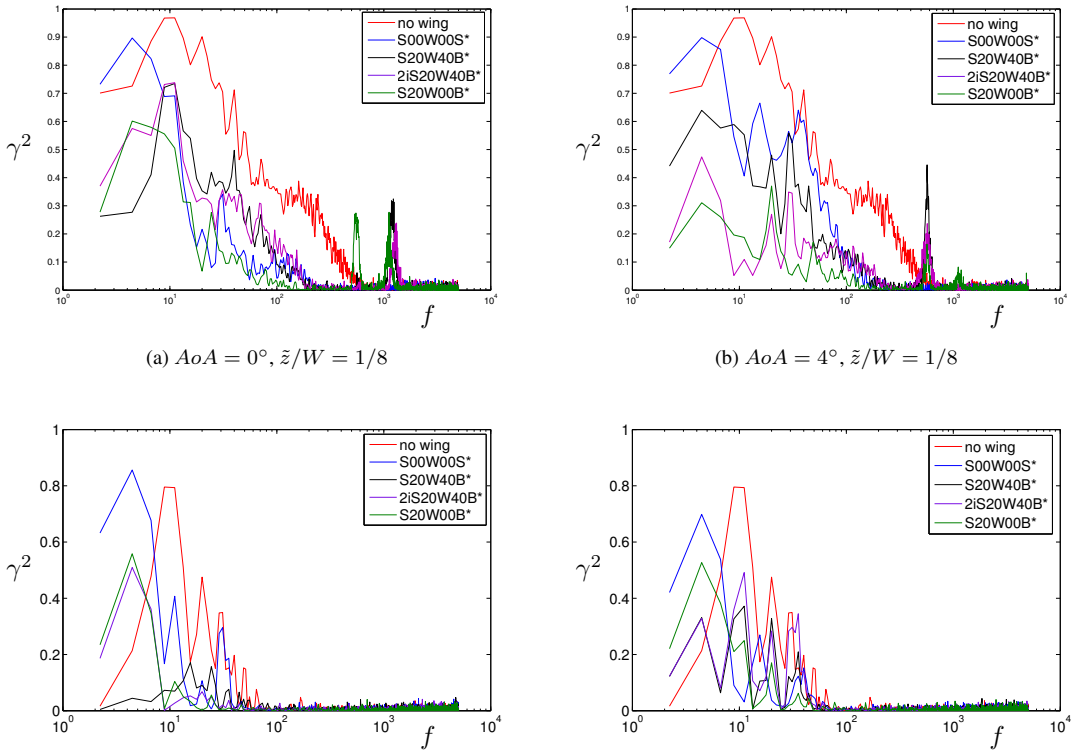
Fig. 5.3 also shows the coherence with $\tilde{z}/W = 1$ separation, that is between two adjacent troughs. It is clear that only low frequency coherence is visible, most likely due to the dynamics of the flow imposed on the wing by the protocol. No coherence is seen at the vortex shedding frequency between these two troughs, which is in line with the findings from the previous chapters.

Fig. 5.4 shows the spectra measured downstream of the trough ($\tilde{z}/W = 0$) for the same trailing edges. Although the introduction of the wing (with or without modified trailing edges) reduces the coherence, it is clear that the energy levels are increased in the spectra. It is worth noting that $S20W00B^*$ has the highest levels of energy, which adds to the comparison with $2iS20W40B^*$, which not only appears to better reduce the span-wise coherence but also has lower energy content in the trough.

Therefore, it seems that TE serrations reduce the incoming coherence more than an unmodified wing, when the wing is at incidence. The multiscale serrations then display a stronger reduction of coherence, and exhibit similar values to those of a blunt trailing edge but associated with lower energy. *N.B.*: from chapter 4, it is known that in the case of laminar inflow, the 2-iteration case has a significantly lower self-generated coherence than the blunt case, the difference being less obvious here.

5.2.2 45deg protocol

The aim of the "45deg" protocol is to use the active grid as a vibrating bluff body. For this, the three vertical axes in the middle of the test section oscillate at 25 Hz around a mean position of $45°$, as detailed in section 2.3.1. Fig. 5.5 shows the PSD and coherence measured with this protocol, without the wing. All of the spectra are very similar with a small peak at 25 Hz. All span-wise positions exhibit a clear peak at



(a) $AoA = 0°$, $\tilde{z}/W = 1/8$

(b) $AoA = 4°$, $\tilde{z}/W = 1/8$

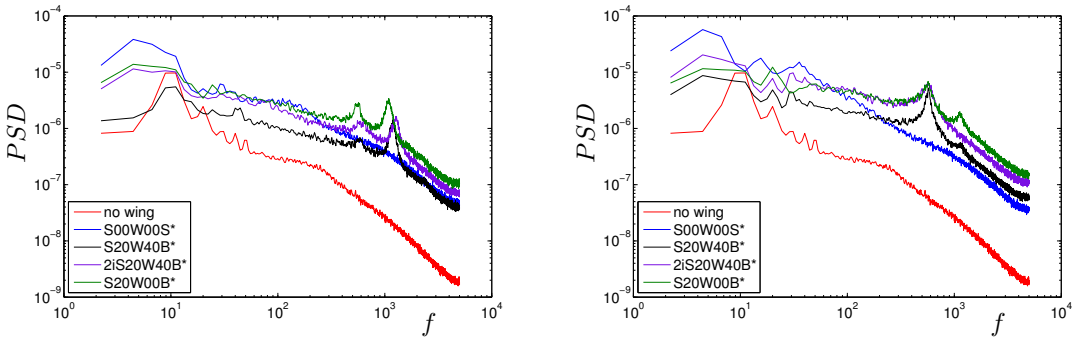
(c) $AoA = 0°$, $\tilde{z}/W = 1$

(d) $AoA = 4°$, $\tilde{z}/W = 1$

Figure 5.3: Sinusoidal protocol: γ^2 for all TEs.

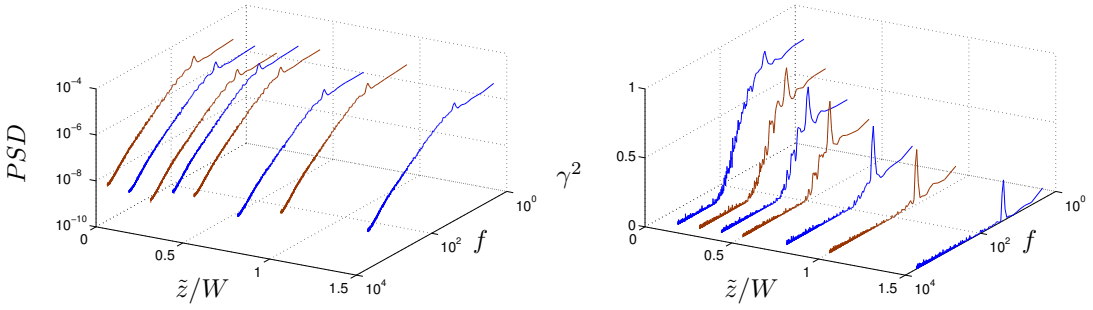
this main frequency, with a broadband component of coherence progressively disappearing until $\tilde{z}/W = 1$. To that extent, this protocol generates an inflow with coherence at a higher frequency than the sinusoidal protocol and over a larger span-wise extent, most likely created by the simultaneous detachment of the flow around the flaps and the small variation in blockage ratio, rather than the variation of the angle of attack.

Fig. 5.6a-5.6c show the coherence between a trough and seven other positions, in the wake of the unmodified wing ($S00W00S^*$) subjected to the "45deg" protocol, at three different geometric incidences. For all three values of incidence, there is a clear peak of coherence at 25 Hz. Its span-wise evolution is monotonic, except at zero-incidence, and the values of the peaks grow with incidence. A broadband component also grows with incidence at small separation, which is clear in fig. 5.6d, as for the previous protocol. This is mainly explained by the proximity of stall, which induces a more broadband dynamic behaviour of the



(a) $AoA = 0°$, $\tilde{z}/W = 1/8$ (b) $AoA = 4°$, $\tilde{z}/W = 1/8$

Figure 5.4: Sinusoidal protocol: PSD for all TEs, $\tilde{z}/W = 0$

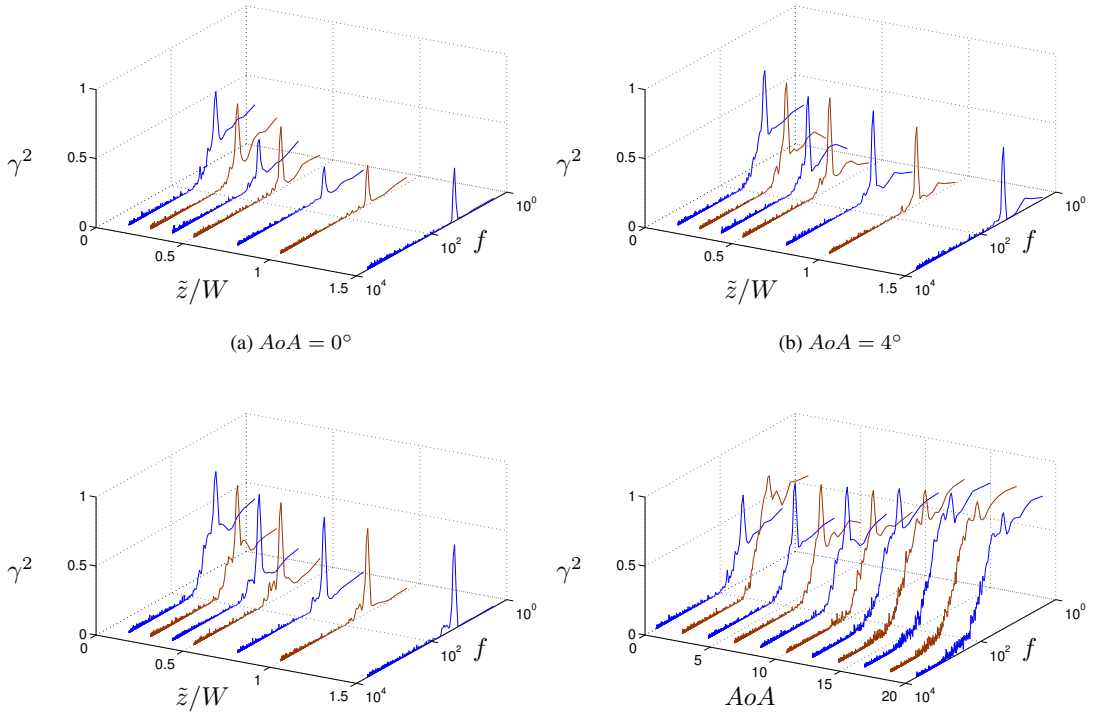


(a) PSD (b) γ^2

Figure 5.5: 45deg protocol: PSD and coherence without wing. Alternated colours for ease of visualisation.

flow around the airfoil. *N.B.*: in this case, even at $AoA = 0°$, a spike of both PSD and coherence is observed at 25 Hz, and not double that since the mean position of the active grid's flaps at $45°$ from the mean flow direction makes the protocol inherently asymmetric.

In order to compare the trailing edges, fig. 5.8 shows the coherence at $\tilde{z}/W = 1/8$ separation for all tested cases (and without the wing for reference) at zero and $4°$ incidence. It is clear that at zero incidence, the unmodified wing ($S00W00S^*$) displays lower coherence at $\tilde{z}/W = 1/8$ separation than both the straight blunt ($S20W00B^*$) and 2-iteration ($2iS20W40B^*$) cases. The difference is smaller at $4°$ incidence, but the trend is maintained. In both cases though, $2iS20W40B^*$ has slightly lower broadband



(a) $AoA = 0°$

(b) $AoA = 4°$

(c) $AoA = 8°$

(d) All AoA, $\tilde{z}/W = 1/8$

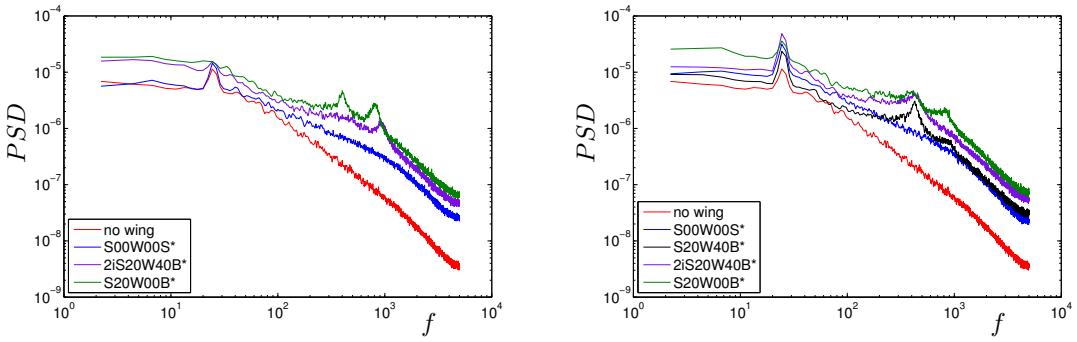
Figure 5.6: 45deg protocol: γ^2 downstream of $S00W00S^*$. Alternated colours for ease of visualisation.

coherence than $S20W00B^*$, along with lower values at the shedding frequency.

Fig. 5.8 also shows the coherence between two adjacent troughs ($\tilde{z}/W = 1$). Apart from the frequency impose by the protocol (25 Hz), no coherence is seen between the two troughs, even at the vortex shedding frequency, as it is the case within one cell measured with $\tilde{z}/W = 1/8$ separation of the probes.

Fig. 5.7 shows the spectra measured downstream of the trough ($\tilde{z}/W = 0$) for the same trailing edges. Once again, $S20W00B^*$ exhibits the highest level of energy overall, and the unmodified wing displays the lowest of all tested wings. This adds to the previous comment that for this protocol, the unmodified wing appears to be the most efficient at reducing the incoming coherence and associated energy over a broadband range of frequencies.

Fig. 5.9 shows the span-wise evolution of the peak value of coherence ($\gamma^2(25\,\text{Hz})$) for the different



(a) $AoA = 0°$, $\tilde{z}/W = 1/8$

(b) $AoA = 4°$, $\tilde{z}/W = 1/8$

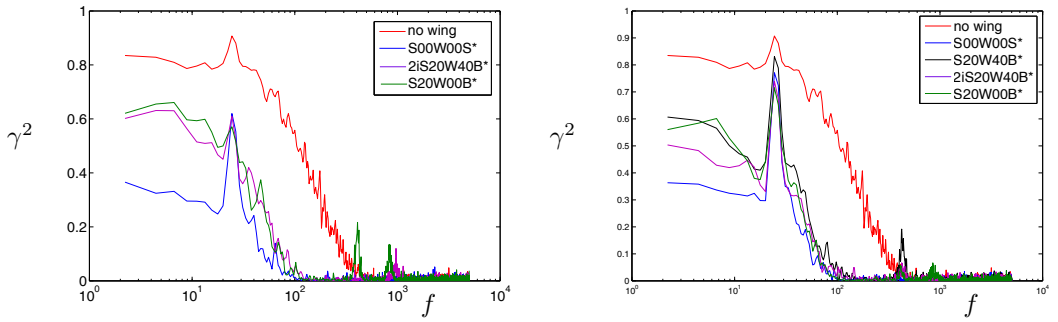
Figure 5.7: 45deg protocol: PSD for all TEs, $\tilde{z}/W = 0$

trailing edges with the reference probe located in a trough at $\tilde{z}/W = 0$. For both zero and $4°$ incidence, the corresponding values measured without the wing are also displayed for reference. Although the difference is not pronounced, both with and without incidence, the serrated trailing edges show lower coherence values at 25 Hz over larger separations ($\tilde{z}/W \geq 1/4$) than for the base wing. This shows that despite having relatively little impact on broadband coherence in this case, the potential for reduction at the peak frequency is still interesting. *N.B.:* the curve is not plotted for $S20W40B^*$ at zero incidence due to a corrupted data file.

5.2.3 Gaussian protocol

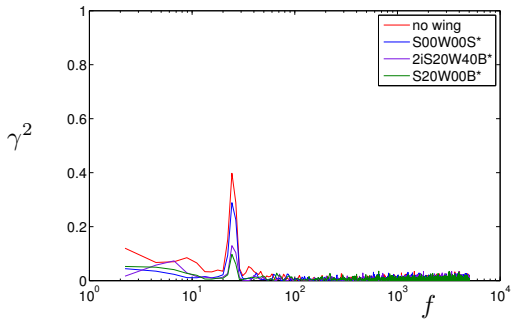
To target flows with specific statistics, Gaussian and intermittent flows were generated with the active grid, as detailed in section 2.3.1. Due to the duration of the protocol relative to the sampling time, only a relatively short part could be measured with the hot wires, and therefore only the Gaussian one is presented in this section.

Fig. 5.10 shows the PSD and coherence measured with the Gaussian protocol, without the wing. The spectra do not exhibit any peak and are rather similar, except for sightly higher low frequency values close to $\tilde{z}/W = 0$. At small separations, the coherence shows high values at low frequency and a broadband component, both dropping fast when the separation is increased. The low frequency coherence seems however to increase again after $\tilde{z}/W = 1$, which is not observed in other protocols. A potential explanation would have been the periodicity of the active grid flap, but the scales do not match. It is however worth noting that this span-wise inhomogeneity can also be noticed in the PSDs, plotted in fig. 5.10a.

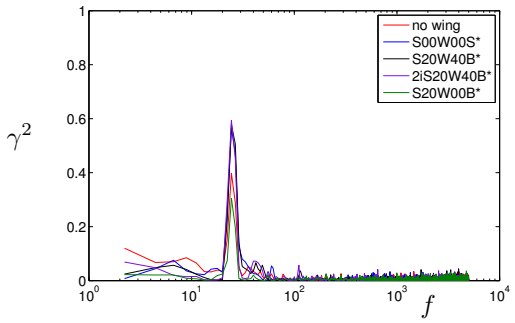


(a) $AoA = 0°$, $\tilde{z}/W = 1/8$

(b) $AoA = 4°$, $\tilde{z}/W = 1/8$



(c) $AoA = 0°$, $\tilde{z}/W = 1$

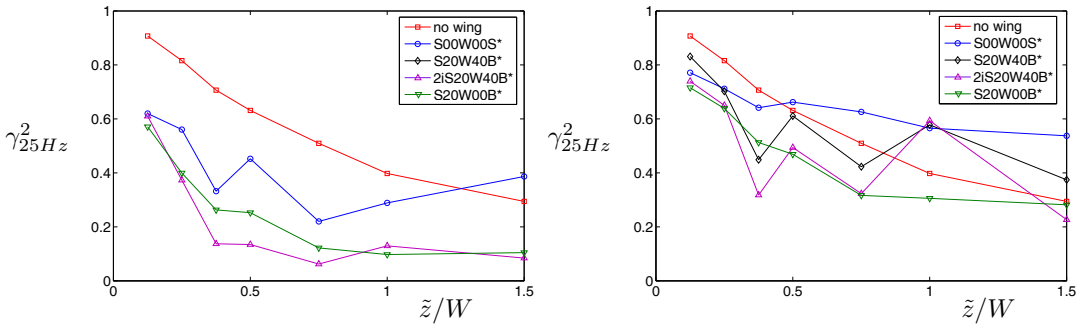


(d) $AoA = 4°$, $\tilde{z}/W = 1$

Figure 5.8: 45deg protocol: γ^2 for all TEs.

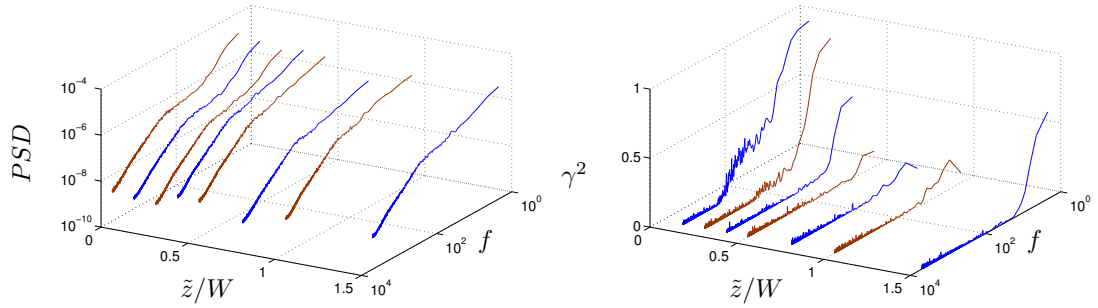
Fig. 5.11a-5.11c show the coherence at $\tilde{z}/W = 1/8$ and various incidences for the base wing subjected to the Gaussian protocol. Comparison with fig. 5.10b highlights how the introduction of the base wing at zero incidence further reduces the already low coherence. However, when increasing the geometric angle of attack, a broadband component of coherence appears: as previously mentioned the pitch angle then gets closer to its stall value, and the protocol's gusts can therefore temporarily make the wing go into stall conditions, thus exhibiting more broadband flow dynamics. Fig. 5.11d shows that both low frequency and broadband coherence increase with incidence, until the geometric angle of attack approaches the stall value for unsteady inflow conditions.

Fig. 5.12 shows that at zero geometric incidence, $S20W00B^*$ exhibits the lowest levels of broadband coherence but has the highest value of coherence at the expected shedding frequency. The base wing has



(a) $AoA = 0°$, $\tilde{z}/W = 1/8$ (b) $AoA = 4°$, $\tilde{z}/W = 1/8$

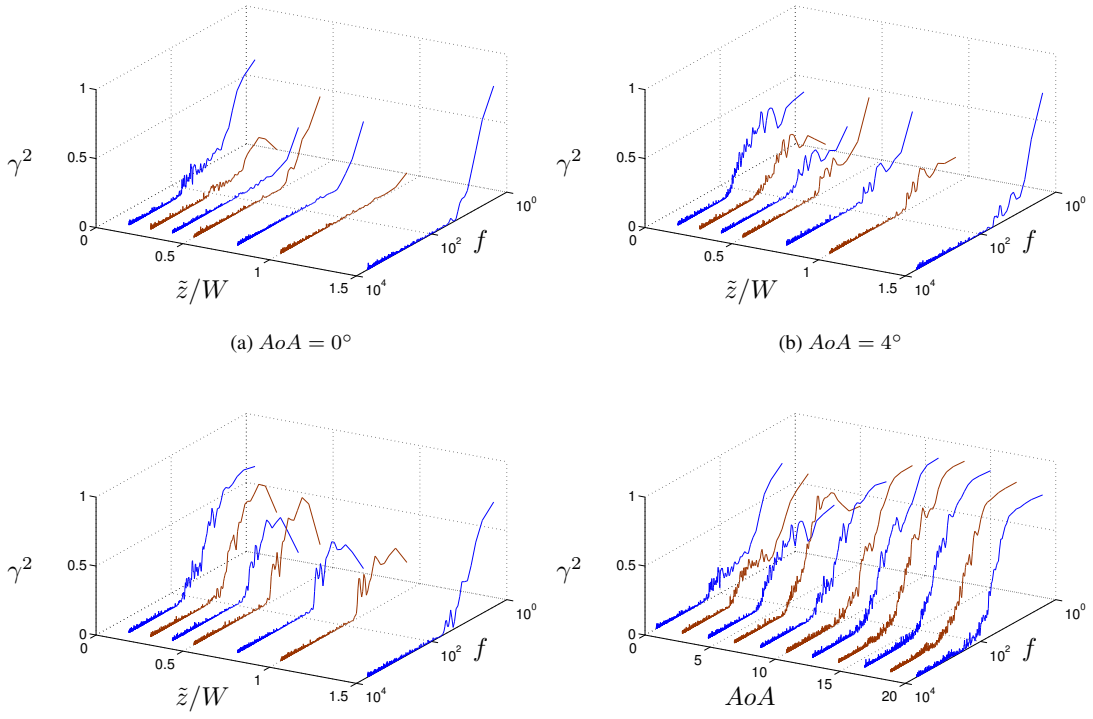
Figure 5.9: 45deg protocol: γ^2_{25Hz}



(a) PSD (b) γ^2

Figure 5.10: Gaussian protocol: PSD and coherence without wing. Alternated colours for ease of visualisation.

the strongest overall reduction of coherence compared to the protocol without the wing, since its broadband reduction is close to $S20W00B^*$'s but it does not exhibit a shedding spike. On the contrary, when putting the wing at incidence, the serrated trailing edges exhibit lower coherence than the base wing and the 2-iteration multi-scale TE seems to have the strongest overall effect. Indeed it has a lower broadband coherence than the base wing and the sinusoidal TE and is comparable to the straight blunt case. At the shedding frequency, $\gamma^2 = 0.18$ for 2-iteration compared to 0.15 for the blunt case, but the latter also has a spike at the harmonic. This overall performance is backed by the spectra plotted in fig. 5.13, which shows higher values for $S20W00B^*$. $S20W40B^*$ has lower energy content than $2iS20W40B^*$ but its effect on



(a) $AoA = 0°$

(b) $AoA = 4°$

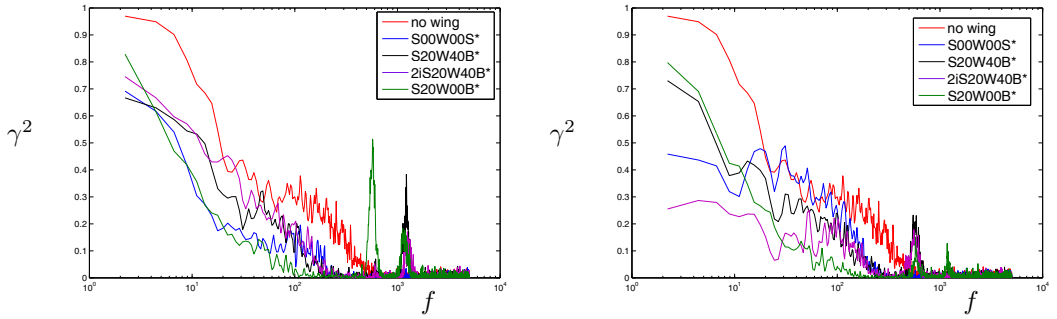
(c) $AoA = 8°$

(d) All AoA, $\tilde{z}/W = 1/8$

Figure 5.11: Gaussian protocol: γ^2 downstream of $S00W00S^*$. Alternated colours for ease of visualisation.

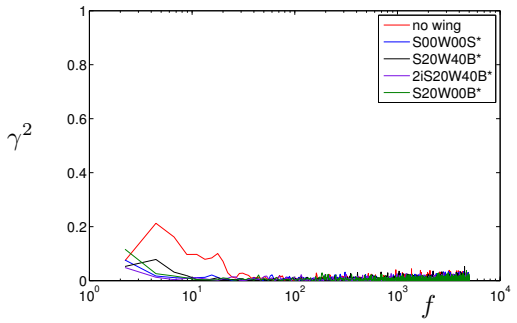
coherence is lesser. Fig. 5.12, one notices that apart from very low frequencies no coherence is measured between the two troughs. The values measured at low frequencies are much lower than in the case of the sinusoidal protocol, which is partly explained by the less structured inflow sent onto the airfoils.

N.B.: at $AoA = 0°$, the symmetry of the set-up with regards to the orientation of the hot-wires should shift the shedding peaks to the harmonics, which is the case for the serrated trailing edges but not for the straight blunt one. As previously mentioned, a possible explanation would be 3-D instabilities generated over the span of the blunt edges; however, further investigation is required to draw a conclusion on that matter.

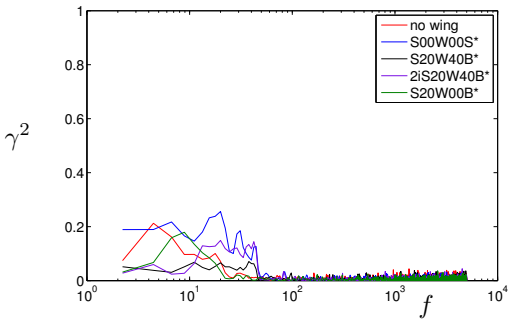


(a) $AoA = 0°$,$\tilde{z}/W = 1/8$

(b) $AoA = 4°$,$\tilde{z}/W = 1/8$



(c) $AoA = 0°$,$\tilde{z}/W = 1$



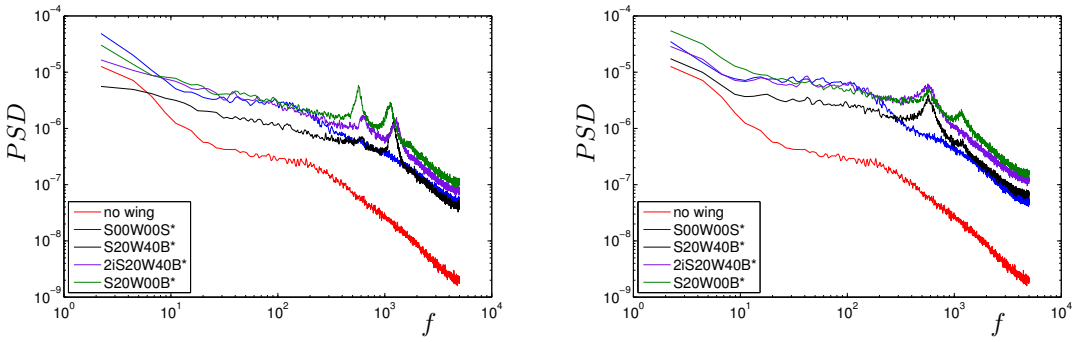
(d) $AoA = 4°$,$\tilde{z}/W = 1$

Figure 5.12: Gaussian protocol: γ^2 for all TEs.

5.2.4 Intermediate conclusions

For all protocols, the effect of the serrated trailing edges on incoming coherence is stronger when the wing is put at incidence. This can be explained by the generation of a strong cross flow (peak to trough) in the wake of the serrations as reported in the previous chapters.

With the sinusoidal and Gaussian protocols, when at incidence, the coherence levels are lower for 2-iteration TE than the unmodified wing. However, it is found that for the 45deg protocol, the base wing reduces incoming broadband coherence more than the serrated TEs; the opposite trend being observed at the main frequency of the protocol. It is important to note that the sinusoidal protocol creates coherence over a large span-wise extent, in contrast to the Gaussian one that sees coherence dropping after $\tilde{z}/W = 0.5$. This highlights the potential effect of modulated TEs to affect coherence over large scales down to the order of



(a) $AoA = 0°$, $\tilde{z}/W = 1/8$ (b) $AoA = 4°$, $\tilde{z}/W = 1/8$

Figure 5.13: Gaussian protocol: PSD for all TEs, $\tilde{z}/W = 0$

their patterns' wavelength.

At this point, the reason why 45deg protocol has lower broadband coherence for the base wing still needs to be explained.

5.3 Discussion on vertical asymmetry of the shedding mechanism

The results presented in the previous section display a signature of the blunt trailing edges' vortex shedding, by a peak and its harmonics in both the spectra and the coherence visible for most cases. It is interesting to note that the frequency of this vortex shedding does not appear to change with the incidence. Rather, the peak in the spectra becomes more broadband when getting closer to stall conditions while the dominant frequency remains around its initial value.

With higher incidence, the velocity on the suction surface increases and this should tend to change the vortex shedding frequency. The observation of a constant vortex shedding frequency therefore leads to the idea that the phenomena is mainly driven by the pressure side, less sensitive to the incidence. In fact, this corroborates the discussion from section. 4.2.1, where it was pointed out that only the displacement thickness of the pressure side boundary layer could be used for the definition of the Strouhal number.

The vortex shedding mechanism would therefore involve the detachment of vortices mainly from the pressure surface, which would constrain the shedding frequency, as sketched in fig. 5.14. In the extreme situation where the wing would be placed almost normal to the flow, the mechanism is expected to be

similar to that of a cross-stream plate, shedding from its edges.

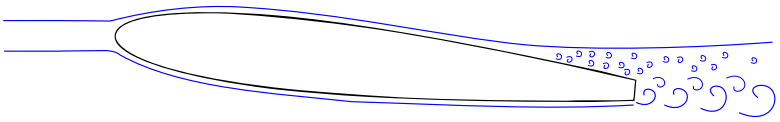


Figure 5.14: Sketch of the shedding mechanism at a blunt trailing edge.

This representation of the mechanism would also explain the vertical asymmetry of the shedding intensity observed in the vertical maps of spectra behind the troughs of blunt trailing edges, such as seen in fig. 3.4.

5.4 Force measurements

As mentioned in the section 1.2.6, a great interest in using an active grid is the ability to test airfoil or wind turbines in unsteady inflow conditions. The unsteadiness of the inflow can translate into unsteadiness of the forces applied to the airfoil, which in the case of wind turbines load can accelerate structural fatigue. Given that lift is higher than drag at moderate pitch angles and that it induces the load of a wind turbine, previous studies [19, 37, 22] have focused on its statistics. The present work therefore follows the same approach and focuses on the lift of an airfoil, subjected to three different inflows. An intermittent and a Gaussian protocol are used to study the statistics of the lift with different inflow statistics, and its evolution with incidence. A sinusoidal variation of the flow incidence is also used to complement this study with a comparison of the lift output for a more simple and periodic variation of the inflow conditions.

5.4.1 Gaussian inflow

Fig. 5.15 shows the mean, corrected for the initial set-up offset, and standard deviation of lift for four airfoils under Gaussian inflow. All airfoils follow the same trend with a stall around 10° incidence, after which the mean lift slowly decreases and the standard deviation of the lift, due to the incoming unsteady flow, increases. The difference of maximum lift values represents a 6% variation, with the unmodified wing having the highest value and $S20W00B^*$ the lowest. This is indeed expected as blunt wings increase the lift coefficient and not the maximum value of lift. It appears that both serrated airfoils have similar values up until the stall, after which the sinusoidal one maintains higher mean values. However, mean and

standard deviation of the lift fluctuations are not enough to characterise the impact of the serrations, as further consideration of distribution of lift fluctuations can be key for both power output stability and load fatigue.

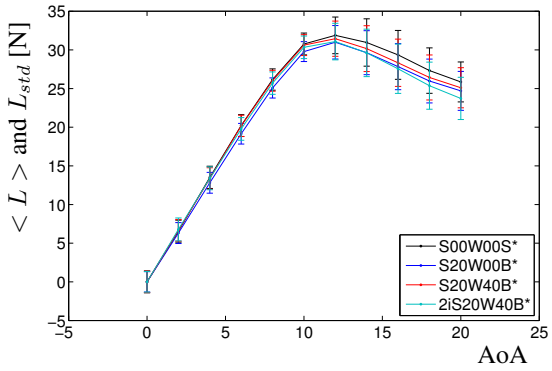
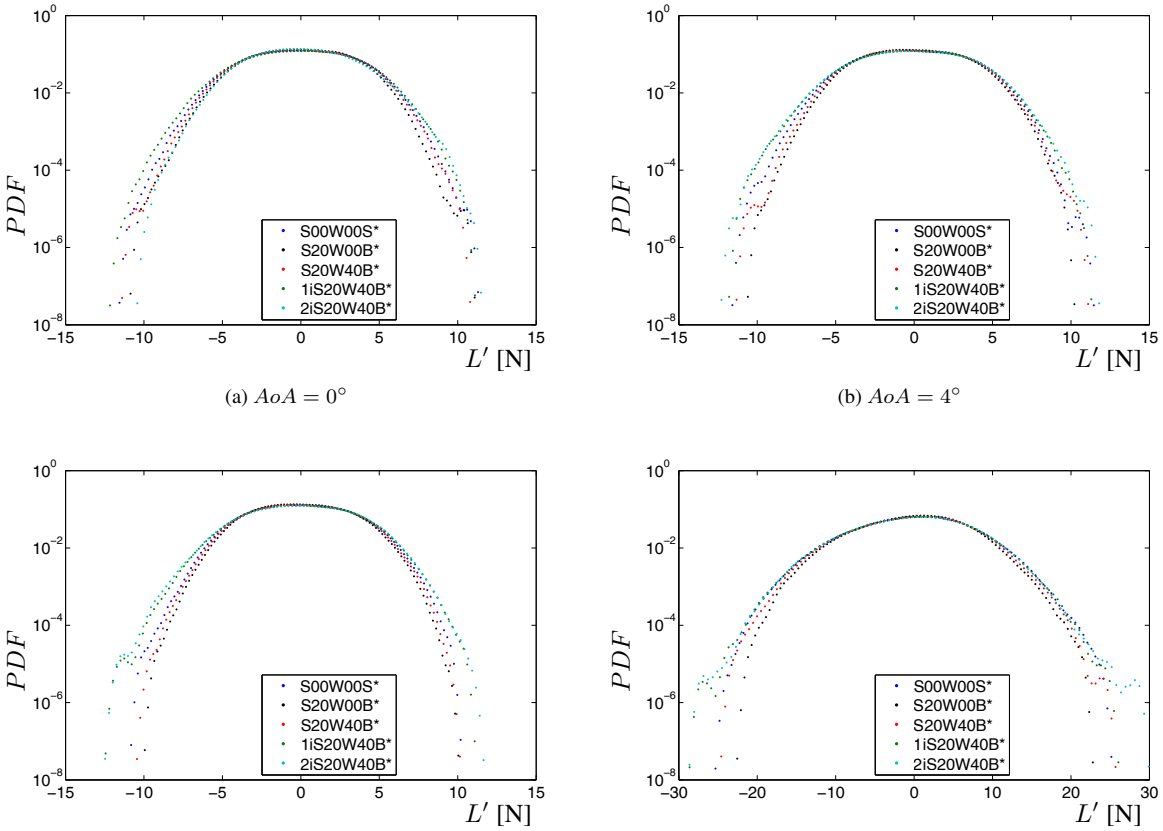


Figure 5.15: Lift curve and standard deviation, for four trailing edges, with Gaussian inflow.

Fig. 5.16 shows the Probability Density Function (PDF) of the lift fluctuations for the five tested trailing edges, under Gaussian inflow conditions at four pitch angles. The four pitches correspond to zero incidence, moderate incidence ($4°$), pre-stall ($8°$) and post-stall ($14°$). At zero incidence, it is noticeable that all wings have similar PDF values up to around $5\,$N, after which differences arise. The $S20W00B^*$ then seems to reduce the probability of large fluctuations the most. For positive fluctuations, $S20W40B^*$ and $S00W00S^*$ have very similar values, higher than those of $S20W00B^*$ and lower than those of $1iS20W40B^*$ and $2iS20W40B^*$. For negative fluctuations, the same trend is observed, except for $2iS20W40B^*$ which displays the lowest value.

At $4°$ and $8°$, $S20W00B^*$ still has the lowest values of lift fluctuations' PDF and the two multiscale trailing edges exhibit the highest ones, close to each other, around two decades higher than $S20W00B^*$ for $10\,$N fluctuations. $S20W40B^*$ and $S00W00S^*$ sit in-between those extrema, with the former having lower values overall.

In post-stall conditions, at $14°$, the values of the amplitude of lift fluctuations drastically change, and now extend up to $20-30\,$N. Within $\pm25\,$N, the unmodified wing now has the highest values along with the multiscale serrations. $S20W00B^*$ has the lowest values, although within $\pm25\,$N, the difference is less than a decade at its highest. $S20W40B^*$ has intermediary values. It must be noted though, that the multiscale



(a) $AoA = 0°$ (b) $AoA = 4°$

(c) $AoA = 8°$ (d) $AoA = 14°$

Figure 5.16: PDF of lift fluctuations for all five wings at four pitch angles (Gaussian inflow).

TEs exhibit heavy tails further than $\pm 25\,\mathrm{N}$.

Overall, the serrations, and in particular the multiscale ones, seem to increase the PDF of larger fluctuations under Gaussian inflow, while the straight blunt wing has the strongest reduction of those fluctuations. This would imply more extreme values of the load if applied to wind turbine and could be detrimental to structural fatigue and power output stability. However, atmospheric flows often are intermittent, which are the type of inflows studied in the next section.

5.4.2 Intermittent inflow

Fig. 5.17 shows the mean and standard deviation of lift for four airfoils under intermittent inflow. Contrary to the Gaussian protocol, the maximum lift value is obtained with $S20W00B^*$, that maintain the highest values for stall and post-tall conditions. The unmodified wing exhibits the most abrupt stall, while $S20W40B^*$ has a slow stall behaviour. In that case, $2iS20W00B^*$ seems to offer the best results of the two serrated airfoils, as it reaches a higher maximum value and exhibits a slow decay of mean lift in post-stall. However, as for the previous protocol, the mean and standard deviation values are not enough to describe the effect of the trailing edge patterns on the lift, and the focus should be on the fluctuations.

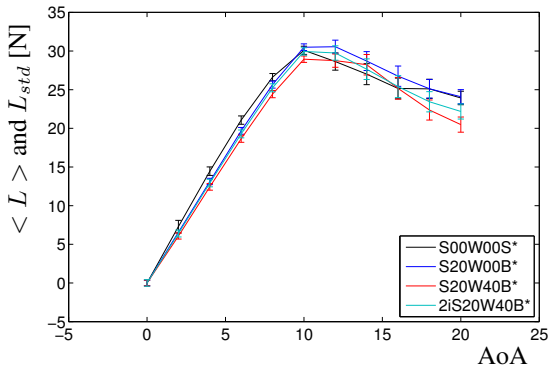
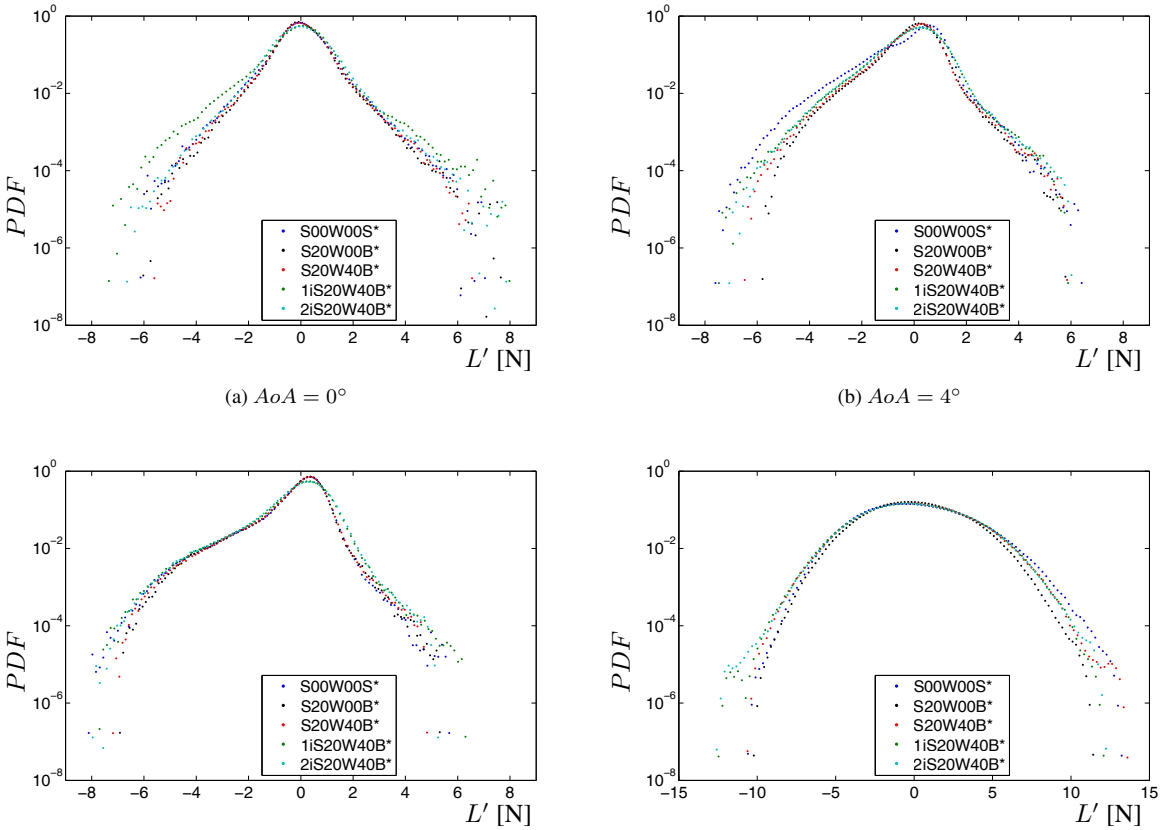


Figure 5.17: Lift curve and standard deviation, for four trailing edges, with intermittent inflow.

Fig. 5.18 shows the PDF of the lift fluctuations for the five tested trailing edges, under intermittent inflow conditions at four pitch angles. Contrary to the results from the Gaussian inflow, there is a clear change in the aspect of the PDFs when varying the pitch angle. At zero incidence, the PDF are almost symmetric and no clear trend is discernible, apart from $1iS20W40B^*$ having heavier tails, and $S20W00B^*$ having lower values, but without a clear separation.

At $4°$, the shape of the PDF changes and values are higher for the negative fluctuations. The unmodified wing has the heaviest negative tails, while the straight blunt one has again the lowest values and all three serrated ones are close to each other, in between the previous two. When increasing the incidence, at $8°$, the PDF curves get narrower, except for the two multiscale ones that exhibit the same shape as previously and therefore have higher values in the positive fluctuations. A narrower PDF implies that fluctuations around the mean value are more likely to be small. Therefore, $1iS20W40B^*$ and $2iS20W40B^*$ exhibit larger

positive lift fluctuations.



(a) $AoA = 0°$

(b) $AoA = 4°$

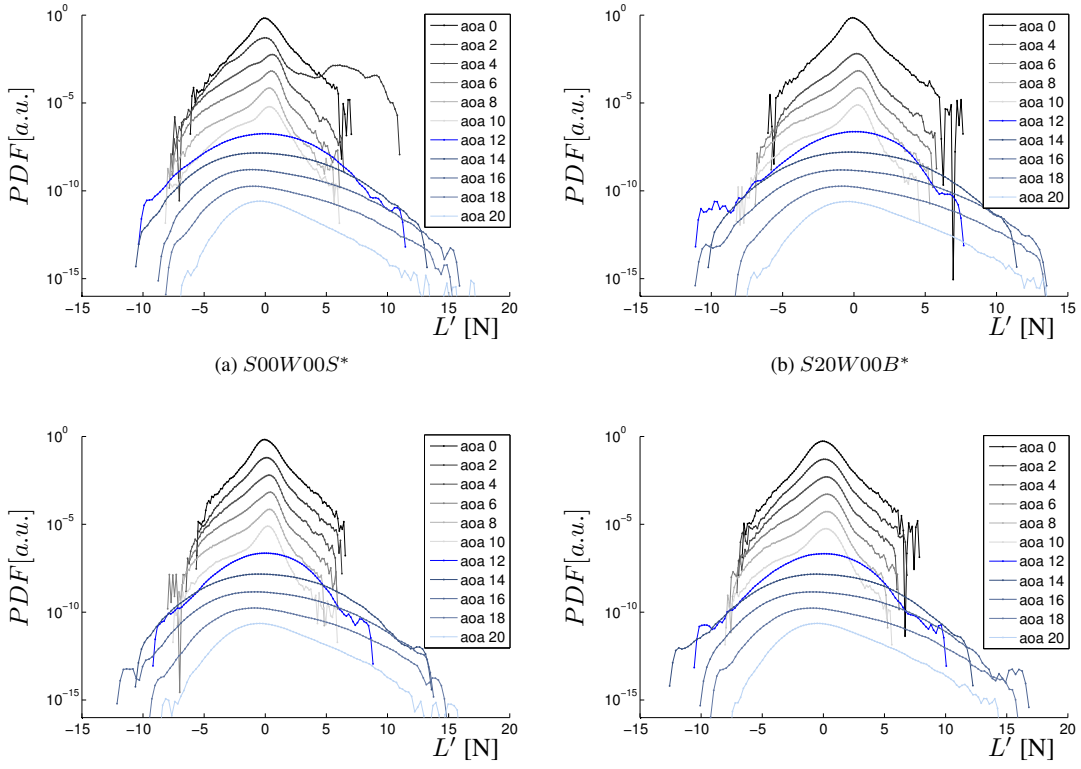
(c) $AoA = 8°$

(d) $AoA = 14°$

Figure 5.18: PDF of lift fluctuations for all five wings at four pitch angles (intermittent inflow).

Post-stall, at $14°$, the aspect of the PDF has clearly changed again, and becomes very similar to that of the Gaussian inflow case. It is clear that $S20W00B^*$ has overall the lowest values, followed by $S20W40B^*$ and then $1iS20W40B^*$ and $2iS20W40B^*$ close together. $S00W00S^*$ displays asymmetry, as it has similar values to that of $S20W00B^*$ for negative fluctuations, but the highest for positive fluctuations. Two parameters contribute to the variations of lift: the variation of incidence and the variation of total velocity. Assuming that an increased flow incidence induced by the flap is linked to a reduced stream-wise velocity, that is $\overline{u'w'} < 0$, the following can be inferred: post-stall, a positive fluctuation means tending towards

smaller angles of attack, while a negative fluctuation means going deeper into stall with a larger angle of attack. The unmodified wing appears to be stronger at limiting fluctuations that push into deeper stall, than those getting closer to the stall onset.



(a) $S00W00S^*$ (b) $S20W00B^*$

(c) $S20W40B^*$ (d) $2iS00W40B^*$

Figure 5.19: PDF, shifted for clarity, of lift fluctuations for four trailing edges at all tested pitch angles (intermittent inflow).

Given the strong variations of the PDF shape with the incidence, observed for the intermittent inflow conditions, fig. 5.19 shows, for four tested trailing edges, the PDF of lift fluctuations over the full range of pitch angles. Overall, the four wings exhibit a very similar trend. In pre-stall conditions (shades of grey), the skewed PDFs tend to be narrower until $10°$ incidence, with higher values for the negative fluctuations. Starting at $12°$, the post-stall conditions (shades of blue) first exhibit almost symmetric shapes resembling

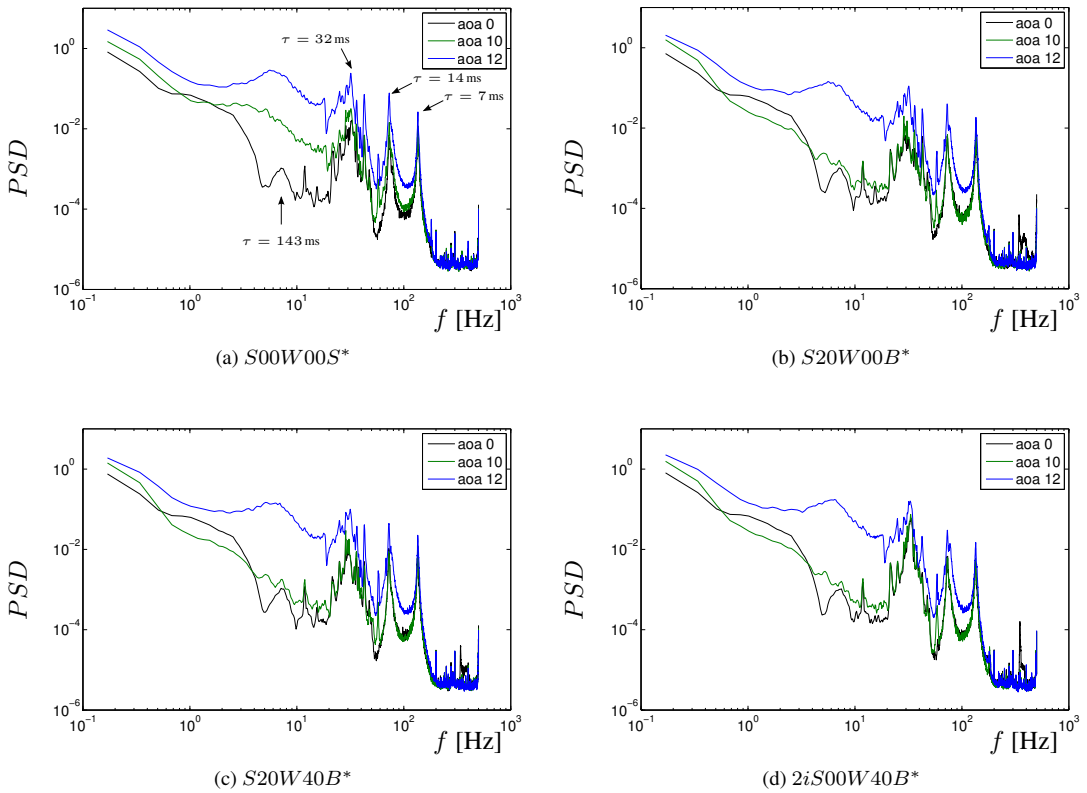
the distribution of the Gaussian protocol, that gets skewed when increasing the incidence again. In that case, positive fluctuations have the highest values. As discussed before, positive fluctuations in post-stall correspond to a decrease in the angle of attack, which is equivalent to negative fluctuations in pre-stall conditions. Therefore, both pre- and post-stall conditions show that the four wings tend to exhibit lift fluctuations that correspond to the reduction of the angle of attack. Although to a lesser extent, one can also notice a change in the pre- and post-stall behaviour of the previously Gaussian protocol, where fig. 5.16 displays an inversion of the skewness between the three initial pitch angle and the post-stall one.

Although the PDF shapes are similar for all tested wings, a few differences are worth noticing in fig. 5.19. Immediately after stall, at $12°$, both serrated trailing edges have narrower PDFs than the straight trailing edges, the difference being most noticeable between $S20W40B^*$ and $S00W00S^*$. At $10°$, it appears that $S20W40B^*$ also has the narrowest PDFs. As mentioned before, this means that the fluctuations will tend to be closer to the mean value, which is potentially interesting in terms of structural load fatigue. This implies that around stall conditions, the serrated trailing edges reduce the fluctuations more than the straight blunt one ($S20W00B^*$). However, as noted before, $S20W00B^*$ exhibit stronger overall reduction away from the stall on-set. The secondary peak around $6 - 12$ N observed for $S00W00S^*$ at $2°$ incidence is attributed to an error in the data acquisition rather than a physical phenomena.

So far, the results have been discussed in terms of the PDF of the lift fluctuation, which gives an overview of the range of values reached during the measurements but does not provide dynamical information. Given that some behaviour remains as yet un-explained and that variations of the inflow are expected to give rise to unsteady aerodynamics, it is worth looking into more dynamical aspect of the data.

Fig. 5.20 shows the Power Spectral Density (PSD) of the lift fluctuations, for four tested trailing edges, at three pitch angles: zero incidence, and pre and post-stall where the change of the PDF shape was the most noticeable. It is worth reminding that lift was acquired at 1 KHz, therefore resolving up to 500 Hz and that the main body of the wing was milled out of aluminium to ensure a high stiffness. The wing itself, irrespective of serrations, acts as a low-pass filter on the lift output, so the higher frequencies are not expected to be of great interest.

The spectra are very similar between the different trailing edges, and only a band around $4 - 20$ Hz observed at $10°$ incidence sets $S00W00S^*$ apart from the other cases. To look into the dynamics of lift, the increment PDF of the lift fluctuations can be based on these spectra. In fact, the increment PDF for a given time-scale τ is the PDF of the values $(L(t+\tau) - L(t))$ [39]. It represents the distribution of steps in lift values with a given time separation and is therefore an indication of the unsteadiness of the signal. The



(a) $S00W00S^*$ (b) $S20W00B^*$

(c) $S20W40B^*$ (d) $2iS00W40B^*$

Figure 5.20: PSD of lift fluctuations for four trailing edges at three pitch angles (intermittent inflow).

value of τ is thus chosen based on the frequencies that appear significant in the lift spectra.

Since the strongest variations of PDF are observed between $10°$ and $12°$, fig. 5.21 shows the increment PDFs of four wings at $10°$ and $12°$ pitch angles, at a number of time-scales selected from fig. 5.20a.

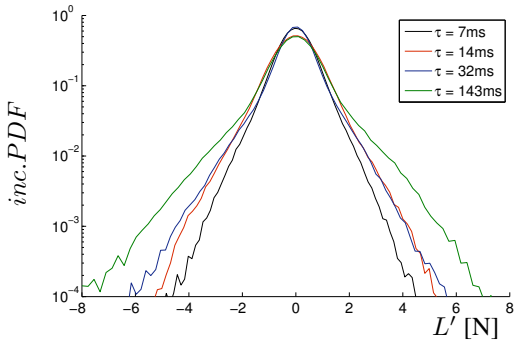
While all wings exhibit similar spectra, there are a number of differences in the incremental PDFs that are noticeable. First, $S00W00S^*$ has been observed to have a larger broadband component in the spectra at $10°$ around $4 - 20\,\mathrm{Hz}$, and when looking at $\tau = 143\,\mathrm{ms}$ (fig. 5.21a), its tails are indeed higher than for those of the other trailing edges.

Staying at $10°$ incidence, the three modified wings have narrower incremental PDF at the four investigated time-scales, with $S20W00B^*$ and $S20W40B^*$ being very similar. $2iS20W40B^*$ has larger

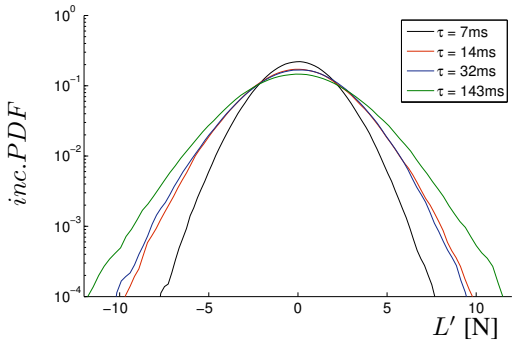
incremental PDF than $S20W40B^*$ for three of the four time-scales.

At a higher incidence, 12°, all incremental PDF are wider as expected from the pre/post-stall comparison previously discussed. In that case, $S20W00B^*$, $S20W40B^*$ and $2iS20W40B^*$ have very similar values, while $S00W00S^*$ has wider incremental PDFs, for all four time-scales.

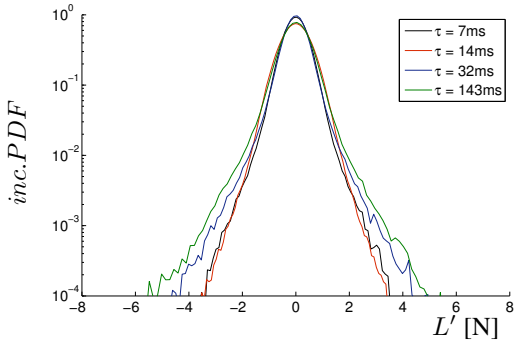
Given that these incremental PDFs represent the distribution of the variations of lift over a given time separation, their implication in terms of load fluctuation is even higher than that of standard PDFs. In that sense, the serrated wings appear to be of particular interest, especially $S20W40B^*$ which exhibits the lowest values overall.



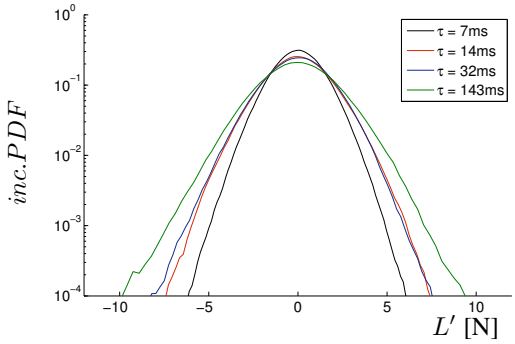
(a) $S00W00S^*$ AoA 10°



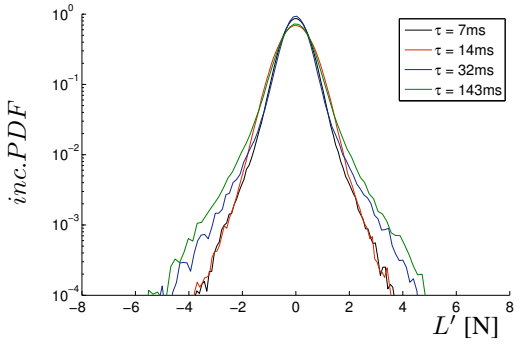
(b) $S00W00S^*$ AoA 12°



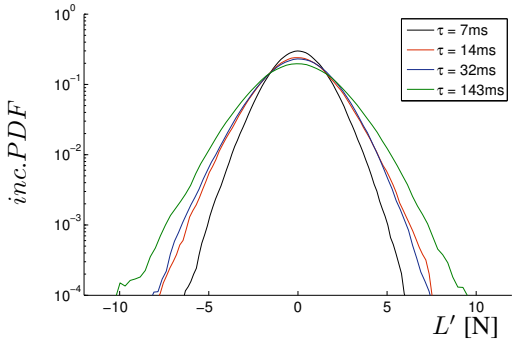
(c) $S20W00B^*$ AoA 10°



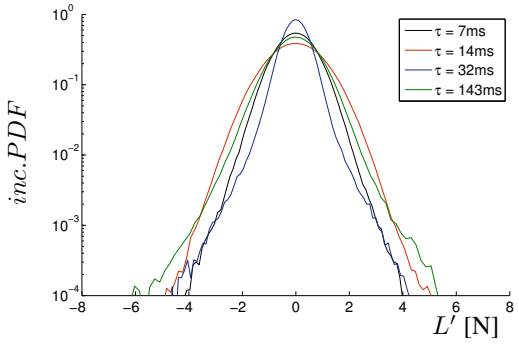
(d) $S20W00B^*$ AoA 12°



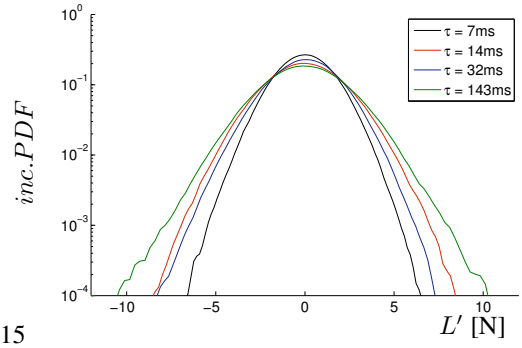
(e) $S20W40B^*$ AoA 10°



(f) $S20W40B^*$ AoA 12°



(g) $2iS20W40B^*$ AoA 10°

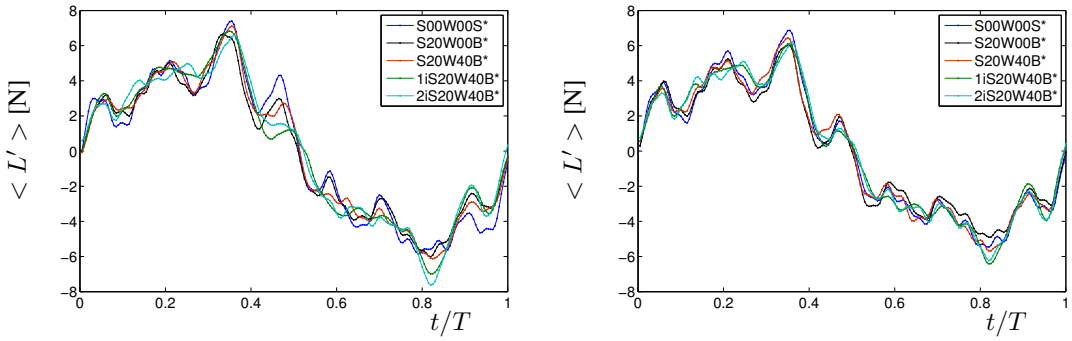


(h) $2iS20W40B^*$ AoA 12°

Figure 5.21: Incremental PDF for four wings at two pitch angles (intermittent inflow).

5.4.3 Sinusoidal inflow

Fig. 5.22 shows the lift fluctuations of five tested wings subjected to sinusoidal inflow conditions, phase averaged over one period of the protocol, at two pitch angles. The results are similar to those from the study by Cordes *et al.* [19], illustrated in fig. 2.10b, in the sense that a sinusoidal trend is visible, with a high content of higher frequencies adding peaks and small variations. Here, the main interest is to compare the response of the different wings, and although they follow the same trend over the period, some differences arise. At 4° incidence, the serrated trailing edges appear to smooth the time variations observed for the unmodified case. The effect seems stronger for the multiscale ones, which apart from a peak around $t/T = 0.82$, reduce most of the peaks over the protocol period. At 8° incidence, the effect is less clear, but the same trend is observed, with the multiscale serrated trailing edges smoothing the time variations of the lift fluctuations.



(a) $AoA = 4^\circ$ (b) $AoA = 8^\circ$

Figure 5.22: Phase-averaged lift fluctuations under sinusoidal inflow conditions.

It must be noted that the value measured here is inherently integrated across the whole span of the wing, since the lift is directly measured as a force and not estimated from flow data. Due to possible de-phasing of the variation of the flow incidence across the wind tunnel section, any discussion of the aerodynamics responsible for this observation would be somewhat speculative and would require further characterisation of the flow around the wing. It is nonetheless encouraging to note the trend observed for the multiscale serrations, that could be of significant interest in terms of load fluctuations, for cases where the airfoil is submitted to variations of the flow incidence, such as a wind turbine blade subject to atmospheric turbulence.

5.5 Discussion and concluding remarks

For all protocols, the effect of the serrated trailing edges on incoming coherence is stronger when the wing is put at incidence. This can be explained by the generation of the cross flow (peak to trough) in the wake of the serrations. With the sinusoidal and Gaussian protocols, when at incidence, the coherence levels are lower for a 2-iteration serrated TE than the unmodified wing. However, it is found that for the "45deg" protocol, the unmodified wing reduces incoming coherence more than the serrated TEs.

The study of lift statistics has shown that the airfoil's load is sensitive to the statistics of the inflow. An intermittent inflow shows the highest sensitivity to pitch angle with a clear variation of the shape of the probability density function (PDF) of lift fluctuations. Indeed, the transition between pre- and post-stall is abrupt. While the effect of the trailing edge serration patterns seems limited on the load statistics, sinusoidal serrations display a narrower PDF of lift fluctuations in both pre- and post-stall conditions, compared to the unmodified wing (the difference with the multiscale patterns is lesser).

An experiment with a sinusoidal variation of the flow incidence has shown that wings with serrated trailing edges, and in particular multiscale patterns, tend to damp unsteady fluctuations in lift over an inflow period.

For the hot-wire data and even more so for the lift statistics, the discussion of results has often been limited to the comparison of salient quantities between wings with different trailing edges. This is due to the complexity of the inflow which renders the discussion of specific aerodynamic phenomena more complicated.

Chapter 6

Conclusions and future work

Following on from previous studies, chapter 1 has presented the three main goals of the present thesis. The following gives a summary of the main outcomes of the thesis for each of them. Naturally, although a number of questions have been answered, many more have been asked; an outline of future works to tackle these challenges is then given.

Offering a better understanding of how cut-in sinusoidal trailing edge serrations affect the flow around them and in the wake.

The cut-in approach for the trailing edges of a lifting wing generates a flow from below the peaks towards the troughs. Such a flow pattern increases the velocity deficit behind the peaks while re-energising the wake behind the troughs. Therefore, span-wise inhomogeneity of the velocity deficit and wake width is observed and persists far downstream, particularly for the wake width.

Span-wise inhomogeneity is also observed in spectral analysis, where the shedding signature slowly spreads out, in the span-wise direction from the troughs. Downstream evolution of the shedding intensity shows that the shedding signature disappears from the spectra before span-wise homogeneity is reached.

Vortex shedding is found to be locked into cell structures behind the cut-in serrations. In turn, span-wise coherence is mostly seen at the shedding frequency and is greatly reduced by the sinusoidal patterns compared to the blunt straight one. This reduction, however, comes at the price of an increase in low frequency coherence. The cell structures are bent and can be reversed (for the large wavelength) by the span-wise inhomogeneity of the stream-wise velocity. The lack of coherence and correlation between ad-

jacent cells and the existence of distinct modes for each of them shows that the shedding is independent between neighbouring serrations.

Devising ways of mitigating drawbacks induced by the disruption of the flow.

Two separate approaches were investigated in an effort to modify the previously observed vortex shedding cell structures and the associated span-wise coherence in the wake of a wing with a cut-in sinusoidal trailing edge. The first one is to introduce multiscale patterns to promote flow mixing in the trough and break down the cellular structure of the wake. The second is to maintain sharpness at the trailing edge by modulating the aft part of the wing, rather than just cutting into the trailing edge.

Cell structures are observed in the case of multiscale TEs, via a study of de-phasing and Optimal Mode Decomposition. However, they are weaker than in the single tone cases. By weakening the cell structures, the use of multiscale patterns leads to a strong decrease of vortex shedding energy and associated coherence. It is also observed that the low frequency coherence introduced near the troughs of the single tone sinusoidal TEs is further decreased, by 8% for the 1-iteration multiscale TE and by 57% for the 2-iteration one.. The introduction of a sharp sinusoidal trailing edge removes the shedding signal measured in the wake behind the trough, and replaces it with a broadband equivalent. At large scales, the span-wise coherence on the edges of the wake is less affected than for a blunt trailing edge, however, no coherence attributed to shedding phenomena is measured. OMD in the wake of such trailing edges reaches its limitations and cannot pick-up a clear cell structure.

In short, the introduction of cut-in serrations exhibits bluntness that in turn generates vortex shedding that locks into a bent cell structure. This shedding is, however, weaker than that of a straight trailing edge of the same maximal bluntness. The use of multiscale patterns weakens the cell structures which translates into a reduction of vortex shedding intensity as well as a reduction of span-wise correlation at both vortex shedding and low frequencies. The use of an alternative sharp approach is a compromise that gives less coherence reduction on the edges of the wake but avoids the introduction of a clear vortex shedding signal.

Studying how such flow disruption would affect the behaviour of serrated wings under unsteady inflow conditions.

An investigation was conducted using an active grid to tailor the inflow conditions to which the wing was subjected. Both hot-wire measurements in the wake and lift measurement on the wing were performed, to

study span-wise coherence and energy spectra as well as studying the lift statistics.

For all active grid excitation protocols, the effect of the serrated trailing edges on incoming coherence is stronger when the wing is at incidence. This can be explained by the generation of the periodic cross flow (trough to peak) in the wake of the serrations. The 2-iteration multiscale trailing edge is found to best reduce the coherence, for Gaussian and sinusoidal protocols. In the particular case of the bluff-body-like protocol, the unmodified wing has stronger broadband reduction than the others, although the multiscale one exhibits stronger reduction at the targeted frequency of bluff-body-like oscillations.

The study of lift statistics shows that the wing's load is sensitive to the statistics of the inflow. An intermittent inflow shows the highest sensitivity to pitch angle with a clear variation of the shape of the probability density function (PDF) of lift fluctuations. Indeed, these fluctuations are observed to be strongly skewed before stall, while a more symmetric and wider distribution is observed in close post-stall conditions. While the effect of the trailing edge serration patterns seems limited on the load statistics, sinusoidal serrations display a narrower PDF of lift fluctuations in both pre- and post-stall conditions, compared to the unmodified wing (the difference with the multiscale patterns is lesser). This would be of interest for applications where the standard operating conditions are close to stall.

For the hot-wire data and even more so for the lift statistics, the discussion of results has often been limited to comparison of output between the trailing edges. This is due to the complexity of the inflow which renders the discussion of a particular aerodynamics phenomena more complicated. To extend the discussion and to be able to associate some observed variation in e.g. lift statistics, further characterisation of the inflow would highly desirable.

The vortex shedding mechanism at the troughs of the serrations was observed to be vertically asymmetric, with a stronger contribution of the pressure side than of the suction side.

Based on the conclusions drawn from this thesis, a number of studies can be recommended for future work, in order to address the new questions that have been raised.

- The sharp trailing edge approach was presented to allow for a cut-in serration method while maintaining sharpness in the trough. However, due to experimental constraints, only the aft part of the wing was modulated, which inherently creates a steep trailing edge in the trough, and although this part is sharp, it can be perceived as somewhat blunt by the shear layers. Therefore, it is recommended to investigate the near wake of a wing with a sinusoidal modulation of its trailing edge affecting the entire chord. Such a wing would have an unmodified NACA0012 section at the peak and a compressed

profile at the trough, with the same thickness and therefore not a NACA0012 section anymore. To avoid span-wise variation of the point of maximum thickness, an alternative would be to only extend the aft part that is modulated, without covering the entire chord.

- The original acoustic study by Chong *et al.* [14] had highlighted the interest of cut-in serrations in terms of broadband noise reduction but stated that the additional tonal noise due to vortex shedding was a main limitation. Given that the multiscale and sharp trailing edge serrations gave interesting results in terms of vortex shedding reduction while maintaining a cut-in serration approach, it would be interesting to conduct an acoustic study on such geometries. The potential tonal noise reduction should be studied and checked against the overall broadband noise level to ascertain whether there is an overall benefit.

- In addition to the study of airfoil self-noise, interaction noise is of interest, as it is relevant for most applications where the wake downstream of the modified trailing edges impinges onto a fixed or moving surface, such as a mast or a subsequent rotor. The weakening of the cell structures in the wake behind the studied geometries could translate in strong variations of interaction noise.

- The initial idea was to work with smooth geometries to avoid the generation of stream-wise vorticity at the trough due to sharp angles. The multiscale approach has proven useful in keeping this requirement while breaking down the cellular structure of the wake. It could be useful to investigate compound geometries, by combining the present ones with brushes or slits, recently studied on triangular serrations as detailed in section 1.2.

- To complement the study of a wing subjected to a turbulent and coherent inflow, the rod-wing configuration could generate incoming coherence over a large span-wise extent at a high frequency. Such frequency can be selected, by varying the diameter of the rod, to be close to that of the serrations' vortex shedding to study the interaction of the two phenomena.

- A numerical study could provide useful information on the 3D flow structures, observed here mainly through 2D experimental data sets. However, the direct numerical simulation of the flow over a wing with complex trailing edge geometry and turbulent boundary layers at the current Reynolds number is extremely delicate. An alternative could be the use of high fidelity large eddy simulation.

- Finally, and as stated previously, a strong limitation of the study of unsteady inflows is their inherent complexity. A better characterisation of the incoming flow would be useful to link observed flow

structures to statistical properties of the lift fluctuations. For this, a possible experiment would be the study of the flow around the wing with particle image velocimetry, synchronised with the active grid protocols.

■

Bibliography

[1] R. K. Amiet. Noise due to turbulent flow past a trailing edge. *Journal of Sound and Vibration*, 47(3):387–393, 1976.

[2] C. Arce Leon, F. Avallone, S. Pröbsting, and D. Ragni. PIV Investigation of the Flow Past Solid and Slitted Sawtooth Serrated Trailing Edges. *54th AIAA Aerospace Sciences Meeting*, AIAA 2016-1014.

[3] C. Arce León, D. Ragni, S. Pröbsting, F. Scarano, and J. Madsen. Flow topology and acoustic emissions of trailing edge serrations at incidence. *Experiments in Fluids*, 57(5):1–17, 2016.

[4] F. Avallone, S. Probsting, K. Lynch, and D. Ragni. Tomographic-PIV investigation of the flow over serrated trailing-edges. *54th AIAA Aerospace Sciences Meeting*, AIAA 2016-1012.

[5] F. Avallone, S. Probsting, and D. Ragni. Three-dimensional flow field over a trailing-edge serration and implications on broadband noise. *Physics of Fluids*, 28(11):117101, 2016.

[6] M. Azarpeyvand, M. Gruber, and P. F. Joseph. An analytical investigation of trailing edge noise reduction using novel serrations. *19th AIAA/CEAS Aeroacoustics Conference*, AIAA 2013-2009.

[7] C. Bailly and G. Comte-Bellot. *Turbulence*. Springer, 2015.

[8] P. Baj, P. J. K. Bruce, and O. R. H. Buxton. The triple decomposition of a fluctuating velocity field in a multiscale flow. *Physics of Fluids*, 27(7):075104, 2015.

[9] R. J. Barthelmie, K. Hansen, S. T. Frandsen, O. Rathmann, J. G. Schepers, W. Schlez, J. Phillips, K. Rados, A. Zervos, E. S. Politis, and P. K. Chaviaropoulos. Modelling and measuring flow and wind turbine wakes in large wind farms offshore. *Wind Energy*, 12(5):431–444, 2009.

[10] R. J. Barthelmie, S. C. Pryor, S. T. Frandsen, K. S. Hansen, J. G. Schepers, K. Rados, W. Schlez, A. Neubert, L. E. Jensen, and S. Neckelmann. Quantifying the impact of wind turbine wakes on power output at offshore wind farms. *Journal of Atmospheric and Oceanic Technology*, 27(8):1302–1317, 2010.

[11] G. Berkooz, P. Holmes, and J. L. Lumley. The proper orthogonal decomposition in the analysis of turbulent flows. *Annual Review of Fluid Mechanics*, 25(1971):539–575, 1993.

[12] T. F. Brooks, D. S. Pope, and M. A. Marcolini. *Airfoil Self-Noise and Prediction*, volume 1218. National Aeronautics and Space Administration, Office of Management, Scientific and Technical Information Division, 1989.

[13] S. Buck, S. Oerlemans, and S. Palo. Experimental validation of a wind turbine turbulent inflow noise prediction code. *22nd AIAA/CEAS Aeroacoustics Conference*, pages 1–16, 2016.

[14] T. Chong, A. Vathylakis, P. Joseph, and M. Gruber. Self-Noise Produced by an Airfoil with Nonflat Plate Trailing-Edge Serrations. *AIAA Journal*, 51(11):2665 – 2677, Nov 2013.

[15] T. P. Chong and P. F. Joseph. An experimental study of airfoil instability tonal noise with trailing edge serrations. *Journal of Sound and Vibration*, 332(24):6335–6358, 2013.

[16] T. P. Chong and A. Vathylakis. On the aeroacoustic and flow structures developed on a flat plate with a serrated sawtooth trailing edge. *Journal of Sound and Vibration*, 354:65–90, 2015.

[17] T. P. Chong, A. Vathylakis, P. F. Joseph, and M. Gruber. On the Noise and Wake flow of an Airfoil with Broken and Serrated Trailing Edges. *AIAA Conference*, (June):05 – 08, 2011.

[18] U. Cordes, K. Hufnagel, C. D. Tropea, G. Kampers, M. Hölling, and J. Peinke. Experimental investigation of Passive Load Reduction under dynamic inflow conditions. *33rd AIAA Applied Aerodynamics Conference*, (June):1–12, 2015.

[19] U. Cordes, K. Hufnagel, C. D. Tropea, G. Kampers, M. Hölling, and J. Peinke. Experimental investigation of Passive Load Reduction under dynamic inflow conditions. *33rd AIAA Applied Aerodynamics Conference*, 2015-3313.

[20] U. Cordes, G. Kampers, T. Meißner, C. Tropea, and J. Peinke. *Journal of Fluid Mechanics*, 811, 2017.

[21] A. Finez, E. Jondeau, M. Roger, and M. C. Jacob. Broadband Noise Reduction of a Linear Cascade With Trailing Edge Serrations. *17th AIAA/CEAS Aeroacoustics Conference (32nd AIAA Aeroacoustics Conference)*, (June), 2011-2874.

[22] A. Fischer, T. Lutz, E. Kramer, U. Cordes, K. Hufnagel, C. Tropea, G. Kampers, M. Hölling, and J. Peinke. Numerical and experimental investigation of an airfoil with load control in the wake of an active grid. *Journal of Physics: Conference Series*, 753:022036, 2016.

[23] F. E. Fish and G. V. Lauder. Passive and Active Flow Control By Swimming Fishes and Mammals. *Annual Review of Fluid Mechanics*, 38(1):193–224, 2006.

[24] K. H. H. Goh, P. Geipel, and R. P. Lindstedt. Lean premixed opposed jet flames in fractal grid generated multiscale turbulence. *Combustion and Flame*, 161(9):2419–2434, apr 2014.

[25] M. Gruber, P. Joseph, and T. Chong. Experimental investigation of airfoil self noise and turbulent wake reduction by the use of trailing edge serrations. *16th AIAA/CEAS Aeroacoustics Conference*, 2010-3803.

[26] M. Gruber, P. Joseph, and T. Chong. On the mechanisms of serrated airfoil trailing edge noise reduction. *17th AIAA/CEAS Aeroacoustics Conference*, (June), 2011-2781.

[27] M. Gruber, P. F. Joseph, and M. Azarpeyvand. An experimental investigation of novel trailing edge geometries on airfoil trailing edge noise reduction. *19th AIAA/CEAS Aeroacoustics Conference*, 2013-2011.

[28] C. Hah and B. Lakshminarayana. Measurement and prediction of mean velocity and turbulence structure in the near wake of an airfoil. *Journal of Fluid Mechanics*, 115:251–282, 1982.

[29] F. Hoerner, Sighard. Fluid Dynamic Lift - Practical Information on Aerodynamic and Hydrodynamic Lift. *NASA STI/Recon Technical Report A*, page 507, 1985.

[30] M. Howe. Surface pressure fluctuations produced by vortex shedding from a coated airfoil. *Journal of sound and vibration*, 113(2):233–244, 1987.

[31] M. S. Howe. Aerodynamic noise of a serrated trailing edge. *Journal of Fluids and Structures*, 5(1):33–45, 1991.

[32] M. S. Howe. Noise produced by a serrated trailing edge. *J. Acoust. Soc. Am.*, 90(1):482–487, 1991.

[33] H. Johari, C. Henoch, D. Custodio, and A. Levshin. Effects of leading-edge protuberances on airfoil performance. *Aiaa Journal*, 45(11):2634–2642, nov 2007.

[34] L. E. Jones and R. D. Sandberg. Numerical Investigation of Airfoil Self-Noise Reduction by Addition of Trailing-Edge Serrations. *16th AIAA/CEAS Aeroacoustics Conference*, 2010-3703.

[35] L. E. Jones and R. D. Sandberg. Acoustic and hydrodynamic analysis of the flow around an aerofoil with trailing-edge serrations. *Journal of Fluid Mechanics*, 706:295–322, Jul 2012.

[36] M. R. Jovanovic, P. J. Schmid, and J. W. Nichols. Sparsity-promoting dynamic mode decomposition. *Physics of Fluids*, 26(2):024103, 2014.

[37] G. Kampers, J. Peinke, M. Hölling, U. Cordes, and C. Tropea. Stochastic analysis of aerodynamic forces acting on a self-adaptive camber airfoil in turbulent inflow. *33rd AIAA Applied Aerodynamics Conference*, (2015-2427), 1–7.

[38] P. S. Klebanoff. Characteristics of turbulence in a boundary layer with zero pressure gradient, 1955.

[39] P. Knebel, A. Kittel, and J. Peinke. Atmospheric wind field conditions generated by active grids. *Experiments in Fluids*, 51(2):471–481, 2011.

[40] D. Krentel and W. Nitsche. Investigation of the near and far wake of a bluff airfoil model with trailing edge modifications using time-resolved particle image velocimetry This article is part of the topical collection on application of laser techniques to fluid mechanics 2012. *Experiments in Fluids*, 54(7):1551, jun 2013.

[41] X. Liu, H. Kamliya Jawahar, M. Azarpeyvand, and R. Theunissen. Wake Development of Airfoils with Serrated Trailing Edges. *22nd AIAA/CEAS Aeroacoustics Conference*, 2016-2817.

[42] B. Lyu, M. Azarpeyvand, and S. Sinayoko. A Trailing-Edge Noise Model for Serrated Edges. *21st AIAA/CEAS Aeroacoustics Conference*, 2015-2362.

[43] B. Lyu, M. Azarpeyvand, and S. Sinayoko. Prediction of noise from serrated trailing-edges. *Journal of Fluid Mechanics*, 793(2016):556–588, 2016.

[44] J. Mathew, A. Singh, J. Madsen, and C. Arce León. Serration Design Methodology for Wind Turbine Noise Reduction. *Journal of Physics: Conference Series*, 753:022019, 2016.

[45] G. Melina, P. J. K. Bruce, and J. C. Vassilicos. Vortex shedding effects in grid-generated turbulence. *Physical Review Fluids*, 1(4):044402, 2016.

[46] D. S. Miklosovic, M. M. Murray, L. E. Howle, and F. E. Fish. Leading-edge tubercles delay stall on humpback whale (Megaptera novaeangliae) flippers. *Physics of Fluids*, 16(5):39–42, 2004.

[47] D. J. Moreau, L. Brooks, and C. J. Doolan. On the noise reduction mechanism of a flat plate serrated trailing edge at low-to-moderate Reynolds number. *18th AIAA/CEAS Aeroacoustics Conference (33rd AIAA Aeroacoustics Conference)*, (June), 2012-2186.

[48] D. J. Moreau and C. J. Doolan. Noise-Reduction Mechanism of a Flat-Plate Serrated Trailing Edge. *AIAA Journal*, 51(10):2513–2522, 2013.

[49] D. J. Moreau and C. J. Doolan. The generation of tonal noise from sawtooth trailing-edge serrations at low Reynolds numbers. *Aeronautical Journal*, 120(1228):971–983, 2016.

[50] J. Nedic, O. Supponen, B. Ganapathisubramani, and J. C. Vassilicos. Geometrical influence on vortex shedding in turbulent axisymmetric wakes. *Physics of Fluids*, 27(3):035103, 2015.

[51] J. Nedić and J. C. Vassilicos. Vortex shedding and aerodynamic performance of an airfoil with multi-scale trailing edge modifications. *AIAA Journal*, 53(11):3240–3250, 2015.

[52] S. Oerlemans. Reduction of wind turbine noise using blade trailing edge devices. *22nd AIAA/CEAS Aeroacoustics Conference*, 2016-3018.

[53] S. Oerlemans, M. Fisher, T. Maeder, and K. Kögler. Reduction of wind turbine noise using optimized airfoils and trailing-edge serrations. *AIAA Journal*, 47(6):1470–1481, Jun 2009.

[54] M. Petrusma and S. L. Gai. Investigation into the wakes of blunt trailing edge aerofoils at low reynolds numbers. In *Tenth Australasian fluid mechanics conference - university of Melbourne*, 1989.

[55] S. L. Prigent, O. R. H. Buxton, and P. J. K. Bruce. Wake of a lifting wing with cut-in sinusoidal trailing edges. *AIAA Journal*, 55(5):1590–1601, May 2017.

[56] G. Ramesh, L. Venkatakrishnan, and A. Prabhu. PIV studies of large scale structures in the near field of small aspect ratio elliptic jet. *Journal of Visualisation*, 9(1):23–30, 2006.

[57] E. Rind and I. P. Castro. On the effects of free-stream turbulence on axisymmetric disc wakes. *Experiments in Fluids*, 53(2):301–318, 2012.

[58] E. Rodríguez-López, P. J. K. Bruce, and O. R. H. Buxton. Near field development of artificially generated high Reynolds number turbulent boundary layers. *Physical Review Fluids*, 1(7):074401, 2016.

[59] R. D. Sandberg and L. E. Jones. Direct numerical simulations of low Reynolds number flow over airfoils with trailing-edge serrations. *Journal of Sound and Vibration*, 330(16):3818–3831, Aug 2011.

[60] M. Sanjosé, C. Méon, V. Masson, and S. Moreau. Direct numerical simulation of acoustic reduction using serrated trailing-edge on an isolated airfoil. *Arc.Aiaa.Org*, (June):1–15, 2014.

[61] J. Sato and Y. Sunada. Experimental research on blunt trailing-edge airfoil sections at low Reynolds numbers. *AIAA Journal*, 33(11):2001–2005, 1995.

[62] P. J. Schmid. Dynamic mode decomposition of numerical and experimental data. *Journal of Fluid Mechanics*, 656:5–28, 2010.

[63] P. J. Schmid. Application of the dynamic mode decomposition to experimental data. *Experiments in Fluids*, 50(4):1123–1130, 2011.

[64] J. Schottler, A. Hölling, J. Peinke, and M. Hölling. Wind tunnel tests on controllable model wind turbines in yaw. *34th Wind Energy Symposium*, (January), 2016.

[65] J. Schottler, N. Reinke, A. Hölling, J. Whale, J. Peinke, and M. Hölling. On the impact of non-Gaussian wind statistics on wind turbines - an experimental approach. *Wind Energy Science*, (2), 2017.

[66] H. A. Smith and R. F. Schaefer. Aerodynamic Characteristics at Reynolds Numbers of 3.0106 and 6.0106 of Three Airfoil Sections Formed by Cutting Off Various Amounts from the Rear Portion of the NACA 0012 Airfoil Section. *Naca Tn-2074*, 1950.

[67] K. J. Standish and C. P. van Dam. Aerodynamic Analysis of Blunt Trailing Edge Airfoils. *Journal of Solar Energy Engineering*, 125(4):479, 2003.

[68] Tanner, M. A Method for Reducing the Base Drag of Wings with Blunt Trailing Edge. Technical report, DTIC Document, 1970.

[69] N. Tombazis and P. W. Bearman. A study of three-dimensional aspects of vortex shedding from a bluff body with a mild geometric disturbance. *Journal of Fluid Mechanics*, 330:85–112, Jan 1997.

[70] A. Vathylakis, C. C. Paruchuri, T. P. Chong, and P. Joseph. Sensitivity of aerofoil self-noise reductions to serration flap angles. *22nd AIAA/CEAS Aeroacoustics Conference*, 2016-2837.

[71] M. Wächter, H. Heißelmann, M. Hölling, A. Morales, T. Milan, P.and Mücke, J. Peinke, N. Reinke, and P. Rinn. The turbulent nature of the atmospheric boundary layer and its impact on the wind energy conversion process. *Journal of Turbulence*, 13(July):N26, 2012.

[72] M. Werle, R. Paterson, and W. Presz Jr. Trailing-Edge Separation/Stall Allevation. *AIAA Journal*, 25(4):624–626, 1987.

[73] A. Wynn, D. S. Pearson, B. Ganapathisubramani, and P. J. Goulart. Optimal mode decomposition for unsteady flows. *Journal of Fluid Mechanics*, 733:473, 2013.

[74] K. B. M. Q. Zaman. Axis switching and spreading of an asymmetric jet: the role of coherent structure dynamics. *Journal of Fluid Mechanics*, 316(1996):1–27, 1996.

[75] A. Zobeiri, P. Ausoni, F. Avellan, and M. Farhat. An experimental investigation on vortex induced vibration of a flexible inclined cable under a shear flow. *Journal of Fluids and Structures*, 54(3):297–311, 2015.